This electronic thesis or dissertation has been downloaded from the King's Research Portal at https://kclpure.kcl.ac.uk/portal/

Ergodicity and localisation in mean-field quantum systems

Facoetti, Davide

Awarding institution:
King's College London

The copyright of this thesis rests with the author and no quotation from it or information derived from it may be published without proper acknowledgement.

END USER LICENCE AGREEMENT

Unless another licence is stated on the immediately following page this work is licensed

under a Creative Commons Attribution-NonCommercial-NoDerivatives 4.0 International

licence. https://creativecommons.org/licenses/by-nc-nd/4.0/

You are free to copy, distribute and transmit the work

Under the following conditions:

- Attribution: You must attribute the work in the manner specified by the author (but not in any way that suggests that they endorse you or your use of the work).
- Non Commercial: You may not use this work for commercial purposes.
- No Derivative Works - You may not alter, transform, or build upon this work.

Any of these conditions can be waived if you receive permission from the author. Your fair dealings and other rights are in no way affected by the above.

Take down policy

If you believe that this document breaches copyright please contact librarypure@kcl.ac.uk providing details, and we will remove access to the work immediately and investigate your claim.

Download date: 06. May. 2023

Thesis submitted to King's College London
for the degree of Doctor of Philosophy

Ergodicity and localisation in mean-field quantum systems

Candidate: Davide Facoetti
Supervisor: Dr Pierpaolo Vivo

Abstract

Recent years have seen a resurgence of interest in fundamental questions regarding the out-of-equilibrium behaviour of isolated quantum systems. Due to both new experimental techniques, such as those involving cold atomic gases, and progress in the theoretical understanding of closed quantum systems, it is now possible to explore fundamental questions about thermalisation and the applicability of statistical mechanics. The interplay between disorder, interactions and quantum interference gives rise to interesting phenomena, such as many-body localisation (MBL), which has a key role in the non-equilibrium behaviour of such systems.

Realistic models of disordered, interacting quantum systems are largely intractable analytically. Their numerical study is limited by the difficulty of simulating quantum systems with classical computers, making it challenging to separate genuine "thermodynamic" results from finite size effects. In this thesis we consider some more tractable mean-field models, as a starting point to investigate specific aspects of ergodicity and localisation transitions in many-body systems.

The first part is devoted to the outstanding question of whether MBL systems undergo two separate ergodicity and localisation transitions when disorder strength is increased. The two transitions are separated by a putative "bad metal", non-ergodic extended (NEE) phase, in which ergodicity is broken but the eigenstates are not exponentially localised. We show explicitly the existence of the NEE phase in a random matrix model, and characterise it using the local resolvent in an unusual scaling limit.

In the second part we consider a spin glass model, in which quantum effects are introduced by a transverse magnetic field. A refined equilibrium phase diagram, going beyond the quasi-static approximation, is obtained with a numerically exact diagrammatic Monte Carlo approach. We discuss the difference between the ergodic, eigenstate and clustering transitions.

Finally, we consider a quantum model that shares some of the peculiar low-temperature properties which have brought the Sachdev–Ye–Kitaev (SYK) model under the spotlight of the string theory community. In our model such properties are understood in terms of the glassy dynamics of a corresponding classical stochastic system.

Acknowledgements

I would like to express my deep appreciation to Pierpaolo Vivo for his mentoring and support over the past four years. It was a pleasure to work under his supervision. His scientific curiosity, enthusiasm in following ideas and clarity in sharing them have been, and will continue to be, great source of inspiration.

I am indebted to Giulio Biroli for suggesting many interesting problems, and for his guidance and insight while working on some of them. In the same regard I would like to thank Jorge Kurchan, David R. Reichman and Marco Schiró, with whom I had the pleasure to collaborate on different parts of this work. I thank Joe Bhaseen for many discussions, his sharp questions, and advice.

I am grateful to Leticia F. Cugliandolo and Juan P. Garrahan for accepting to be examiners for this thesis, for the ensuing interesting discussions and for offering useful comments.

The Disordered Systems group at King's College London has provided a lively research environment and precious support. The CANES CDT complemented this, offering many stimulating opportunities. I thank all the people involved, and in particular Chris Lorenz and Valeria De Marco.

I was supported by the EPSRC centre for doctoral training in Cross-Disciplinary Approaches to Non-Equilibrium Systems (CANES, EP/L015854/1). This work benefited from several visits to the the Institut de Physique Théorique (IPhT, CEA Saclay) and ENS Paris, and a visiting period at the Department of Chemistry of Columbia University. Their hospitality is acknowledge, as well as funding from ERC (NPRGGLASS), the Simons Foundation (#454935 Giulio Biroli, #454951 David R. Reichman), and LabEx (ANR-10-LABX-0039-PALM).

Collaboration statement

This thesis is the result of my own work, performed with the following collaborations:

- Chapter 2 is an extended version of [1], with Giulio Biroli and Pierpaolo Vivo.
- Chapters 3 and 4: work done in collaboration with Giulio Biroli, Marco Schiró and Pierpaolo Vivo. Manuscript in preparation.
- Chapter 5: work with Giulio Biroli, Jorge Kurchan and David R. Reichman. Most of the results have been included in [2].

Contents

List of Figures

1 Introduction

1.1 Thermalisation in closed quantum systems

Quantum statistical mechanics was developed as a framework together with quantum mechanics itself. The introduction of density operators by von Neumann in 1927 [3] allowed the application of the ideas of statistical mechanics to quantum systems, leading to the well established description of systems at equilibrium. The central idea of this framework is that quantum states can be well described by a density matrix depending only on a few macroscopic parameters.

However, it is far from trivial to explain how these equilibrium states are reached, starting from the microscopic description of local dynamics. In particular, in closed systems unitarity and time-reversal invariance of the evolution imply that (strictly speaking) the state cannot evolve to a thermal one. This draws attention to the fact that the very definition of thermalisation is nontrivial. These questions were asked in the early days of quantum statistical mechanics; however they have remained largely unanswered for a long time. The topic has seen a resurgence of interest in recent years, driven both by experimental developments and progress in theoretical techniques [4].

Experiments involving ultra-cold atomic gases [5] provide examples of of systems which are very well isolated from their environment, and undergo unitary dynamics. This, combined with the possibility of very good control of parameters of the systems, make them the ideal playground to explore fundamental questions about quantum phenomena, including those about non-equilibrium dynamics and thermalisation. Interest in these systems is also motivated by possible applications, including the simulation of condensed matter systems for which experimental control is not as good, and in quantum computing.

For isolated systems undergoing unitary dynamics thermalisation is not possible in the strong sense that the state converges at late times to an equilibrium ensemble. However it is observed that many systems thermalise in the sense that long-time aver-

ages of expectation values of local observables equal those from a statistical ensemble,

$$\lim_{T\to\infty} \frac{1}{T} \int_0^T \mathrm{d}t \, \langle A(t) \rangle = \langle A \rangle_{th} = \mathrm{Tr}\,(\rho_{th} A), \tag{1.1}$$

where ρ_{th} is the density matrix obtained as the maximum entropy state holding all constants of motion fixed. While the latter is a mathematically weaker statement, the physical implications are the same if one only has access to local observables.

This hints to a solution to the apparent paradox of quantum thermalisation, as described for example in the review [6]. To reach equilibrium, a system must "forget" all the information about the initial state, except for a few conserved quantities corresponding to parameters of the equilibrium state. However unitary dynamics cannot erase any information. The solution to this is that information about the initial state is not erased, but hidden in non-local correlations. Since a many-body system can typically be probed only by measuring local observables, information hidden in this way can be effectively inaccessible, and the system can thermalise in the sense of (1.1).

If only local operators $\mathcal{O}(x)$ are considered, one can ideally divide the system in a small region A including the support of $\mathcal{O}(x)$, and its complement B. Expectation values can be written in terms of the reduced density matrix $\rho_A = \mathrm{Tr}_B\, \rho$, where ρ is the state of the full system. For thermalising systems, it is ρ_A that is effectively thermal. In this case, the system is acting as its own thermal bath: B effectively acts as a reservoir for the small subsystem A.

Since thermalisation is observed in many systems, it is interesting to look for generic mechanisms through which it happens. The most prominent explanation is known as the eigenstate thermalisation hypothesis (ETH) [7, 8]. The basic idea of the ETH is that all many-body eigenstates of the system are thermal, in the sense that

$$\rho_A = \mathrm{Tr}_B\, |\psi\rangle \langle\psi| \tag{1.2}$$

looks like a thermal for any eigenstate $|\psi\rangle$ of the Hamiltonian describing the system. The corresponding eigenvalue gives an energy density which sets the effective temperature of the thermal state. The ETH is a strong statement, but it is necessary if one wants the system to thermalise starting from any initial state [9]. It can be relaxed by requiring thermalisation only from most states drawn randomly from some measure, which can implement physical requirements of typical states prepared in experiments [10].

The experimental observation that some systems fail to thermalise [11], showing

memory of the initial state even after long times sparked interest in the study of the breakdown of ETH and ergodicity. Theoretical explanations for the lack of thermalisation in many-body systems fall in the two main areas of integrability and many-body localisation (MBL). The former deals with systems described by integrable models, in which an extensive (in system size) number of local conserved quantities prevent relaxation to a thermal state. This work falls in the latter, which studies systems in which the interplay between interactions and disorder is the cause of ergodicity breaking.

1.2 Many-body localisation

Consider a quantum particle hopping on a disordered lattice. It can be modelled by the tight-binding Hamiltonian

$$H = t \sum_{\langle i,j \rangle} \left(c_i^\dagger c_j + c_j^\dagger c_i \right) + \sum_i \varepsilon_i c_i^\dagger c_i, \tag{1.3}$$

where the first term implements hopping between nearest neighbouring sites with rate t, ε_i are random on-site energies.

If all the ε_i's are zero, it reduces to the basic model for calculations of electronic band structure, see *e.g.* [12]. A single particle placed on a site i of such lattice will explore all the sites, and the return probability

$$P_i(t) = |\langle i| \, \mathrm{e}^{-\mathrm{i}Ht} \, |i\rangle|^2 \tag{1.4}$$

will go to zero at long times for an infinite system. However, depending on features of the lattice, such as the dimensionality, and on the strength of the disorder (the typical value of the ε_i's) the interference between multiple-scattering paths can inhibit diffusion. This is the well known phenomenon of Anderson localisation (AL) [13], which is crucial for the understanding of electric and thermal conduction properties of crystalline materials, taking into account the effect of impurities.

This can be understood from spectral properties, as the fact that the eigenstates of H are exponentially localised:

$$\psi_\alpha(j) = \langle j | \psi_\alpha \rangle \propto \exp\left(-\frac{|j - i_\alpha|}{\xi} \right), \tag{1.5}$$

where α labels the eigenstate localised around the site i_α, and xi is a disorder-dependent localisation length. Since the dynamics is controlled by the eigenstates,

this means that a single particle placed on a site will remain within a distance ξ from the initial site, it cannot explore the whole lattice, and the return probability remains finite at late times, breaking ergodicity.

The question of what happens to many-body systems with localised single-particle counterpart, when interactions between the particles are taken into account, spawned the field of research known as many-body localisation (MBL) [6]. Recent interest in this area is motivated by progress in the theoretical description of both disordered electronic systems [14], and simpler models used to investigate fundamental questions of quantum statistical mechanics [15].

A paradigmatic example of such models is the random field Heisenberg spin chain [6, 15],

$$H = \sum_i h_i \sigma_i^z + J \sum_i \vec{\sigma}_i \cdot \vec{\sigma}_{i+1} \tag{1.6}$$

in which each spin interacts with its nearest neighbours, and with an external fixed field h_i chosen randomly from a continuous distribution of width W. The model is still not completely understood, despite being the object of intense scrutiny due to indications that it thermalises if W/J is small enough, while ergodicity is broken at strong disorder due to the presence of a many-body localised phase [15].

There is no commonly accepted clear definition of many-body localisation in the literature. Features commonly ascribed to MBL systems include [6, 16]:

- Breaking of ergodicity: some memory of the initial conditions is preserved in local observables at long times.
- The ETH is not satisfied.
- Absence of diffusion: as in Anderson localisation, transport coefficients (conductivity) vanish.
- Absence of level repulsion: the statistics of level spacing is given by a Poisson distribution, instead of the Wigner-Dyson distribution of Gaussian random matrices that characterises ergodic systems.
- Area law entanglement in excited states.
- Slow (logarithmic) growth of entanglement.
- Anderson localisation in configuration space.
- The emergence of quasi-local integrals of motion, or ℓ-bits: operators obtained by dressing the original spins that are conserved by the dynamics.

In the following, we focus on the characterisation of MBL as localisation in Fock space, and how it differs from single-particle localisation on finite-dimensional lattice. In particular we concentrate on the connections and differences between static

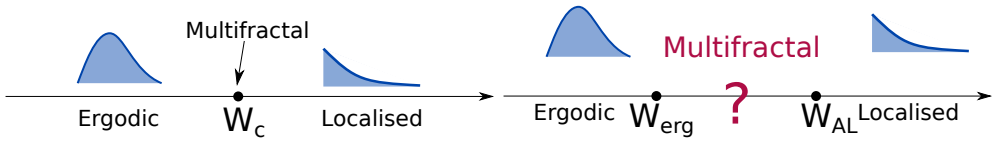

Figure 1.1: Representation of typical AL transitions (left), and the proposed two-transitions scenario that might be relevant for MBL (right). Poisson and Wigner-Dyson level statistics are represented, corresponding to localised and ergodic phases.

or spectral properties (eigenstate localisation) and dynamical properties (ergodicity breaking).

1.3 Extended, non-ergodic phases

Localisation transitions

As previously explained, the emergence of localisation can depend on the strength of the disorder. It is interesting to study the transition between ergodic and localised phases with the disorder strength W as a control parameter. Typical systems that support both AL and ergodic phases, such as the three-dimensional cubic lattice [13], have a sharp transition at a critical strength W_c. For any $W > W_c$ the system is localised, while for $W < W_c$ it is ergodic [17].

It has been proposed that some MBL systems are instead characterised by two separate transitions [14, 18], a localisation transition at W_{AL} and an ergodic transition at $W_{erg} < W_{AL}$. According to this picture, the system shows three different phases: a completely localised phased for $W > W_{AL}$, an ergodic phase for $W < W_{erg}$, and an intermediate extended, non-ergodic regime. In the intermediate "bad metal" regime, eigenstates would be delocalised over a large number of configurations, but which only cover a very tiny fraction, vanishing for large system size, of the entire Fock space. The unusual properties of this phase, first considered in the context of MBL in [18], are related to multifractal properties of the eigenstates, which instead AL systems only show exactly at the transition $W = W_c$ [17]. The proposed difference between AL and MBL transitions is represented schematically in Fig. 1.1.

Anderson Localisation in Fock space

Many-body localisation can be understood as Anderson localisation on a non-trivial graph. The correspondence, first suggested in [18], is obtained by identifying the

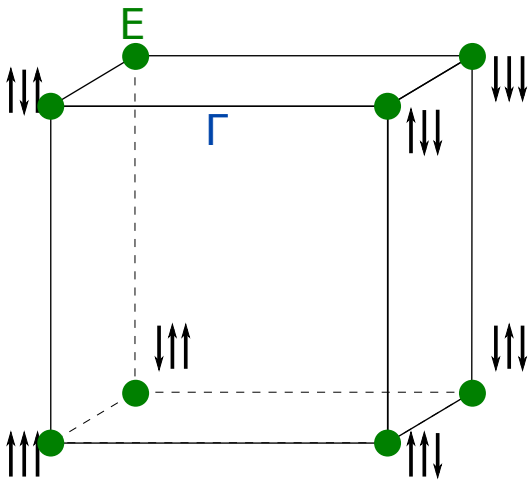

Figure 1.2: Representation of the Fock space of $N = 3$ spins as a cube. Each vertex labels an eigenstate in the localised phase (strong-disorder limit), each side a hopping (spin-flipping) term.

many-body Fock states, eigenstates of the non-interacting Hamiltonian, with sites of the graph. The system can be effectively described as a particle hopping on the graph, with an amplitude given by the non-zero matrix element between Fock states given by the interactions.

As a general example, consider a system of N spins, with Hamiltonian H_0 that is diagonal in the computational basis, *i.e.* eigenstates are obtained by independently setting each spin to be up or down in the σ^z eigenbasis. The resulting 2^N eigenstates, labelled by their energy, can be represented as the vertices of an N-dimensional hypercube. A system starting in a classical configuration of up-or-down spins will stay in that configuration. Adding to the Hamiltonian a transverse field $H = H_0 - \Gamma \sum \sigma^x$ introduces spin flips to the dynamics. In terms of the hypercube, the state of the system can be represented as a particle hopping between the sites with rate $\propto \Gamma$, see Fig. 1.2. In this sense, a many-body Hamiltonian can be mapped to a single-particle Hamiltonian of the form (1.3), in which all the complication of the many-body problem is hidden both in the structure of the graph, and in the correlations between on-site energies.

Specific realisations of the model described include the quantum random-energy and quantum p-spin models, studied in Chapter 4. The random-field Heisenberg spin chain (1.3) can be represented in a similar way, but with the hopping term J flipping two neighbouring spins at once instead of just one, inducing a different graph structure.

The structure of the graph is that of a very high dimensional lattice, organised

hierarchically: each of the 2^N sites is connected to $\propto N$ other sites by the hopping; starting from one configurations, all the others can be organised in *levels* counting the number of spin flips (more generally, hopping distance) from the root configurations. This is reminiscent of the Bethe lattice and random regular graphs. For this reason, Anderson localisation on such lattices has been considered by many as a simplified case to study questions related to the MBL transition. An important difference between the Bethe lattice and the ones obtained by the mapping from many-body Hamiltonians, is that the former is a tree, while the latter have many short loops.[1] For this reason, the study of the Bethe lattice as a model for MBL intrinsically introduces a mean-field approximation, ignoring the interference between different paths. This is similar to the forward-scattering approximation (FSA), in which only the shortest path between two states is retained. The approximation improves as the local connectivity of the graph increases, and it has been shown to give a good description of the localised phase, including a good estimate of the critical disorder for the Anderson model in high dimension, and for MBL in the Heisenberg chain [19].

The study of such graphs has attracted a lot of attention recently [20–22] because it could provide a test ground to analyse the "bad metal" regime described in the previous paragraph. Although the existence of the MBL transition is now well established (at least for one-dimensional systems) [6], the understanding of the delocalised non-ergodic phase is far from being complete. Some numerical results seem to indicate its presence in many-body systems [23, 24] whereas its existence on Bethe lattices is under intense scrutiny and debate [20–22, 25–27].

1.4 Ergodicity breaking in glasses

Models of spins in the presence of disorder have been studied long before the recent interest in MBL, in the field of spin glasses. Motivated by experiments with magnetic impurities, Edwards and Anderson proposed a model of spins $s_i = \pm 1$ with a random nearest-neighbour interaction [28, 29]

$$H = \sum_{\langle i,j \rangle} J_{ij} s_i s_j \ . \tag{1.7}$$

Due to the difficulty of analysing the Hamiltonian (1.7) on a cubic d-dimensional lattice, the Sherrington–Kirkpatrick (SK) [30] model was introduced, in which the Hamiltonian has the same form, but the interaction is all-to-all. This fully-connected

[1] For example, configurations differing by two spin flips are obviously connected in two different ways.

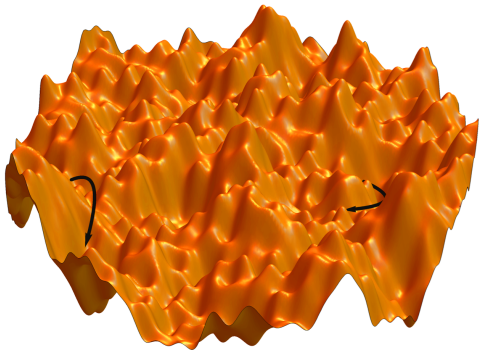

Figure 1.3: Schematic representation of a rugged free-energy landscape. From scglass.uchicago.edu, (Chiara Cammarota).

model provides a *mean-field* approximation to the nearest-neighbour one, in which fluctuations are suppressed and which becomes exact in the infinite-dimensional limit. The strategy is the same as that used for ferromagnets, in which the Curie–Weiss model is used as a starting point for the solution of the more difficult finite-dimensional Ising model.

Unlike the case of ferromagnetism, the study of spin glasses poses a formidable challenge already at the mean-field level, due to the need to average over the disorder. The equilibrium analysis of the SK model was solved by Parisi with the introduction of replica symmetry breaking [31]. Parisi's analysis and subsequent work (see *e.g.* [32–35] for reviews) showed that the SK model has two very different thermodynamic phases. At high temperature, its equilibrium properties are those of a paramagnetic system. Below a critical temperature T_k, it is characterised by a complex, "rugged" free-energy landscape, with large number of local minima and saddle points.

From the dynamical point of view, the SK model is ergodic in the paramagnetic phase, and becomes non-ergodic below T_k (the equilibration timescale is of order N and diverges in the thermodynamic limit). This is understood as the system being "stuck" in the minima of the landscape.

In this thesis we are interested in a related class of models, known as p-spin model, in which the Hamiltonian has p-body interactions (the SK model is recovered for $p = 2$)

$$H = -\sum_{i_1<\cdots<i_p} J_{i_1\cdots i_p} s_{i_1} \cdots s_{i_p}. \tag{1.8}$$

This model, which we review in Chapters 3 and 4, has a similar characterisation in terms of a rugged free-energy landscape, with some important differences compared to SK. It also has a thermodynamical transition at a temperature T_k; however the dynamics becomes non-ergodic at a higher temperature $T_d > T_k$, the dynamical glass transition. In the $p \to \infty$ limit the model becomes the random energy model (REM), the "simplest spin glass" [36–38], see Chapter 3.

Quantum effects can be introduced, *e.g.* by adding a transverse magnetic field, leading to the quantum p-spin model considered in Chapter 4. The dynamical glass transition is then a mechanism for *dissipative* quantum dynamics to become non-ergodic. Quantum spin glass models have been reconsidered more recently from the point of view of isolated quantum dynamics and localisation properties, as potential mean-field models of MBL [39–43]. Part of this thesis is devoted to the study of equilibrium, dynamical and localisation transitions in the quantum p-spin and quantum random energy models.

The collection of ideas and techniques briefly described above, based on an underlying rugged free-energy landscape, provides one of the paradigm for the description of glasses [44], spin glasses, and other complex phenomena (see *e.g.* [35] for a review of applications to optimisation problems).

In this thesis we always refer to *(spin) glasses* with this paradigm in mind. However it is important to note that other theories, relying on a purely dynamical rather than thermodynamical description, have been proposed and represent equally lively and stimulating research directions. See [45] for a perspective comparing both approaches, and [46] for a more recent review of classical glassy physics and quantum non-ergodicity from the purely dynamical perspective.

2 Extended, non-ergodic phases: a random matrix perspective

2.1 Extended, non-ergodic phases

The theoretical study of the non-equilibrium dynamics of isolated quantum systems has attracted considerable interest in recent years, partly due to advances in experiments on trapped ultra-cold atomic gases [4]. One of the most fundamental questions that arose is about the applicability of statistical mechanics to quantum systems in presence of interactions and disorder, and the related Many-body localisation (MBL) transition [14]. A system is in a MBL phase if, taking interactions into account, the many-body eigenstates are localised in Fock space. The Fock space can be seen as a graph with connectivity determined by two-body interactions. Its structure is that of a very high dimensional graph where loops are scarce, therefore reminiscent of the Bethe lattice and random regular graphs (RRG). Starting from the pioneering work [18], Anderson localization on such graphs has been considered by many as a simplified case to study questions related to the MBL transition. It attracted a lot of attention recently [20–22] because it could provide a test ground to analyse the delocalised non-ergodic or "bad metal" regime, which was predicted as an intermediate phase separating the fully delocalised and the MBL phases [14, 18]. In this regime, eigenstates would be delocalised over a large number of configurations, but which only cover a very tiny fraction, vanishing for large system size, of the entire Fock space. Although the existence of the MBL transition is now well established (at least for one dimensional systems) [6], the understanding of the delocalised non-ergodic phase is far from being completed. Some numerical results seem to indicate its presence in many-body systems [23, 24] whereas its existence on Bethe lattices is under intense scrutiny and debated [20, 22, 25–27]. It is not clear at this stage whether the sub-diffusive behaviour found before the MBL transition [47–51] is somehow related to it.

Given this state of the art, it is therefore useful to study simpler models that could provide a playground to explore its nature and sharpen the questions about it. With

this aim, the authors of Ref. [52] proposed a random matrix model, the generalised Rosenzweig–Porter (GRP) model, as a relative of the RRG with random on-site energy. This was motivated by the known relation between the RRG and Gaussian invariant ensembles of random matrix theory [53]. They showed that the GRP model indeed undergoes two transitions: a localisation transition and a separate ergodic transition, with an intermediate delocalised non-ergodic phase separating the two.

In this work we also focus on this model. Our aim is to further characterise the intermediate phase of the GRP model. We do so by applying a technique based on a recurrence relation for the resolvent matrix, and the Dyson Brownian motion. Our main results consist in linking the statistics of the local resolvent to the properties of the mixed phase, and in combining these insights with the Brownian motion analysis to derive the scaling of the eigenstates. Besides the interest in the MBL context, our results are also relevant in other physical situations where quasi-delocalised states emerge, such as jamming [54] and random matrix theory [55, 56].

2.2 The generalised Rosenzweig–Porter model

Following [52], we consider a generalisation of the Rosenzweig–Porter model [57], with the Hamiltonian given by a $N \times N$ Hermitian matrix

$$H = A + \frac{\mu}{N^{\gamma/2}} V \ , \tag{2.1}$$

where A is diagonal with real entries a_i, independently drawn from a probability density $p_A(a_i)$, while V belongs to the Gaussian unitary ensemble (GUE) with unit variance. Drawing analogies with the RRG, the GUE matrix V corresponds to the structural geometrical disorder, while A to the on-site disorder.[1] The parameter γ controls the relative magnitude of the two terms: it is a proxy for the strength of the on-site disorder. For $\gamma > 2$, standard second order perturbation theory shows that the GUE term is a small regular perturbation (the perturbation of the eigenvalues is much smaller than their typical level spacing). As a consequence, the Hamiltonian is close to A and hence eigenstates are completely localised. Similarly, for $\gamma < 1$ the first term is a small regular perturbation, hence the rotationally invariant V term dominates, and the eigenstates are uniformly distributed on the unitary sphere, as for the GUE. The

[1] The analogy with the RRG would suggest to choose V real symmetric (GOE). We consider the unitary model because most of the literature focuses on it. Our conclusions apply to both versions of the model.

value $\gamma = 1$ was indeed shown to play a special role for the density of states [58–62], which is given for $\gamma < 1$ by the Wigner semicircle distribution, and for $\gamma > 1$ by p_A. At $\gamma = 1$ it has a non-trivial, μ-dependent form, interpolating between the semicircle and p_A in the limiting cases $\mu \to \infty, 0$.

The value $\gamma = 2$ instead governs the level statistics on the scale of the typical level spacing. Computing the spectral form factor, the unfolded two-point correlation function was shown to be universal, *i.e.* it does not depend on the specific form of p_A [52, 59]. It has the Wigner–Dyson form for $\gamma < 2$, and Poisson for $\gamma > 2$. These results confirm that for $\gamma < 1$ and $\gamma > 2$ the system is respectively fully delocalised and fully localised. The regime $\gamma \in (1, 2)$ instead is special: the density of states is given by p_A and not by Wigner semicircle but nevertheless the nearest neighbours level statistics has the Wigner–Dyson form. As shown in [52, 63] and discussed later on, this regime provides a simple example of a delocalised non-ergodic phase.

The authors of Ref. [52] characterised the eigenstates for $\gamma \in (1, 2)$, finding the support set [21] to be a fractal over $N^{D_1} = N^{2-\gamma}$ sites. For large N, the eigenstates are supported over a large number of sites, so they are delocalised - but only over a fraction $\propto N^{1-\gamma}$ of all sites, which tends to zero in the thermodynamic limit.

To study the spectral statistics we focus on the resolvent matrix

$$\mathbf{G}(z) = (z - H)^{-1} \,, \tag{2.2}$$

a standard tool of random matrix theory. It is a random complex function, which evaluated at $z = \lambda - i\eta$ carries information about spectral quantities at energy λ, on a scale η, see Appendix 2.A for a more precise explanation. The (global) resolvent is $G(z) = \operatorname{Tr} \mathbf{G}(z)/N$, while the diagonal elements of $\mathbf{G}$ are known as the local resolvent. The behaviour of $G(z)$ is completely featureless: in the large N limit it converges to a non-fluctuating value of order one as long as $\eta > 1/N$, as can be checked by using the spectral representation of $G(z)$. The statistics of the local resolvent can be instead used as a tool to probe localisation transitions. In general one focuses on its imaginary part for $\eta \to 0$ *after* the $N \to \infty$ limit is taken: in the localised phase the imaginary part vanishes whereas it remains finite in the delocalised phase, see, *e.g.*, [64]. As we shall show below, in order to probe the non-ergodic delocalised phase one instead needs to consider a different scaling limit and study how the statistical properties of the local resolvent evolve when η goes to zero as $1/N^\delta$ for $\delta < 1$. More intuition on this is given in the following discussion, and in Appendix 2.A.

In the next section we derive the probability distribution for the local resolvent in

the delocalised non-ergodic phase. We then combine this with results from the Dyson Brownian motion analysis to get a complete picture of the non-ergodic delocalised phase.

2.3 Local resolvent statistics and non-ergodic delocalised phase

Consider a matrix H, drawn from the N-dimensional GRP ensemble (2.1). We can promote it to an $N+1$ dimensional matrix by adding a zero-th row and column, with statistics given by the $N+1$-dimensional GRP ensemble

$$H^{(N+1)} = \left(\begin{array}{c|c} H_{00} & H_{0i} \\ \hline H_{i0} & H^{(N)} \end{array}\right) . \tag{2.3}$$

The resolvent is the inverse of the matrix $z-H$, which obviously has the same block structure. Using the blockwise matrix inversion formula (see *e.g.* [65]) on the 1×1 block, it is possible to derive the equality in distribution between random variables

$$G_{00}^{(N+1)}(z)^{-1} \stackrel{d}{=} z - H_{00} - \frac{\mu^2}{N^\gamma}\sum_{ij} G_{ij}^{(N)}(z) V_{0i}V_{j0} \ , \tag{2.4}$$

relating the probability distribution of the $N+1$-dimensional local resolvent to those of the N-dimensional local resolvent and uncorrelated matrix elements.

The recurrence equation for the local resolvent is not specific to the model considered here. It is closely related to the Bethe–Peierls/belief propagation (BP) method, leading in general to self-consistent integral equations for the probability distributions, which can be solved in the thermodynamic limit by population dynamics algorithms [64, 66, 67]. We now argue that for the GRP model, the sum in the right hand side of (2.4) is self-averaging with respect to the V_{0i}s and the V_{ij}s in the large N limit. As a consequence, we derive the exact probability distribution for the local resolvent at $N\to\infty$, without the need to solve any self-consistent equation numerically. Indicating explicitly the independent random variables, equation (2.4) takes the form

$$G_{00}^{(N+1)}(z)^{-1} = z - a_0 - \frac{\mu}{N^{\gamma/2}}V_{00} - \frac{\mu^2}{N^{\gamma-1}}\left(\underbrace{\frac{1}{N}\sum_i G_{ii}^{(N)}(z)|V_{0i}|^2}_{X} + \underbrace{\frac{2}{N}\sum_{i<j} G_{ij}^{(N)}(z)V_{0i}V_{j0}}_{Y}\right) . \tag{2.5}$$

Consider the random variable X defined in (2.5). Note that the quantities multiplied in each term of the sum are statistically independent, as they involve different blocks of (2.3), which are constructed to be independent. The mean and variance of X are

$$\langle X \rangle = \frac{1}{N} \sum_i \langle G_{ii}^{(N)}(z) \rangle \, \langle |V_{0i}|^2 \rangle = \frac{2}{N} \sum_i \langle G_{ii}^{(N)}(z) \rangle \tag{2.6}$$

$$\langle |X|^2 \rangle_c \equiv \langle |X|^2 \rangle - |\, \langle X \rangle \,|^2 = \frac{4}{N^2} \sum_i \left(2 \, \langle |G_{ii}|^2 \rangle - |\, \langle G_{ii} \rangle \,|^2 \right) + \frac{4}{N^2} \sum_{(i,j)} \langle G_{ii} G_{jj}^* \rangle_c \tag{2.7}$$

To find the scaling of the variance of X at large N, estimates are needed for the covariances of the local resolvent elements, which can be obtained from diagrammatic perturbation theory [61]. In Gaussian rotationally invariant ensembles, $\langle G_{ii} \rangle$ is of order one, while variances and covariances scale as $1/N$. The average of X (2.6) is of order one, and both terms in (2.7) are of order $1/N$. In the GRP ensemble, the diagonal matrix A introduces a perturbation that in terms of diagrams is represented by an extra diagonal vertex. This changes the scaling of the variance $\langle |G_{ii}|^2 \rangle_c \propto \mathrm{Var}(a)$, which however does not affect the scaling of the first term in (2.7). On the other hand, as long as the diagonal entries of A are uncorrelated, to leading order in N the covariances $\langle G_{ii} G_{jj} \rangle_c , i \neq j$ are unchanged, because the extra diagrams cancel when computing the connected correlation.

A similar analysis can be performed on Y. Noting that the off-diagonal elements have $\langle |G_{ij}|^2 \rangle \propto \mathcal{O}(N^{-\gamma})$, and correlations $\langle G_{ij} G_{kl} \rangle$ are further suppressed,

$$\langle Y \rangle = 0, \qquad \langle |Y|^2 \rangle = \frac{8}{N^2} \sum_{i<j} \langle |G_{ij}|^2 \rangle \approx \mathcal{O}(N^{-\gamma}) \ . \tag{2.8}$$

Therefore, in the large N limit, fluctuations are suppressed, and X and Y become non-fluctuating quantities, equal to $\langle X \rangle = \langle G_{ii}(z) \rangle = G(z)$ and $\langle Y \rangle = 0$ respectively, and we obtain the relation

$$G_{00}(z)^{-1} \stackrel{d}{=} z - a - \frac{\mu^2}{N^{\gamma-1}} G(z) - \frac{\mu}{N^{\gamma/2}} V_{00} \ , \tag{2.9}$$

where all the randomness in the right hand side comes from $a \sim p_A(a)$ and $V_{00} \sim \mathcal{N}(0,1)$. Since all diagonal elements of $\mathbf{G}$ are statistically equivalent, eq. (2.4) establishes the distribution of G_{ii}^{-1} for every i. Looking at eq. (2.9) one immediately realises that the values $\gamma = 1$ and $\gamma = 2$ play a special role. In our region of interest $\gamma \in (1,2)$, the last term can be neglected. By taking the average of the local resolvent and using

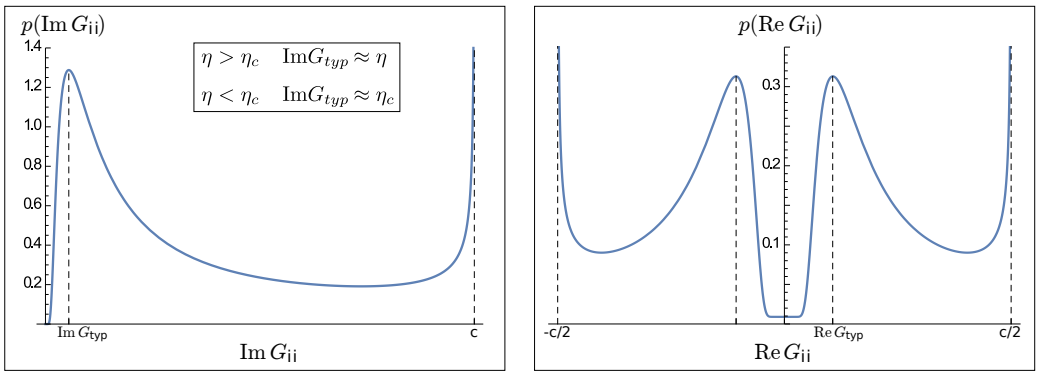

Figure 2.1: Probability distributions for the imaginary (left) and real (right) parts of the local resolvent $G_{ii}(z)$. The values $\lambda = 0$, $\eta = 0.4$ (left), $\eta = 0.15$ (right) and a standard normal distribution for p_A are used for the plots. For small $\eta > \eta_c$, $\mathrm{Im}\, G_{typ} \propto \eta$, for $\eta < \eta_c$, $\mathrm{Im}\, G_{typ} \propto \eta_c$ while $\mathrm{Re}\, G_{typ}$ is of order one in both cases. The cutoffs are controlled by $c = 1/\eta$ or $c = 1/\eta_c$ respectively.

eq. (2.9), one finds that up to corrections small in N, the global resolvent is that of A,

$$G(z) = \overline{G}(z) = \overline{G}_A(z) = \fint \frac{p_A(a)}{z-a} \mathrm{d}a \ , \tag{2.10}$$

where $\fint$ indicates the Cauchy principal value of the integral. Now that $G(z)$ is known, and is determined from p_A, the distribution of $G_{ii}(z)$ can be obtained.

We will study separately the real and imaginary parts of $G_{ii}(z)$ at $z = \lambda - \mathrm{i}\eta$, taking the large N limit with η either fixed, or scaling as $\eta \approx N^{-\delta}$ ($\delta < 1$). Up to terms that can be neglected in both cases, we derive from (2.10) the expressions

$$\mathrm{Re}\, G_{ii}(z) = \frac{\lambda - a_i}{(\lambda - a_i)^2 + \left(\eta + \frac{\mu^2}{N^{\gamma-1}} \mathrm{Im}\, \overline{G}\right)^2} \ , \tag{2.11}$$

$$\mathrm{Im}\, G_{ii}(z) = \frac{\eta + \frac{\mu^2}{N^{\gamma-1}} \mathrm{Im}\, \overline{G}(z)}{(\lambda - a_i)^2 + \left(\eta + \frac{\mu^2}{N^{\gamma-1}} \mathrm{Im}\, \overline{G}\right)^2} \ . \tag{2.12}$$

Let us first focus on the usual scaling limit that corresponds to the large N limit with η small but fixed. The second term in the numerator of (2.12) then is subleading. Neglecting it, we obtain the distribution

$$p_{\mathrm{Im}\, G}(x) = [\varphi_+(x) + \varphi_-(x)] \frac{\sqrt{\eta}}{2x^{3/2}\sqrt{1-\eta x}} \ , \tag{2.13}$$

where $\varphi_\pm(x) = p_A\left(\lambda \pm \sqrt{\eta(1/x-\eta)}\right)$. The exact distribution depends on the choice of p_A, and is plotted in Fig. 2.1 for a standard normal distribution $p_A = \mathcal{N}(0,1)$. The distribution displays some interesting features that do not depend on the specific form of p_A. It has a peak of height $\mathcal{O}(1/\eta)$ at $\operatorname{Im} G_{ii} \approx \eta$; for large $\operatorname{Im} G_{ii} \ll \eta^{-1}$ it has a power law decay

$$p_{\operatorname{Im} G}(x) \propto p_A(\lambda)\eta^{1/2}x^{-3/2} \tag{2.14}$$

with a cutoff at $x = \operatorname{Im} G_{ii} = \eta^{-1}$, where it diverges as $(\eta^{-1}-x)^{-1/2}$. Note that the $\eta \to 0^+$ limit of the distribution is singular and must be taken after the integration when computing expectation values. These features are typical of localised phases, see, *e.g.*, [64, 68]. In order to unveil that for $\gamma \in (1,2)$ the system is instead delocalised but non-ergodic, one has to study the statistics of $\operatorname{Im} G_{ii}(\lambda - \mathrm{i}\eta)$ with the scaling $\eta \approx N^{-\delta}$.

Looking at eq. (2.12), we foresee three possible behaviours, with a critical value $\eta_c = N^{1-\gamma}$ discriminating between them.

- If $\eta \gg \eta_c$ ($\delta > \gamma - 1$) then η dominates the numerator of (2.12) and the previous discussion still holds.
- If $\eta \ll \eta_c$ ($\delta < \gamma - 1$) then the $\operatorname{Im}\overline{G}$ term dominates. For finite large N the previous arguments still work, but with $\mu^2 N^{1-\gamma}\operatorname{Im}\overline{G}$ replacing η.
- In the critical case $\eta = \eta_c$, the two terms are of the same order and they both contribute to the quantity setting the scales for the probability distribution.

A similar treatment yields the statistics of $\operatorname{Re} G_{ii}(z)$. The result is qualitatively similar to the imaginary part, but more involved and perhaps less instructive. For the real part, the limit $\eta \to 0^+$ is not singular and its typical value is of order one. The typical plot for $p_{\mathrm{Re}G}(x)$ is shown in Fig. 2.1 (right).

In summary, we find that the usual scaling ($N \to \infty$ first and $\eta \to 0$ after) is blind to the existence of the non-ergodic delocalised phase, whose existence can be instead revealed focusing on $\eta = 1/N^\delta$. For any $\delta < 1$, in a standard localised phase the typical value of $\operatorname{Im} G_{ii}(x)$ is always of the order of η, whereas in a standard delocalised phase the typical value of $\operatorname{Im} G_{ii}(x)$ tends to a finite value. The behaviour in the non-ergodic delocalised phase is intermediate between these two cases: the typical value of $\operatorname{Im} G_{ii}(x)$ decreases with η, as it would happen in a localised phase, but only until the value η_c is reached. For $\eta \ll \eta_c$ it remains of the order of η_c, as it would happen in a delocalised phase (with the important difference that η_c is not of order one but vanishes as $N^{1-\gamma}$). In the next section we relate this result to the scaling of the eigenstate components using the Dyson Brownian motion technique.

2.4 Dyson Brownian motion

The Dyson Brownian motion (DBM) is a matrix-valued stochastic process in which each element of the matrix undergoes an independent Brownian motion,

$$\mathrm{d}M_{ij}(t) = \sqrt{\frac{(1+\delta_{ij})\sigma^2}{2}}\mathrm{d}W_{ij}, \tag{2.15}$$

where W_{ij} are independent standard complex Wiener processes, with $W_{ij} = W_{ji}^*$. With initial conditions $M(0) = 0$, $M(t)$ is a random GUE matrix with variance $\sigma^2 t$. This technique was in fact introduced by Dyson to study spectral properties of the Gaussian invariant ensembles [69].

If we consider instead initial conditions $M(0) = A$ and set $\sigma^2 = N^{-\gamma}$, at $t = \mu^2$ we obtain $M(\mu^2) = H$, the Hamiltonian (2.1) of the generalised Rosenzweig–Porter model. It is then possible to analyse quantities derived from H, such as eigenvalues, eigenvectors and the local resolvent, by studying their evolution equations under the Brownian motion. In the rest of this section we use the results, obtained in this way, that we need for our analysis. Their derivations are reported in Appendix 2.B.

Using perturbation theory on a discretised version of (2.15) (or equivalently Itō calculus), stochastic differential equations can be derived, describing the evolution of the eigenvalues and eigenvectors under the Brownian motion. Denoting the i-th eigenvalue (sorted in increasing order) by λ_i and the corresponding eigenvector $\psi^{(i)} = (\psi_1^{(i)}, \dots, \psi_N^{(i)})$, we obtain the stochastic differential equations [70, 71]

$$\mathrm{d}\lambda_i = \frac{1}{N^\gamma}\sum_{j\neq i}\frac{1}{\lambda_i - \lambda_j}\mathrm{d}t + \frac{1}{N^{\gamma/2}}\mathrm{d}b_i \ , \tag{2.16}$$

$$\mathrm{d}\psi^{(i)} = -\left[\sum_{j\neq i}\frac{1}{(\lambda_i-\lambda_j)^2}\right]\frac{\psi^{(i)}}{2N^\gamma}\mathrm{d}t + \frac{1}{N^{\gamma/2}}\sum_{j\neq i}\frac{\psi^{(j)}\mathrm{d}b_{ij}}{\lambda_i-\lambda_j} \ , \tag{2.17}$$

with initial conditions $\lambda_i(0) = a_i$, $\psi_j^{(i)}(0) = \delta_{ij}$. The noise terms are real (b_i) and complex ($b_{ij} = b_{ji}^*$) standard Wiener processes.

It is also useful to establish the equation verified by the following quantities [70, 71]

$$u_{i|j} = [|\psi_j^{(i)}|^2] \ , \tag{2.18}$$

where $[\cdots]$ indicates the average over the eigenvector noise b_{ij}. Since the evolution of the eigenvalues is decoupled from that of the eigenvectors, the average $[\cdots]$ does not affect the eigenvalues. Using Itō's calculus one obtains for a fixed realisation of the

eigenvalues the evolution equation [71]

$$\partial_t u_{i|j}(t) = N^{-\gamma} \sum_{k \neq i} \frac{u_{k|j}(t) - u_{i|j}(t)}{(\lambda_k - \lambda_i)^2} \ , \tag{2.19}$$

with initial conditions $u_{i|j} = \delta_{ij}$.

Resolvent and DBM

We first show that the DBM provides an alternative way to find the previous results on the resolvent for $\gamma \in (1, 2)$. To do so, we first consider the (non-averaged) eigenvalue density

$$\rho(\lambda, t) = \frac{1}{N} \sum_i \delta(\lambda - \lambda_i(t)) \ , \tag{2.20}$$

and its Stieltjes transform, the resolvent

$$G(z, t) = \int \frac{\rho(\lambda, t)}{z - \lambda} \mathrm{d}\lambda = \frac{1}{N} \operatorname{Tr} \mathbf{G}(z, t) \ . \tag{2.21}$$

Dean's equation [72] provides a way to derive from the SDE for the eigenvalues (2.16) a closed stochastic evolution equation for $\rho(\lambda, t)$. A Stieltjes transformation then gives a closed equation for $G(z, t)$, which is a stochastic complex Burgers' equation

$$\partial_t G(z, t) = -\frac{1}{N^{\gamma-1}} G(z, t) \partial_z G(z, t) + \frac{1}{N^{\gamma/2}} \bar{\eta}(z, t) \ , \tag{2.22}$$

where $\bar{\eta}$ is an order one, Gaussian noise with correlations

$$\langle \bar{\eta}(z, t) \bar{\eta}(z', t') \rangle = -\delta(t - t') \partial_z \partial_{z'} \frac{\langle G(z, t) - G(z', t') \rangle}{z - z'} \ . \tag{2.23}$$

Note that G can be written explicitly as a function of $\{\lambda_i\}$, so its evolution equation can be derived directly from eq. (2.16) using Itō's lemma [71]. The result is again a stochastic Burgers' equation, however the noise term appears in a less appealing form. While still quite complicated, the form (2.22) clarifies what the order in N of each term is, and the transitions at $\gamma = 1$ and $\gamma = 2$ appear naturally in it.

In the intermediate phase the leading term is 0, *i.e.* $G(z, t) \approx G(z, 0) = G_A(z)$ at all t, as found previously. The first correction gives a deterministic inviscid Burgers' equation, well known in random matrix theory[2] [73, 74].

[2] The treatment of the Dyson Brownian motion is normally applied to models corresponding to $\gamma = 1$ [71, 73, 74]. The standard Burgers' equation is recovered with the rescaling $t \to N^{\gamma-1} t$.

We can then focus on the local resolvent, averaged over the off-diagonal noise W_{ij} only [71]:

$$U_j(z,t) = [G_{jj}(z,t)] = \sum_i \frac{u_{i|j}}{z - \lambda_i(t)} \ . \tag{2.24}$$

The evolution equation for U_j is derived from equations (2.16,2.19) again using Itō's lemma (see Appendix 2.B). The resulting stochastic equation (2.62) has a structure similar to (2.22). Keeping only the leading term in N for $\gamma \in (1,2)$, we obtain the evolution equation

$$\partial_t U_j(z,t) = -\frac{1}{N^{\gamma-1}} G_A(z) \partial_z U_j(z,t) \ . \tag{2.25}$$

The evolution is deterministic, and the randomness in U_j comes only from the initial condition $U_j(z,0) = 1/(z-a_j)$. The solution to (2.25) is

$$U_j(z,t)^{-1} = z - a_j - \frac{t}{N^{\gamma-1}} G_A(z) \ . \tag{2.26}$$

Comparing with equations (2.11,2.12), the result evaluated at $t = \mu^2$ coincides with what we obtained for the local resolvent G_{ii} from the recurrence equation (2.4). With that technique it is not necessary to take the $[\dots]$-expected value, which confirms that G_{ii} is self-averaging for large N with respect to the W_{ij}s.

2.5 Eigenvectors delocalisation and statistics of the local resolvent

In order to understand the amount of delocalisation of the eigenvectors we focus on the solution of (2.19) at $t = \mu^2$. To extract information on the region of the Hilbert space over which the eigenstates are delocalised, we consider the following ansatz, inspired by the results on the statistics of the local resolvent and of Ref. [52]. Assume that $u_{i|j}$ is of order $N^{-\alpha}$ for $|i-j| \approx N^{\alpha}$ and much smaller on the remaining $\approx N - N^{\alpha}$ sites. Then the sum in (2.19) has N^{α} contributions, each of which is of order $N^{-2\alpha+2}$ because $\lambda_i - \lambda_j \approx N^{\alpha-1}$. Hence

$$\partial_t u_{i|j} \approx \frac{1}{N^{\gamma}} N^{\alpha} \cdot N^{-\alpha} N^{2-2\alpha} \overset{!}{\approx} N^{-\alpha} \ , \tag{2.27}$$

showing that the ansatz is consistent only if $\alpha = 2 - \gamma$ and thus establishing that the eigenvectors are delocalised but only on $N^{2-\gamma}$ sites. This result supports the picture that going from the localised to the intermediate phase the states spread from a single site to $\approx N^{2-\gamma}$ states closest in energy, and is compatible with the result of

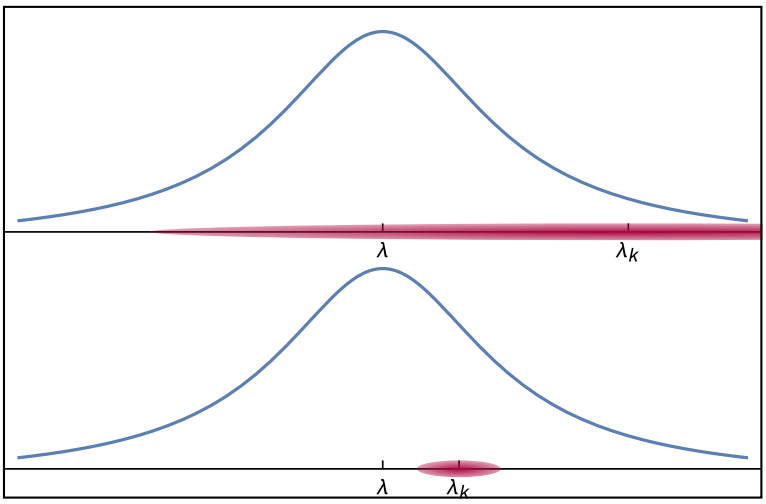

Figure 2.2: Representation of the packet picture for the contributions to $\operatorname{Im} G_{ii}$, see eq. (2.28). The shaded area represents the packet associated to the level λ_k, of width $\approx \eta_c = N^{1-\gamma}$. The width of the Lorentzian is η. If $\eta > \eta_c$ (lower panel) all the levels in the packet contribute approximatively the same. If $\eta < \eta_c$ (upper panel) this is no longer the case.

Ref. [52] for the fractal dimension of the eigenstates. Correspondingly, the eigenvalues are correlated if their distance is of order $N^{1-\gamma}$ or less, but become uncorrelated on larger scales. Hence one expects Poisson-like statistics on larger scales in agreement with the results found in Ref. [52].

We now show that these insights provide a natural explanation of the statistics of the local resolvent found previously. The imaginary part of the local resolvent is given by the sum

$$\operatorname{Im} G_{ii}(\lambda - \mathrm{i}\eta) = \sum_k \frac{|\psi_k^{(i)}|^2 \eta}{(\lambda - \lambda_k)^2 + \eta^2} \ . \tag{2.28}$$

The k-th level's contribution to the sum is given by two factors: the eigenvector weight $|\psi_k^{(i)}|^2$, and a weight depending on λ_k as a Lorentzian centred in λ. In the completely localised phase ($\gamma > 2$) $|\psi_k^{(i)}|^2 = \delta_{ki}$, so only λ_i contributes. For large N, $\lambda_i \approx a_i$ is drawn randomly from p_A. If λ is in the bulk of the spectrum, typically $|\lambda - \lambda_i| \approx 1$, giving a peak of the distribution at $\operatorname{Im} G_{ii} \approx \eta$. If instead $|\lambda - \lambda_i| \lesssim \eta$, which happens with probability $\propto p_A(\lambda)\eta$, then $\operatorname{Im} G_{ii} \lesssim 1/\eta$. These are the rare fluctuations that populate the tail of the distribution close to the cutoff at $1/\eta$. In between there is the regime $1 \ll |\lambda - \lambda_i| \ll \sqrt{\eta}$, where the density of states is approximately constant, corresponding to the power law $\propto p_A(\lambda) \operatorname{Im} G^{-3/2}$.

We now turn to our region of interest: the delocalised non-ergodic phase $1 < \gamma < 2$. From the the previous discussion on eigenvector delocalisation, we know that the leading contribution comes from $\approx N^{2-\gamma}$ levels, which come in "packets" (or mini-bands) of eigenvalues of width $\eta_c = N^{1-\gamma}$, centred around λ_i. For large enough N and $\eta_c \ll \eta \ll 1$, the width of the packet is much smaller than that of the Lorentzian, so the packet behaves coherently, with all the eigenvalues in the packet being close to λ if and only if λ_k is, and so on (see Fig. 2.2 - lower panel). The total contribution from the packet is identical to the single-level contribution in the localised phase. In particular, the typical value of the local resolvent is of the order of η. This explains the result we found for $\eta_c \ll \eta \ll 1$, see eq. (2.13).

The picture changes when the width of the Lorentzian becomes smaller than that of the eigenvalue packet. In this case, the probability that the Lorentzian overlaps with the packet is of order η_c. When this happens, the sum over k in (2.28) is of the order of $1/\eta_c$ independently of the value of η as long as $\eta > 1/N$. States which are $O(1)$ away from the centre of the Lorentzian are only important in determining the typical value of $\operatorname{Im} G_{ii}$: their weights are of order $N^{-\gamma}$ [52, 70] and hence their overall contribution leads to the result $\operatorname{Im} G_{typ} \sim N^{1-\gamma} = \eta_c$ found previously.

2.6 Conclusion and further developments

We investigated the localisation properties of the generalised Rosenzweig–Porter model, using a recurrence relation for the local resolvent and the Dyson Brownian motion. Our main focus was the non-ergodic delocalised phase unveiled in Ref. [52], of which we confirmed the existence using complementary techniques. Interpreting the model as the combination of on-site random energies a_i and a structurally disordered hopping, we found that each eigenstate is delocalised over $N^{2-\gamma}$ sites close in energy $|a_j - a_i| \leq N^{1-\gamma}$, in agreement with the fractal properties found in Ref. [52].

The other main result of our work is the characterisation of the statistics of the local resolvent in the non-ergodic delocalised phase. In particular, we showed that its existence can be revealed studying a non-standard scaling limit in which the small additional imaginary part η vanishes as $1/N^{\delta}$. The value η_c at which the statistics displays a cross-over from a behaviour characteristic of standard localised phases to a behaviour similar to the one of standard delocalised phases is equal to the typical level spacing, $1/N$, times the number of sites, $N^{2-\gamma}$, over which the eigenvectors are delocalised. Thus, from the local resolvent statistics one has a direct access to the non-ergodic properties of the delocalised phase. After the completion of this work, we

became aware of [25] in which the statistics of the local resolvent in a non-standard scaling limit is also proposed and used to probe the existence of a delocalised non-ergodic phase. However, the type of cross-over and of non-ergodic delocalised phase are different from the ones studied in this work. In the case studied in [25], the delocalised non-ergodic phase should have a typical imaginary part of the local resolvent that does not vanish in the large N limit, moreover below a cross-over scale η_c the local resolvent, i.e. the local density of states, should cease to be a smooth function. This is a distinct cross-over from the one found in our work, signalling that the two non-ergodic delocalised phases are different.

The analysis presented was carried out at a physics level of rigour. However, one of the reason for choosing the Dyson Brownian motion technique was that it lends itself to a rigorous formalisation. Indeed, in [75] von Soosten and Warzel proved rigorously the existence of the extended, non-ergodic phase, and that the eigenstates are fractal of dimension $N^{2-\gamma}$. Their proof is based on the Dyson Brownian motion equations for the resolvent (2.22,2.62), which were proven for a related model in a previous work by the same authors [76].

In this work we only considered static (spectral) properties of the model. The characterisation of ergodicity is then implied by the fact that in quantum mechanics, the dynamics is controlled by the eigenstates,but we did not discuss it by looking explicitly at the time evolution. Our results provide a glimpse into the dynamics through the following estimate. Consider the time evolution of a state ϕ initially localised at site k, $\phi_j(0) = \delta_{jk}$. The survival probability at time t can be written in terms of the eigenvalues and eigenvectors,

$$|\phi_k(t)|^2 = \sum_{l,m} |\psi_k^{(m)}|^2 |\psi_k^{(l)}|^2 \, \mathrm{e}^{-\mathrm{i}(\lambda_m - \lambda_l)t} \tag{2.29}$$

According to the packet picture, only the terms with both λ_m, λ_l close to λ_k contribute, and they do so approximately with the same amplitude, and a random phase oscillating with frequency $\lambda_k - \lambda_l$, with typical value of order $N^{1-\gamma}$. This gives a timescale for decay (destructive interference) of order $t_d \approx N^{\gamma-1}$. For $\gamma > 1$ the timescale diverges with N, showing that both the intermediate and the localised phases are indeed non-ergodic. Both the non-ergodicity and the scaling of t_d were confirmed by detailed numerical analysis based on exact diagonalisation, see [77, 78].

Appendix

2.A The resolvent

A central object of the work presented here and of random matrix theory in general is the resolvent matrix at $z = \lambda - \mathrm{i}\eta$,

$$\mathbf{G}(z) = (z - H)^{-1} = \sum_k \frac{|\psi^{(k)}\rangle \langle\psi^{(k)}|}{\lambda - \lambda_k - \mathrm{i}\eta} \tag{2.30}$$

where $\{\lambda_k\}$ and $\psi^{(k)}$ are the eigenvalues of H and the corresponding eigenvectors. Its trace $G(z) = \operatorname{Tr}\mathbf{G}(z)/N$ is (somewhat confusingly) also called the resolvent. This object can be defined for any random matrix. If H is a Hamiltonian, $\mathbf{G}$ is the corresponding Green function in the energy (or frequency) domain. Its first application in random matrix theory comes from the observation that

$$\operatorname{Im} G(z) = \frac{1}{N}\sum_k \frac{\eta}{(\lambda - \lambda_k) + \eta^2} \xrightarrow{\eta\to 0^+} \frac{\pi}{N}\sum_k \delta(\lambda - \lambda_k) = \pi\hat{\rho}(\lambda) \tag{2.31}$$

gives the empirical density of states. Each term in the sum is a Lorentzian of width η, converging to a δ-function in the $\eta \to 0^+$ limit. This makes more precise the statement that the distribution of $\mathbf{G}$ (as a random function of z) encodes the spectral properties of H around λ, averaged over a width η.

In this work we focused on the distribution of the imaginary part of the *local* resolvent, the diagonal elements of $\mathbf{G}$, which is related to the *local* density of states (see Eq. 2.28)

$$\operatorname{Im} G_{ii}(z) \xrightarrow{\eta\to 0^+} \frac{\pi}{N}\sum_k |\psi_k^{(i)}|^2 \delta(\lambda - \lambda_k) = \pi\hat{\nu}^{(i)}(\lambda)\ . \tag{2.32}$$

This gives some intuition on the use of the statistics of the local resolvent to study localisation properties. The density of states (2.31) is self-averaging. If the states are delocalised, their contribution to (2.32) is more or less the same at all sites i, and we expect typical values of $\hat{\nu}^{(i)}$ to be the same as the global density of states. Therefore the local density of states is also self-averaging. On the other hand it the

states are localised, the local density of states is typically zero, except when $\lambda \approx \lambda_i$ ("resonance"). Therefore in the $\eta \to 0$ limit the distribution is singular, with typical values of order η and a tail given by the resonances. In the main text we extend this intuition to the extended, non-ergodic phase.

2.B Dyson Brownian motion

This appendix collects derivations of the stochastic differential equations for the evolution of various quantities under the Dyson Brownian motion (2.15).

2.B.1 Itō calculus

Consider a Wiener process W over $[0, T]$, the corresponding measure $\mathrm{d}W$ and the discretisation with timestep Δ, $\eta_i \sim \mathcal{N}(0, \Delta)$. The sum $\hat{W} = \sum_{i=1}^{T/\Delta} \eta_i$ is distributed as $\mathcal{N}(0, T)$ and converges to W in the continuum limit.

The quantity $s = \sum_{i=1}^{T/\Delta} \eta_i^2$ on the other hand is a sum of Gamma-distributed variables with mean Δ and variance $2\Delta^2$. Due to the CLT, in the continuum limit $s \sim \mathcal{N}(T, 2T\Delta) \to \mathcal{N}(T, 0)$, i.e. the fluctuations vanish and $s = T$ deterministically. For this reason in Itō calculus

$$(\mathrm{d}W)^2 = \mathrm{d}t, \tag{2.33}$$

while other second order differentials are neglected (including products of independent Wiener processes).

Consider a multivariate Itō drift-diffusion process $\mathbf{X}$ with

$$\mathrm{d}\mathbf{x} = \mathbf{f}(\mathbf{x}, t)\mathrm{d}t + \mathbb{G}(\mathbf{x}, t)\mathrm{d}\mathbf{W}, \tag{2.34}$$

where $\mathbf{f}$ is $\mathbb{R}^n$-valued, $\mathbf{W}$ a vector of m independent Wiener processes and $\mathbb{G}$ is $n \times m$ matrix-valued. A function $h(\mathbf{x}, t)$ can be Taylor expanded

$$\mathrm{d}h = \vec{\nabla} h \cdot \mathrm{d}\mathbf{x} + \partial_t h \mathrm{d}t + \frac{1}{2}\mathrm{d}\mathbf{x}^T \cdot \nabla^2_{\mathbf{xx}} h \cdot \mathrm{d}\mathbf{x} + \mathcal{O}(\mathrm{d}t^{3/2}). \tag{2.35}$$

where $\nabla^2_{\mathbf{xx}} h$ is the Hessian matrix of h with respect to $\mathbf{x}$. Using (2.33,2.34), we obtain the following formula for the change of variable in SDEs, known as Itō's lemma:

$$\mathrm{d}h = \left[\vec{\nabla}_{\mathbf{x}} h \cdot \mathbf{f} + \partial_t h + \frac{1}{2}\operatorname{Tr}\left(\mathbb{G}\mathbb{G}^T \nabla^2_{\mathbf{xx}} h\right)\right]\mathrm{d}t + \vec{\nabla}_{\mathbf{x}} h \cdot \mathbb{G} \cdot \mathrm{d}\mathbf{W}, \tag{2.36}$$

2.B.2 Eigenvalues and eigenvectors

Consider one step of the Dyson Brownian motion (2.15), discretised with timestep Δ,

$$M(t+\Delta) = M(t) + \frac{1}{N^{\gamma/2}}\delta M \tag{2.37}$$

where δM is a GUE matrix with variance $\langle|\delta M_{ij}|^2\rangle = \Delta(1+\delta_{ij})/2$. With Δ as a small parameter, we can consider δM as a perturbation and use second order time-independent perturbation theory [79], to express the eigenvalues and eigenvectors of $M(t+\Delta)$ in terms of those of $M(t)$,

$$\lambda_i(t+\Delta) = \lambda_i + \frac{1}{N^{\gamma/2}}\delta M_{ii} + \frac{1}{N^{\gamma}}\sum_{j\neq i}\frac{|\delta M_{ij}|^2}{\lambda_i-\lambda_j} + \mathcal{O}(\Delta^{3/2}) \tag{2.38}$$

$$\begin{aligned}\psi_i(t+\Delta) = \psi_i + \frac{1}{N^{\gamma/2}}\sum_{j\neq i}\frac{\delta M_{ij}}{\lambda_i-\lambda_j}\psi_j - \frac{1}{2N^{\gamma}}\left[\sum_{k\neq i}\frac{|\delta M_{ik}|^2}{(\lambda_i-\lambda_k)^2}\right]\psi_i \\ + \frac{1}{N^{\gamma}}\sum_{k\neq i}\left[\sum_{l\neq i}\frac{\delta M_{kl}\delta M_{li}}{(\lambda_i-\lambda_k)(\lambda_k-\lambda_l)} - \frac{\delta M_{ii}\delta M_{ki}}{(\lambda_i-\lambda_k)^2}\right]\psi_k + \mathcal{O}(\Delta^{3/2}).\end{aligned} \tag{2.39}$$

For $\Delta \to 0$ we recover the continuous time stochastic processes, $\lambda_i(t+\Delta)-\lambda_i \to \mathrm{d}\lambda_i$ *etc*, and $\delta M_{ij} \to \mathrm{d}W_{ij}$, where W_{ij} are independent standard Wiener processes with $W_{ij} = W^*_{ji}$. Therefore $|\delta M^2_{ij}| \to \mathrm{d}t$, while the other second order terms vanish, leading to the stochastic differential equations (2.16,2.17).

2.B.3 Resolvent and Dean's equation

Using Itō's formula (2.36) and the SDE for the eigenvalues (2.16), the evolution equation for the (global) resolvent $G(z,t) = \mathrm{Tr}(z-H(t))^{-1}/N$ takes the form

$$\mathrm{d}G(z,t) = \underbrace{\left[\frac{1}{N^{\gamma}}\sum_{\langle i,j\rangle}\frac{\partial_{\lambda_i}G}{(\lambda_i-\lambda_j)} + \frac{1}{2N^{\gamma}}\sum_i \partial^2_{\lambda_i}G\right]}_{F}\mathrm{d}t + \frac{1}{N^{1+\gamma/2}}\sum_i\frac{\mathrm{d}W_i}{(z-\lambda_i)^2}. \tag{2.40}$$

The resolvent is expressed as a function of the eigenvalues as

$$G(z,t) = \frac{1}{N}\sum_i \frac{1}{z-\lambda_i(t)}, \tag{2.41}$$

from which the following identities are derived:

$$\sum_i \partial_{\lambda_i} G = -\partial_z G \tag{2.42}$$

$$\begin{aligned}\frac{1}{2N}\partial_z^2 G =& \frac{1}{N}\sum_i \frac{\partial_{\lambda_i} G}{z-\lambda_i} = \frac{1}{N}\sum_{i,j}\frac{\partial_{\lambda_i} G}{z-\lambda_j} - \frac{1}{N}\sum_{\langle i,j\rangle}\frac{\partial_{\lambda_i} G}{z-\lambda_j} \\ =& -G\partial_z G - \frac{1}{N}\sum_{\langle i,j\rangle}\frac{\partial_{\lambda_i} G}{z-\lambda_j}.\end{aligned} \tag{2.43}$$

The term in square brackets in (2.40) can be written as

$$\begin{aligned}F =& -\frac{1}{N^{\gamma-1}} G\partial_z G + \frac{1}{N^{\gamma}}\sum_{\langle i,j\rangle}\partial_{\lambda_i} G\left(\frac{1}{\lambda_i-\lambda_j} - \frac{1}{z-\lambda_j}\right) \\ =& -\frac{1}{N^{\gamma-1}} G\partial_z G + \frac{1}{N^{\gamma+1}}\sum_{\langle i,j\rangle}\frac{1}{(\lambda_i-\lambda_j)(z-\lambda_i)(z-\lambda_j)} \\ =& -\frac{1}{N^{\gamma-1}} G\partial_z G\end{aligned} \tag{2.44}$$

where the sum vanishes because the terms in the sum are antisymmetric in $i \leftrightarrow j$. This leads to the stochastic Burgers' equation as found in the literature [71],

$$\mathrm{d}G(z,t) = -\frac{1}{N^{\gamma-1}} G(z,t)\partial_z G(z,t)\mathrm{d}t + \frac{1}{N^{1+\gamma/2}}\sum_i \frac{\mathrm{d}W_i}{(z-\lambda_i)^2}. \tag{2.45}$$

An alternative way to derive the evolution equation for G, leading to the characterisation of the noise in (2.23), is based on Dean's equation [72]. Given a generic many-particle system undergoing Langevin dynamics with pairwise interactions described by a potential, Dean's equation provides a closed integro-differential stochastic equation for the density ρ. The eigenvalue evolution (2.16) is a particular case of such a process, for which Dean's equation reads

$$\partial_t \rho(\lambda,t) = \frac{1}{N^{\gamma/2}}\partial_\lambda\left[\eta(\lambda,t)\sqrt{\rho(\lambda,t)}\right] - \frac{1}{N^{\gamma}}\partial_\lambda\left[\rho(\lambda,t)G(\lambda,t)\right] - \frac{1}{2N^{\gamma}}\partial_\lambda^2\rho(\lambda,t) \tag{2.46}$$

where η is a unit variance Gaussian white noise $\langle \eta\eta' \rangle = \delta(\lambda - \lambda')\delta(t - t')$. The appearance of G in (2.46) is not a generic feature of Dean's equation: it is a consequence of the specific form of the inter-particle potential, the "Coulomb gas" interaction typical of random matrix theory [80]. For a generic potential V, the drift term of Dean's equation involves the convolution $\rho \star V'$.

A Stieltjes transformation of (2.46) converts it to an equation for $G(z,t)$. With manipulation mirroring the derivation above, it can be cast again in the form of a stochastic Burgers' equation,

$$\partial_t G(z,t) = -\frac{1}{N^\gamma}\partial_z \int\int \frac{\rho(\lambda,t)\rho(\lambda',t)}{(z-\lambda)(\lambda-\lambda')}\mathrm{d}\lambda\mathrm{d}\lambda' + \frac{1}{2N^\gamma}\partial_z^2 G(z,t) + noise \tag{2.47}$$

$$= -\frac{1}{N^{\gamma-1}} G(z,t)\partial_z G(z,t) + \frac{1}{N^{\gamma/2}}\bar{\eta}(z,t). \tag{2.48}$$

The noise term can be treated in the following way. A cleaner way to describe the noise (avoiding taking the square root of ρ) is to write the first term in Dean's equation (2.46) as $\partial_\lambda \tilde{\eta}(\lambda,t)$, where $\tilde{\eta}$ is Gaussian with correlation $\langle \tilde{\eta}\tilde{\eta}' \rangle = \delta(t-t')\delta(\lambda-\lambda')\rho(\lambda,t)$. Note that the ρ here is still a stochastic quantity, the same for which eq. (2.46) holds. Averages on the noise are taken conditionally on ρ. When taking the Stieltjes transformation the noise term then becomes

$$\bar{\eta}(z,t) = \int \frac{\partial_\lambda \tilde{\eta}(\lambda,t)}{z-\lambda}\mathrm{d}\lambda = \partial_z \int \frac{\tilde{\eta}(\lambda,t)}{z-\lambda}\mathrm{d}\lambda \tag{2.49}$$

which is Gaussian with correlation function

$$\langle \bar{\eta}(z,t)\bar{\eta}(z',t') \rangle = \partial_z\partial_{z'} \int \frac{\langle \tilde{\eta}(\lambda,t)\tilde{\eta}(\lambda',t') \rangle}{(z-\lambda)(z'-\lambda')}\mathrm{d}\lambda\mathrm{d}\lambda' \tag{2.50}$$

$$= -\delta(t-t')\partial_z\partial_{z'}\left(\frac{G(z,t)G(z',t)}{z-z'}\right) \tag{2.51}$$

This makes eq. (2.48) a closed equation for G and clarifying the relative order of the terms, as discussed in the main text.

2.B.4 Overlaps and local resolvent

Consider the squared overlaps of the i-th eigenstate at time t on the j-th localised state $\psi_j^A = \psi_j(0)$,

$$\hat{u}_{i|j} = \left|\left(\psi_i(t), \psi_j^A\right)\right|^2, \qquad u_{i|j}(t) = \left[\hat{u}_{i|j}\right], \tag{2.52}$$

where $[\dots]$ indicates the average over the eigenvector (off-diagonal) noise only. Using Itō's formula and the equation for the eigenvector process (2.17) we derive

$$\mathrm{d}\hat{u}_{i|j} = -\frac{1}{n^{2\gamma}}\sum_{k\neq i}\frac{1}{(\lambda_i-\lambda_k)^2}\left(\psi_i(t),\psi_j^A\right)\left(\psi_j^A,\psi_i(t)\right) \tag{2.53}$$

$$+\frac{1}{n^{2\gamma}}\sum_{k\neq i}\frac{1}{(\lambda_i-\lambda_k)^2}\,\mathrm{Tr}\left[\psi_k(t)\psi_k(t)^\dagger\psi_j^A\psi_j^{A\dagger}\right]\mathrm{d}t + noise. \tag{2.54}$$

Note that in the first two terms $\hat{u}_{i|j}$ and $\hat{u}_{k|j}$ appear respectively, and the noise has zero mean. Taking the $[\cdot]$-average we obtain

$$\frac{\partial u_{i|j}}{\partial t} = \frac{1}{n^{2\gamma}}\sum_{k\neq i}\frac{[|(\psi_k(t),\psi_j^A)|^2-|(\psi_i(t),\psi_j^A)|^2]}{(\lambda_i-\lambda_k)^2} = \frac{1}{n^{2\gamma}}\sum_{k\neq i}\frac{u_{k|j}-u_{i|j}}{(\lambda_i-\lambda_k)^2}\,. \tag{2.55}$$

The mean squared overlaps can be used to define the local density of states

$$\nu^{(j)}(\lambda,t) = \sum_i u_{i|j}\delta(\lambda-\lambda_i(t)) \tag{2.56}$$

and its Stieltjes transform, the local resolvent

$$U^{(j)}(z,t) = \left[\langle\psi_j^A|(z-H)^{-1}|\psi_j^A\rangle\right] = \int\frac{\nu^{(j)}(\lambda,t)}{z-\lambda}\mathrm{d}\lambda = \sum_i\frac{u_{i|j}}{z-\lambda_i(t)}. \tag{2.57}$$

From this expression we can again use Itō's lemma and the evolution equations (2.16,2.55) to find

$$\mathrm{d}U^{(j)}(z,t) = \frac{1}{N^\gamma}\underbrace{\left[\sum_{\langle i,k\rangle}\frac{u_{k|j}-u_{i|j}}{(z-\lambda_i)(\lambda_i-\lambda_k)^2}+\sum_{\langle i,k\rangle}\frac{u_{i|j}}{(z-\lambda_i)^2(\lambda_i-\lambda_k)}+\sum_i\frac{u_{i|j}}{(z-\lambda_i)^3}\right]}_{F'}\mathrm{d}t$$

$$+\frac{1}{N^{\gamma/2}}\sum_i\frac{u_{i|j}\mathrm{d}W_i}{(z-\lambda_i)^2}. \tag{2.58}$$

With the identities

$$\begin{aligned}\sum_i\frac{u_{i|j}}{(z-\lambda_i)^3} &= \sum_{i,k}\frac{u_{k|j}}{(z-\lambda_i)(z-\lambda_k)^2}-\sum_{\langle i,k\rangle}\frac{u_{k|j}}{(z-\lambda_i)(z-\lambda_k)^2}\\ &= -NG(z,t)\partial_z U^{(j)}(z,t)-\sum_{\langle i,k\rangle}\frac{u_{k|j}}{(z-\lambda_i)(z-\lambda_k)^2}\end{aligned} \tag{2.59}$$

we see that

$$F' = -NG\partial_z U + \sum_{\langle i,k \rangle} s_{ik} \tag{2.60}$$

with

$$s_{ik} = \frac{u_{k|j}}{(z-\lambda_k)(\lambda_k-\lambda_i)^2} - \frac{u_{i|j}}{(z-\lambda_i)(\lambda_k-\lambda_i)^2} \ . \tag{2.61}$$

The sum in (2.60) vanishes since s_{ik} is antisymmetric, and we obtain the stochastic evolution equation for the local resolvent

$$\mathrm{d}U^{(j)}(z,t) = -\frac{1}{N^{\gamma-1}} G(z,t)\partial_z U^{(j)}(z,t)\mathrm{d}t + \frac{1}{N^{1+\gamma/2}} \sum_i \frac{u_{i|j}\mathrm{d}W_i}{(z-\lambda_i)^2}, \tag{2.62}$$

which correctly reproduces the result found in the literature for $\gamma = 1$ [71].

3 p-spin and random energy models

Mean-field disordered spin models have been long studied in the field of spin glasses, both at the classical and quantum levels (see the brief discussions in Sec. 1.4 and Chapter 4). The interest in quantum spin-glass models in this work is due to the fact that recently they have been investigated in the context of many-body localisation, with the goal of comparing their unitary dynamics to that of low-dimensional models with MBL [39–43]. In particular, it is interesting to compare the "glassy" point of view of configurations clustering into pure states with the quantum phenomenon of localisation. Before exploring these ideas in Chapter 4, we take here a detour on purely classical models.

In this chapter we consider the classical p-spin model and the random energy model (REM), the exactly solvable "simplest spin glass" emerging in the $p \to \infty$ limit [36–38]. We first review the analysis of the microcanonical entropy at the replica-symmetric level for both models, and the replica symmetric canonical calculation for the REM, arguably one of the simplest replica calculations.

We then present a calculation of the overlap-resolved entropy, and numerically solve the equations at the one-step replica symmetry breaking (1RSB) level. This is a new result, improving on the annealed calculation found in the literature. It gives insight into the energy landscape of the models and provides an alternative derivation of the dynamical transition, which agrees with other methods, and sets the stage for a discussion of the difference between dynamical and clustering transitions at the classical level. Some implications on the properties of eigenstates of quantum spin glass models are discussed in Chapter 4.

3.1 Equilibrium analysis

Consider the p-spin model of N Ising spins $\sigma_i = \pm 1$, with p-body random interactions

$$H = -\sum_{i_1<\cdots<i_p} J_{i_1\cdots i_p}\sigma_{i_1}\cdots\sigma_{i_p} \tag{3.1}$$

The symmetric couplings $J_{i_1\dots i_p}$ are i.i.d. Gaussian random variables with zero mean and variance $J^2/2p!N^{p-1}$. The energy levels associated to each spin configuration are sums of such random variables, and therefore Gaussian as well. A derivation of the joint probability of energies is given in Section 3.1.2. The probability distribution of the energy of any configuration is

$$P(E) = \frac{1}{\sqrt{N\pi J^2}}\, \mathrm{e}^{-\frac{E^2}{NJ^2}} \,. \tag{3.2}$$

Given any two configurations, their two-level probability distribution is Gaussian

$$P(E_1, E_2) \propto \exp\left[-\frac{(E_1+E_2)^2}{2NJ^2(1+q^p)} - \frac{(E_1-E_2)^2}{2NJ^2(1-q^p)}\right] \,. \tag{3.3}$$

Notice that the covariance of E_1 and E_2 depends only on the overlap $q \in [-1,1]$ between them, being equal to q^p. Therefore in the $p \to \infty$ limit the energies of two distinct configurations become uncorrelated. This corresponds to the random energy model, a system with 2^N independent energy levels, distributed according to (3.2).

In the following we denote by $\langle\cdot\rangle$ the average over the couplings in (3.1). The dependence on J is sometimes retained, but we generally set $J = 1$, *i.e.* we express energies and temperatures in units of J.

3.1.1 Random energy model

Working in the microcanonical ensemble, let $n(E)\delta E$ be the random variable counting how many energy levels are in the interval $(E, E+\delta E)$. Since the energy levels are uncorrelated, for $\delta E \to 0$

$$\langle n(E)\rangle = 2^N P(E) = \mathrm{e}^{N(\log(2)-\varepsilon^2)} \tag{3.4}$$

where $\varepsilon = E/(JN)$ is a reduced energy density. The average number of states at energy ε either grows of decay exponentially with N, depending on whether $|\varepsilon|$ is larger or smaller than $\varepsilon_c = \sqrt{\log(2)}$. Notice that the typical value extracted from (3.2) is of order $\sqrt{N}$, but the spectrum is extensive, with ground state energy $-N\varepsilon_c$. The ground state energy is distributed according to the extreme value statistics of the Gaussian distribution [81]. The largest (smallest) value of $M = 2^N$ i.i.d. Gaussians follows a Gumbel distribution with average $\pm\log M = \pm N\varepsilon_c$ and fluctuations of order $1/N$.

If $|\varepsilon| < \varepsilon_c$, the number of levels is exponentially large. The fluctuations of $n(E)$ are of order $\sqrt{\langle n(E)\rangle} \ll \langle n(E)\rangle$, so the level density is self-averaging. The average

entropy density is given by

$$\langle s(\varepsilon)\rangle \approx \frac{1}{N}\log\langle n(E)\rangle = \log(2) - \varepsilon^2 \ . \tag{3.5}$$

This expression becomes negative, and thus unphysical, for $\varepsilon < -\varepsilon_c$. This is because it is the result of an *annealed* calculation. For $|\varepsilon| > \varepsilon_c$ there are typically $n(E) = 0$ states, with exponentially rare fluctuations.

The free energy density is obtained from (3.5) with standard thermodynamics equalities $\mathrm{d}s/\mathrm{d}\varepsilon = 1/T$, $f = \varepsilon - Ts$, giving

$$f = \begin{cases} -T\log 2 - \frac{J^2}{4T} & T > T_c = \frac{J}{2\sqrt{\log 2}} \\ -J\sqrt{\log 2} = -\varepsilon_c & T < T_c \ . \end{cases} \tag{3.6}$$

Below a critical temperature T_c corresponding to the slope of $s(\varepsilon)$ at ε_c, where $s(\varepsilon_c) = 0$, the system is frozen, and the free energy is equal to the ground state energy.

The replica method

To perform the *quenched* calculation for the free energy, the replica method can be used, consisting in computing moments of the partition function and using the identity

$$\langle \log Z\rangle = \lim_{n\to 0}\frac{1}{n}\log\langle Z^n\rangle \ . \tag{3.7}$$

The moments are computed for all positive integers n by considering n copies (replicas) of the system. The replicas are independent, but averaging over the disorder induces an effective interaction between them. Note that using (3.7) requires an analytic continuation to real n. This analytic continuation is in general not unique, and is the origin of many odd features of replica calculations that make the method non rigorous. However, it has proven to be a powerful computational method, and some of its predictions have been proved rigorously, including the solution of the SK and p-spin models, spawning an active area of research in mathematics [82].

The REM was analysed by Gross and Mézard [38] using the replica approach for the p-spin model and taking the large p limit. Here we summarise a simpler approach, working directly with the REM energy levels, that illustrates some essential features of replica calculations, while giving a slightly different perspective, following [33].

The replicated partition function can be written explicitly

$$Z^n = \sum_{i_1 \dots i_n} \mathrm{e}^{-\beta \sum_{a=1}^n E_{i_a}} = \sum_{i_1 \dots i_n} \mathrm{e}^{-\beta \sum_j E_j \sum_{a=1}^n \delta_{i_a j}} \tag{3.8}$$

where the sums over indices i_a run from 1 to 2^N. Averaging over the disorder,

$$\langle Z^n \rangle = \sum_{i_1 \dots i_n} \mathrm{e}^{\frac{\beta^2 N}{4} \sum_j \left(\sum_{a=1}^n \delta_{i_a j}\right)^2} = \sum_{i_1 \dots i_n} \mathrm{e}^{\frac{\beta^2 N}{4} \sum_{a,b=1}^n \delta_{i_a i_b}} . \tag{3.9}$$

The averaged replicated partition function is given by a sum of 2^{nN} terms, each of which depends on the number of equal indices, *i.e.* on whether the replicas are in the same configuration. The *replica symmetric* (RS) ansatz consists in considering only the symmetric terms in the sum with all indices distinct, giving a contribution

$$2^N 2^{N-1} \dots 2^{N-n+1} \, \mathrm{e}^{\beta^2 N n/4} \approx \exp\left[N n \beta \left(\frac{\beta}{4} + \frac{\log 2}{\beta} \right) \right] , \tag{3.10}$$

which indeed leads to a free energy that agrees with the high temperature result (3.6). As shown earlier, the RS solution becomes unphysical below T_c. This means that other contributions dominate the sum (3.9), breaking the symmetry between replicas. We consider a *one-step replica symmetry breaking* (1RSB) ansatz, in which the replicas are divided in n/m groups of m replicas, and two indices are equal if and only if they belong to replicas in the same group. The integer parameter m is then analytically continued together with n, and maximised to determine the saddle point. The 1RSB contribution is

$$\langle Z^n_{1RSB} \rangle \approx \max_m 2^{Nn/m} \, \mathrm{e}^{\beta^2 N n m/4} = \max_m \exp\left[N n \left(\frac{\log 2}{m} + \frac{\beta^2 m}{4} \right) \right] . \tag{3.11}$$

where the maximum is taken over $m \in [0, 1]$. The maximum point is

$$m^* = \frac{2}{\beta} \sqrt{\log 2} = \frac{T}{T_c} . \tag{3.12}$$

For $T > T_c$ the leading contribution is given by $m = 1$ and the RS contribution is recovered (all indices are different). On the other hand if $T < T_c$ the free energy density is $-\sqrt{\log 2}$, in agreement with the low temperature result of (3.6).

3.1.2 Distribution of energies of the p-spin model

Consider k spin configurations $\sigma^a = \{\sigma_i^a\}_{i=1\dots N}$ for $a = 1 \dots k$. The joint probability density function for their energy densities $\boldsymbol{\varepsilon} = (\varepsilon_1 \dots \varepsilon_k)$ is given by

$$p_k(\boldsymbol{\varepsilon}) = \left\langle \prod_{\alpha=1}^{k} \delta\left(\varepsilon_a - \frac{1}{N} H[\boldsymbol{\sigma}^a]\right) \right\rangle \tag{3.13}$$

where $\langle \cdots \rangle$ indicates the expectation value over the disorder. Using the Fourier transform representation for the δ functions,

$$p_k(\boldsymbol{\varepsilon}; \hat{q}_{ab}) = \left(\frac{N}{2\pi}\right)^k \int_{\mathbb{R}^k} \mathrm{d}^k\mu \, \mathrm{e}^{\mathrm{i}N\boldsymbol{\varepsilon}\cdot\boldsymbol{\mu}} \prod_{(i_1\dots i_p)} \left\langle \mathrm{e}^{\mathrm{i}J_{i_1\dots i_p} \sum_a \mu_a \sigma_{i_1}^a \cdots \sigma_{i_p}^a} \right\rangle \tag{3.14}$$

$$= \left(\frac{N}{2\pi}\right)^k \int_{\mathbb{R}^k} \mathrm{d}^k\mu \, \mathrm{e}^{\mathrm{i}N\boldsymbol{\varepsilon}\cdot\boldsymbol{\mu}} \, \mathrm{e}^{-\frac{N}{4}\sum_{a,b}\mu_a\mu_b \frac{p!}{N^p} \sum_{(i_1\dots i_p)} \sigma_{i_1}^a \sigma_{i_1}^b \cdots \sigma_{i_p}^a \sigma_{i_p}^b} \tag{3.15}$$

$$= \left(\frac{N}{2\pi}\right)^k \int_{\mathbb{R}^k} \mathrm{d}^k\mu \, \mathrm{e}^{\mathrm{i}N\boldsymbol{\varepsilon}\cdot\boldsymbol{\mu}} \, \mathrm{e}^{-\frac{N}{4}\boldsymbol{\mu}^T M \boldsymbol{\mu}} = A_k \, \mathrm{e}^{-N\boldsymbol{\varepsilon}^T M^{-1} \boldsymbol{\varepsilon}} \tag{3.16}$$

where the covariance matrix M is expressed in terms of the overlaps between configurations

$$M_{ab} = \left(\frac{1}{N}\sum_i \sigma_i^a \sigma_i^b\right)^p = \hat{q}_{ab}^p \,, \tag{3.17}$$

or equivalently in terms of the normalised Hamming distance x_{ab}, *i.e.* the fraction of spins that need to be flipped to go from one configuration to the other, noting that $q = 1 - 2x$.

The PDF (3.16) is a k-variate Gaussian and depends only on the $k(k-1)/2$ overlaps $\hat{q}_{ab}$ between the configurations; this justifies the notation $p_k(\boldsymbol{\varepsilon}; \hat{q}_{ab})$. For $k = 1$ we recover the p-independent density of states (3.2), and for $k = 2$ the two-level correlation function (3.3). Note that, unless the two configurations are identical, $q_{ab} < 1$. For any k distinct configurations, at large p the off-diagonal covariance matrix elements q_{ab}^p vanish exponentially, and $M_{ab} \to \delta_{ab}$. The energy levels become i.i.d. Gaussian random variables, and the REM is recovered as a limit.

3.1.3 Replica symmetric entropy

To perform a thermodynamic analysis in the microcanonical ensemble, we want to count the number of configurations that have energy density ε in the p-spin model.

This can be expressed as the random variable

$$\Omega(\varepsilon) = \sum_{\{\sigma_i\}} \delta\left(\varepsilon - \frac{1}{N} H[\boldsymbol{\sigma}]\right) \ . \tag{3.18}$$

Its average gives the density of states $\rho(\varepsilon) = 2^N p_1(\varepsilon)$ and the *annealed* entropy

$$s_{\text{ann}}(\varepsilon) = \lim_{N\to\infty} \frac{1}{N} \ln \langle \Omega(\varepsilon) \rangle = \ln 2 - \varepsilon^2 \ . \tag{3.19}$$

Note that this does not depend on p, and is the same as that of the REM (3.5). To compute the *quenched* entropy, we take the expectation value of the logarithm using the replica method,

$$s(\varepsilon) = \lim_{N\to\infty} \frac{1}{N} \langle \log \Omega(\varepsilon) \rangle = \lim_{N\to\infty} \lim_{n\to 0} \frac{1}{N} \frac{\langle \Omega(\varepsilon)^n \rangle - 1}{n} \ , \tag{3.20}$$

$$\langle \Omega(\varepsilon)^n \rangle = \sum_{\{\sigma_i^a\}} \left\langle \prod_{a=1}^{n} \delta\left(\varepsilon - \frac{1}{N} H[\boldsymbol{\sigma}^a]\right) \right\rangle = \sum_{\{\sigma_i^a\}} A_n \, \mathrm{e}^{-N\varepsilon^2 \sum_{ab} \left(M^{-1}\right)_{ab}} \ , \tag{3.21}$$

where $M_{ab} = \left(\frac{1}{N} \sum_i \sigma_i^a \sigma_i^b\right)^p$. To compute the sum we insert for each $a < b$ the integrals

$$1 = \int \mathrm{d}Q_{ab} \delta\left(Q_{ab} - \frac{1}{N} \sum_i \sigma_i^a \sigma_i^b\right) = \int \mathrm{d}Q_{ab} \frac{\mathrm{d}\lambda_{ab}}{2\pi \mathrm{i}/N} \, \mathrm{e}^{-NQ_{ab}\lambda_{ab} + \lambda_{ab} \sum_i \sigma_i^a \sigma_i^b} \ . \tag{3.22}$$

We obtain

$$\langle \Omega(\varepsilon)^n \rangle = \int \mathrm{d}\mathbf{Q} \mathrm{d}\boldsymbol{\lambda} \, \mathrm{e}^{-NnG[\mathbf{Q},\boldsymbol{\lambda}]} \tag{3.23}$$

$$nG[\mathbf{Q}, \boldsymbol{\lambda}] = \varepsilon^2 \sum_{ab} \left(M^{-1}\right)_{ab} + \sum_{a<b} \lambda_{ab} Q_{ab} - \ln \sum_{\{\sigma^a\}} \mathrm{e}^{\frac{1}{2} \sum_{(a,b)} \lambda_{ab} \sigma^a \sigma^b} \ . \tag{3.24}$$

We can now compute the entropy at energy density ε using a replica symmetric ansatz $Q_{ab} = \delta_{ab} + (1 - \delta_{ab})q$, $\lambda_{ab} = \lambda$. The first term in (3.24), computed in appendix 3.A, is given by (3.67) with $c = 1 + (n-1)q^p$. Replicas in the last term can be decoupled by a Hubbard–Stratonovich transformation, introducing an integral with Gaussian measure $Dx = \mathrm{e}^{-x^2/2} \, \mathrm{d}x/\sqrt{2\pi}$.

The integral (3.23) can then be computed using a saddle-point approximation, con-

trolled by the minimum of

$$G(q,\lambda) = \frac{\varepsilon^2}{1-(1-n)q^p} - \frac{1-n}{2}\lambda q - \int Dx \ln\left(2\cosh\sqrt{\lambda}x\right) + \frac{\lambda}{2} \tag{3.25}$$

The saddle point equations are

$$\lambda^* = \frac{2\varepsilon^2}{(1-q^{*p})^2} p q^{*p-1} \qquad q^* = \int Dx \tanh(x\sqrt{\lambda^*})^2 \ . \tag{3.26}$$

The quenched, replica symmetric entropy is

$$s_{\mathrm{RS}}(\varepsilon) = -\frac{1-pq^{p-1}+(p-1)q^p}{(1-q^p)^2}\varepsilon^2 + \int Dx \ln 2\cosh\left(x\frac{\sqrt{2p}}{1-q^p}q^{\frac{p-1}{2}}\varepsilon\right) \tag{3.27}$$

However, the fixed point equation for q^*

$$q = \int Dx \tanh^2\left(x\frac{\sqrt{2p}}{1-q^p}q^{\frac{p-1}{2}}\varepsilon\right) \tag{3.28}$$

has no non-trivial solution. The entropy is dominated by the $q = 0$ contribution, which gives the same result as the annealed entropy (3.19).

3.2 Overlap-resolved entropy

3.2.1 Annealed and quenched entropies

Given a reference configuration $\boldsymbol{\sigma}^0$, with energy density ε_0, we want to count how many configurations of energy ε there are at fixed Hamming distance Nx, or overlap $q_0 = 1-2x$. We are mostly interested in resonances, $\varepsilon = \varepsilon_0$, but consider for the moment the quantity

$$\Omega(\varepsilon_0,\varepsilon;q_0) = \sum_{\{\sigma_i\}} \delta\left(\varepsilon - \frac{1}{N}H[\boldsymbol{\sigma}]\right)\delta\left(q_0 - \frac{1}{N}\sum_i \sigma_i^0\sigma_i\right) \tag{3.29}$$

Since we are fixing the energy of the configuration $\boldsymbol{\sigma}^0$, expectation values $\langle\cdot\rangle_c$ are to be taken with the conditional probability density

$$p\left(\mathbb{J}|\varepsilon_0\right) = \frac{p(\mathbb{J})}{p_1(\varepsilon_0)}\delta\left(\varepsilon_0 - \frac{1}{N}H[\boldsymbol{\sigma}^0]\right) \tag{3.30}$$

where $p(\mathbb{J})$ is the Gaussian joint probability density of the couplings, used to take the usual expectation values $\langle\cdot\rangle$.

The *annealed* entropy of resonances is obtained from the expectation value of Ω

$$s_{\text{ann}}(\varepsilon_0, q_0) = \lim_{N\to\infty} \frac{1}{N} \log \langle \Omega(\varepsilon_0, \varepsilon_0; q_0) \rangle_c \ , \tag{3.31}$$

which can be computed as

$$\langle \Omega(\varepsilon_0, \varepsilon; q_0) \rangle_c = \sum_{\{\sigma_i\}} \delta\left(q_0 - \frac{1}{N}\sum_i \sigma_i^0 \sigma_i\right) \left\langle \delta\left(\varepsilon - \frac{1}{N} H[\boldsymbol{\sigma}]\right) \delta\left(\varepsilon_0 - \frac{1}{N} H[\boldsymbol{\sigma}^0]\right) \right\rangle / p_1(\varepsilon_0) \tag{3.32}$$

$$= \sum_{\{\sigma_i\}} \delta\left(q_0 - \frac{1}{N}\sum_i \sigma_i^0 \sigma_i\right) p_2(\varepsilon_0, \varepsilon; q_0)/p_1(\varepsilon_0) = \binom{N}{Nx} \frac{p_2(\varepsilon_0, \varepsilon; q_0)}{p_1(\varepsilon_0)} \ . \tag{3.33}$$

Unsurprisingly, this tells us that the average is given by the total number of configurations at distance Nx, times the probability that each of them has energy ε conditioned on fixing ε_0.

This gives the annealed entropy, computed in Ref. [41]

$$s_{\text{ann}}(\varepsilon_0; q_0 = 1 - 2x) = -x \ln x - (1-x)\ln(1-x) - \frac{1-(1-2x)^p}{1+(1-2x)^p} \varepsilon_0^2 \ . \tag{3.34}$$

Correlations between the energies of different configurations contribute to fluctuations of Ω, meaning that the average number of states could not be representative of the typical value in a sample. To account for this, we compute the *quenched* entropy, using the replica method to take the average of the logarithm,

$$s(\varepsilon_0; q_0) = \lim_{N\to\infty} \frac{1}{N} \langle \ln \Omega(\varepsilon_0, \varepsilon_0; q_0) \rangle_c = \lim_{N\to\infty} \lim_{n\to 0} \frac{1}{N} \frac{\langle \Omega^n \rangle_c - 1}{n} \ . \tag{3.35}$$

$$\langle \Omega(\varepsilon_0, \varepsilon; q_0)^n \rangle_c = \sum_{\{\sigma_i^a\}} \prod_{a=1}^n \delta\left(q_0 - \hat{q}_{0a}\right) \left\langle \prod_{a=1}^n \delta\left(\varepsilon - \frac{1}{N} H[\boldsymbol{\sigma}^a]\right) \delta\left(\varepsilon_0 - \frac{1}{N} H[\boldsymbol{\sigma}^0]\right) \right\rangle / p_1(\varepsilon_0) \tag{3.36}$$

$$= \sum_{\{\sigma_i^a\}} \left[\prod_{a=1}^n \delta\left(q_0 - \hat{q}_{0a}\right)\right] p_{n+1}(\varepsilon_0, \varepsilon \ldots \varepsilon; \hat{q}_{ab})/p_1(\varepsilon_0) \ . \tag{3.37}$$

The probability p_{n+1} is expressed in terms of the inverse of the matrix M, with $M_{ab} = \hat{q}_{ab}^p$. The replica space is $n+1$-dimensional, due to the additional reference configuration. In the following, replica indices only span the "internal" replicas $a = 1 \dots n$, while the index 0 is written explicitly for the reference configuration.

In principle the quantities we are computing depend on the reference configuration $\boldsymbol{\sigma}^0$. However since all configurations are statistically equivalent, the expectation values in (3.37) are functions of $q_0, \varepsilon_0, \varepsilon$ only and cannot depend on $\boldsymbol{\sigma}^0$. Therefore we can take explicitly the microcanonical average over the reference configuration, which simplifies the calculation. As usual, we insert the integrals (3.22) over the matrices Q_{ab}, λ_{ab} and represent the δ's in (3.37) with integrals over λ_{0a}. Note that there is no Q_{0a} integral since q_0 is fixed.

$$\begin{aligned}\langle \Omega(\varepsilon_0, \varepsilon; q_0)^n \rangle_c \propto \int [\mathrm{d}Q_{ab} \mathrm{d}\lambda_{ab} \mathrm{d}\lambda_{0a}] \sum_{\{\sigma_i^0, \sigma_i^a\}} \exp\Bigg\{ -N \Bigg[\sum_a q_0 \lambda_{0a} + \sum_{a<b} Q_{ab}\lambda_{ab} \\ - \frac{1}{N} \sum_{a,i} \lambda_{0a} \sigma_i^0 \sigma_i^a - \frac{1}{N} \sum_{a<b,i} \lambda_{ab} \sigma_i^a \sigma_i^b + \boldsymbol{\epsilon} M^{-1} \boldsymbol{\epsilon} - \varepsilon_0^2 - \ln 2 \Bigg] \Bigg\}\end{aligned} \tag{3.38}$$

where $\boldsymbol{\epsilon} = (\varepsilon_0, \varepsilon \dots \varepsilon)$. With a replica symmetric ansatz the matrix M takes the form

$$M_{\mathrm{RS}} = \left(\begin{array}{c|ccc} 1 & q_0^p & \dots & q_0^p \\ \hline q_0^p & 1 & & q^p \\ \vdots & & \ddots & \\ q_0^p & q^p & & 1 \end{array} \right) . \tag{3.39}$$

We now focus on resonances, $\varepsilon = \varepsilon_0$. The quantity $\boldsymbol{\epsilon} M_{RS}^{-1} \boldsymbol{\epsilon}$ is computed in the appendix, eq. (3.71), with $d_n = 1 + (n-1)q^p$. After analytical continuation in n, for $n \to 0$ the RS partition function takes the form

$$\langle \Omega(\varepsilon_0, \varepsilon; q_0)^n \rangle_c \propto \int \mathrm{d}q \mathrm{d}\lambda \mathrm{d}\lambda_0 \, \mathrm{e}^{-NnG(q,\lambda,\lambda_0;q_0)} \tag{3.40}$$

$$G_{\mathrm{RS}}(q, \lambda, \lambda_0; q_0) = \lambda_0 q_0 + \frac{\lambda}{2}(1-q) + \varepsilon_0^2 \frac{(1-q_0^p)^2}{1-q^p} - \ln 2 - \int Dx \ln \cosh(\lambda_0 + \sqrt{\lambda} x) + \mathcal{O}(n) \tag{3.41}$$

The stationary point equations, obtained by deriving G with respect to q, λ and λ_0

respectively, are

$$\lambda = 2p\varepsilon_0^2 q^{p-1}\left(\frac{1-q_0^p}{1-q^p}\right)^2 \tag{3.42}$$

$$q = \int Dx \tanh(\lambda_0 + \sqrt{\lambda}x)^2 \tag{3.43}$$

$$q_0 = \int Dx \tanh(\lambda_0 + \sqrt{\lambda}x) \tag{3.44}$$

In general these equations are not solvable analytically. To obtain the replica symmetric overlap-resolved entropy, one needs to solve them self-consistently at fixed q_0, ε_0, obtaining numerical values for q, λ, λ_0, and plugging them in (3.41).

3.2.2 Replica symmetry breaking

The overlap-resolved entropy considered here is the microcanonical analogue of the well studied (canonical) Franz–Parisi potential [83] (see also the brief discussion in section 3.3.3). With insight from the canonical calculation, we expect the replica symmetric ansatz to give accurate results only for some values of q_0, while depending on ε_0, in some ranges of q_0 the entropy can be dominated by a different overlap structure in replica space.

For this reason, we consider for the saddle-points of (3.38) a one-step replica symmetry breaking ansatz, in which the n replicas are grouped in n/m blocks of m replicas. The overlap between two replicas a, b then depends on whether they are part of the same block ($\hat{q}_{ab} = q_2$) or not ($\hat{q}_{ab} = q_1$), while the overlap with the reference configuration is always fixed $\hat{q}_{0a} = q_0$. Similarly, λ_{ab} can take the values λ_2, λ_1, while $\lambda_{0a} = \lambda_0$. The matrix M therefore has a hierarchical structure, *e.g.* for $n = 6, m = 3$:

$$M_{\text{1RSB}} = \left(\begin{array}{c|ccc|ccc} 1 & \multicolumn{6}{c}{q_0^p} \\ \hline & 1 & q_2^p & q_2^p & \multicolumn{3}{c}{} \\ & q_2^p & 1 & q_2^p & \multicolumn{3}{c}{q_1^p} \\ q_0^p & q_2^p & q_2^p & 1 & \multicolumn{3}{c}{} \\ \hline & \multicolumn{3}{c|}{} & 1 & q_2^p & q_2^p \\ & \multicolumn{3}{c|}{q_1^p} & q_2^p & 1 & q_2^p \\ & \multicolumn{3}{c|}{} & q_2^p & q_2^p & 1 \end{array}\right). \tag{3.45}$$

Focussing again on the same-energy overlap resolved entropy, $\varepsilon = \varepsilon_0$, from eq. (3.71),

plugging in the (constant) sum of the rows of the $n \times n$ block

$$d_n = 1 + (m-1)q_2^p + (n-m)q_1^p, \tag{3.46}$$

$$\boldsymbol{\epsilon} M_{\text{1RSB}}^{-1} \boldsymbol{\epsilon} = \frac{1 + (m-1)q_2^p + (n-m)q_1^p - 2nq_0^p + n}{1 + (m-1)q_2^p + (n-m)q_1^p - nq_0^{2p}} \varepsilon_0^2 \ . \tag{3.47}$$

The sum over replicas in (3.38) can be performed by decomposing the index $a = (a_0, a_1)$ running over and within the blocks respectively; and using nested Hubbard-Stratonovich transformations to decouple the blocks (x-integral) and the replicas within each block (z-integral)

$$\frac{1}{2^N} \sum_{\{\sigma_i^0, \sigma_i^a\}} \mathrm{e}^{\sum_{a,i} \lambda_{0a} \sigma_i^0 \sigma_i^a + \sum_{a<b,i} \lambda_{ab} \sigma_i^a \sigma_i^b} = \tag{3.48}$$

$$= \left(\sum_{\sigma^a} \mathrm{e}^{\lambda_0 \sum_a \sigma^a + \frac{\lambda_1}{2} (\sum_a \sigma^a)^2 + \frac{1}{2}(\lambda_2 - \lambda_1) \sum_{a_0} (\sum_{a_1} \sigma^a)^2 - \frac{n}{2}\lambda_2} \right)^N \tag{3.49}$$

$$= \left(\mathrm{e}^{-\frac{n}{2}\lambda_2} \int Dx \prod_{a_0=1}^{\frac{n}{m}} \int Dz_{a_0} \sum_{\{\sigma^a\}_{a_1}} \prod_{a_1=1}^{m} \mathrm{e}^{(\lambda_0 + x\sqrt{\lambda_1} + z_{a_0}\sqrt{\lambda_2 - \lambda_1})\sigma^a} \right)^N \tag{3.50}$$

$$= \left(2^n \, \mathrm{e}^{-\frac{n}{2}\lambda_2} \int Dx \left[\int Dz \cosh(\lambda_0 + x\sqrt{\lambda_1} + z\sqrt{\lambda_2 - \lambda_1})^m \right]^{\frac{n}{m}} \right)^N . \tag{3.51}$$

The z-integral can be seen as a partition function $Z_{x,m}(\varphi)$ for a single spin in an effective field $\varphi = \lambda_0 + x\sqrt{\lambda_1} + z\sqrt{\lambda_2 - \lambda_1}$. In the following, we will need to compute averages in the corresponding measure, which we denote

$$\langle\langle \ldots \rangle\rangle_z = \frac{\int Dz \cosh(\varphi)^m \cdots}{\int Dz \cosh(\varphi)^m} \ . \tag{3.52}$$

The expressions (3.47,3.51) can be analytically continued to $n, m \in \mathbb{R}$, so we can take the $n \to 0$ limit, while m is to be determined later together with the other 1RSB parameters. Under analytic continuation, the condition $1 \leq m \leq n$ becomes $0 \leq m \leq 1$.

Finally, we obtain the 1RSB solution from the saddle point of

$$\langle \Omega(\varepsilon_0, \varepsilon; q_0)^n \rangle_c \propto \int \mathrm{d}q_1 \mathrm{d}q_2 \mathrm{d}\lambda_0 \mathrm{d}\lambda_1 \mathrm{d}\lambda_2 \, \mathrm{e}^{-NnG_{\text{1RSB}}(q_1, q_2, \lambda_0, \lambda_1, \lambda_2; q_0, \varepsilon_0)} \tag{3.53}$$

$$G_{\mathrm{1RSB}}(q_1, q_2, \lambda_0, \lambda_1, \lambda_2; q_0, \varepsilon_0) = q_0\lambda_0 - \frac{m}{2}q_1\lambda_1 + \frac{m-1}{2}q_2\lambda_2 + \varepsilon_0^2\frac{(1-q_0^p)^2}{1+(m-1)q_2^p - mq_1^p} + \frac{\lambda_2}{2} - \ln 2 - \frac{1}{m}\int Dx \ln Z_{x,m} \ . \quad (3.54)$$

Optimising over the q's (except q_0), λ's and m, we obtain the saddle point equations

$$\lambda_{1,2} = 2p\varepsilon_0^2 q_{1,2}^{p-1}\left(\frac{1-q_0^p}{1-(m-1)q_2^p - mq_1^p}\right)^2 \quad (3.55)$$

$$q_2 = \int Dx \left\langle \langle \tanh(\varphi)^2 \rangle \right\rangle_z \quad (3.56)$$

$$q_1 = \int Dx \left\langle \langle \tanh(\varphi) \rangle \right\rangle_z^2 \quad (3.57)$$

$$q_0 = \int Dx \left\langle \langle \tanh(\varphi) \rangle \right\rangle_z \quad (3.58)$$

$$0 = (p-1)\varepsilon_0^2(q_2^p - q_1^p)\left(\frac{1-q_0^p}{1-(m-1)q_2^p - mq_1^p}\right)^2 + \frac{1}{m^2}\int Dx \ln Z_{x,m} - \frac{1}{m}\int Dx \left\langle \langle \ln\cosh(\varphi) \rangle \right\rangle_z \ . \quad (3.59)$$

3.3 Clustering and dynamical transitions

3.3.1 Replica symmetric

The self-consistent solution of equations (3.42-3.44) leads to the replica symmetric result for the overlap-resolved entropy, shown for $p = 3, 6, 10$ in Fig. 3.1. While this is not the exact result for all q_0, it provides a bound for it and improves on the annealed value (3.34). It also allows for a qualitative discussion of the features of the $s(q_0)$ curve and their physical implications. To facilitate comparisons with the equilibrium analysis in the canonical ensemble, in the following we sometimes refer to the value of the corresponding temperature $T = -1/2\varepsilon_0$, rather than directly to the energy density.

The shape of the curves reflects a competition between entropy and correlation. The total number of configurations sampled is much larger at low overlap (high Hamming distance), due to the choice of spins to flip to go from one configuration to the other.

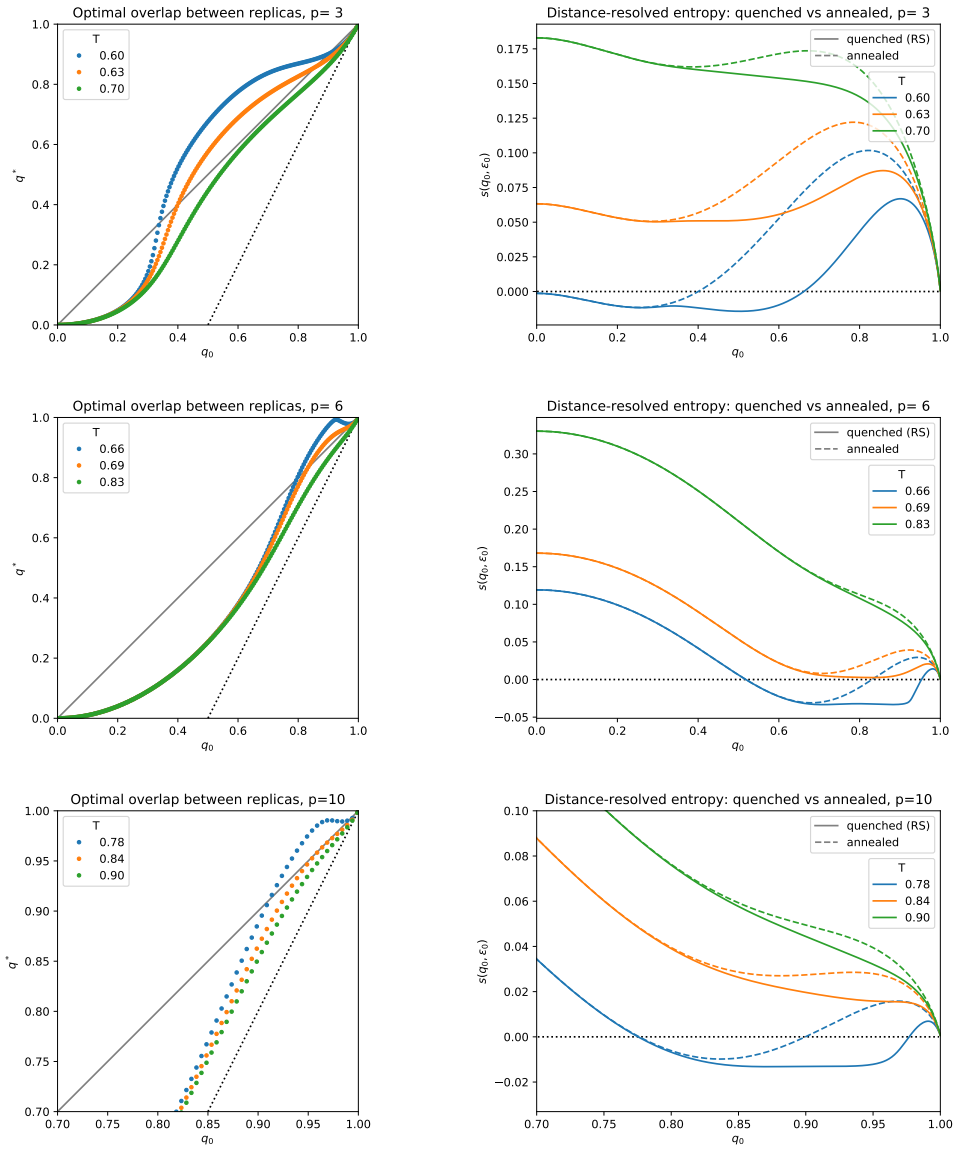

Figure 3.1: Solution of the replica symmetric equations for the overlap-resolved entropy at $T = -1/2\varepsilon_0$. Left: overlap between replicas as a function of q_0, with the diagonal $q^* = q_0$ (solid line) and minimum overlap $2q_0 - 1$ (dotted line). Right: annealed and quenched (RS) distance-resolved entropies. The last row is a detailed view for $q_0 \geq 0.7$.

On the other hand, due to the correlations in energy levels (3.16), configurations at high overlap are more likely to have the same energy.

Dynamical transition

We now discuss how the dynamical glass transition manifests itself in the microcanonical analysis. At fixed energy, we consider the curves described by the entropy as a function of the overlap, as in Fig. 3.1 (right panels). The qualitative discussion applies to both the annealed and quenched results, with the latter providing a quantitatively accurate description of the transition.

At high energy (green curves in Fig. 3.1), the entropy dominates, and the curves are monotonically decreasing, with little difference between quenched and annealed. Lowering the energy, the curves develop a stationary point and then a local maximum and minimum at high overlap (orange and blue curves). We argue that this signals the dynamical glassy transition T_d, and denote the corresponding energy density ε_d. The classical stochastic dynamics starting from the reference configuration ($q_0 = 1$) explores configurations by randomly flipping spins. While energy is not strictly speaking conserved, when considering equilibrium dynamics fluctuations of energy are suppressed in the thermodynamic limit. Therefore the evolution of the overlap with the reference configuration is ultimately determined by the slope $\mathrm{d}s/\mathrm{d}q_0$, with the system evolving towards higher overlap-resolved entropy.

If the entropy is monotonic in q_0 ($\varepsilon > \varepsilon_d$), the overlap decreases with time, ultimately flowing to $q = 0$, where most configurations lie. For $\varepsilon < \varepsilon_d$ ($T < T_d$), $q_0 = 0$ is still the global maximum; however, when the system reaches the local maximum at $q_d > 0$, the number of configurations with slightly lower overlap is still large, but exponentially smaller than that at q_d. Therefore the dynamics remains stuck in a cluster of states that have overlap q_d with the initial configuration, which we identify with the Edwards–Anderson order parameter.

This provides a microcanonical picture of the usual description of the dynamical glass transition as the decomposition of the Gibbs measure into pure states. With this insight, we expect that q_d can be identified by requiring $q^* = q_0$. This is indeed the case:[1]

$$-\frac{\mathrm{d}s_{RS}(\varepsilon_0; q_0)}{q_0} = \frac{\partial}{\partial q_0} G_{RS}(q, \lambda, \lambda_0; q_0)\bigg|_{SP} = \lambda_0 - 2p\varepsilon_0^2 q_0^{p-1}\frac{1-q_0^p}{1-q^p} \stackrel{!}{=} 0\ . \tag{3.60}$$

[1] Total and partial derivatives are equal because we are working at the saddle point, where all other partial derivatives vanish.

p	T_d (quenched)	T_d (annealed)	q_{EA}
3	0.6816	0.7355	0.643
4	0.6784	0.7176	0.815
5	0.7001	0.7304	0.881
6	0.7275	0.7520	0.915
7	0.7560	0.7764	0.935
8	0.7842	0.8017	0.948
9	0.8117	0.8270	0.957
10	0.8383	0.8518	0.963
20	1.0613	1.0669	0.986

Table 3.1: Numerical values for the dynamical transition temperature and the corresponding Edwards–Anderson parameter q_{EA}.

Requiring the entropy to be stationary gives an additional equation, to be solved together with (3.42-3.44).[2] The resulting system of equations is consistent with $q = q_0$, showing that this condition corresponds to stationary points of the entropy. We can use it to analyse the numerical solutions to the saddle-point equations, in particular the $q^*(q_0)$ curve, Fig. 3.1 (left). At fixed ε_0, if the curve crosses the diagonal, we find q_{EA} as the largest crossing point. The dynamical transition T_d corresponds to the energy ε_d at which the curve is tangent to the diagonal. This can be found with a bisection algorithm and is easier than checking directly whether $s(q_0)$ develops stationary points.

As shown in Fig. 3.1, there is in general a significant discrepancy between the quenched (RS) and annealed curves at high overlap only. This is expected: correlations between the energies of configurations with high overlap are at the origin of both the emergence of the local maximum, and the large fluctuations of Ω that make the annealed and quenched averages different. The typical number of states which the classical dynamics explores is smaller than what suggested by the annealed calculation, and their overlap q_{EA} higher. Fig.3.2 shows a comparison of the two estimates for the Edwards–Anderson order parameter at the transition, $q_d = q_{EA}(T_d)$.

The quenched curve develops a maximum at lower energy than the annealed one, implying that T_d is lower than is estimated from (3.34). The resulting estimates for some values of p are reported in Table 3.1, see also Figures 3.2 and 3.3. They agree with those found in [84] for the values of p reported there. Finally, note that the replica symmetric calculation gives the correct result for T_d, since there is no replica symmetry breaking for $q_0 > q_{EA}$, as discussed in section 3.3.2.

[2] Note that $q_0 = \lambda_0 = 0$ always solve the equations and gives the dominant contribution to the (non-overlap-resolved) entropy when optimizing over q_0, recovering equations (3.26).

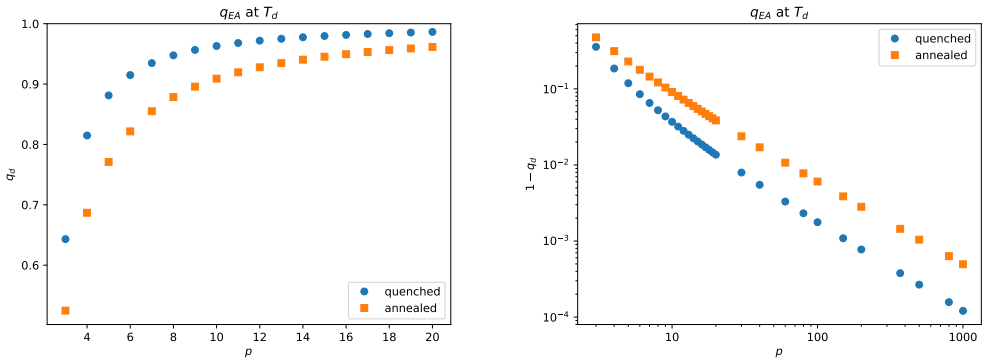

Figure 3.2: Edwards–Anderson order parameter at the dynamical transition $q_d = q_{EA}(T_d)$, annealed and quenched (exact) estimates.

Clustering transition

The description above focussed on the local maximum, representing a cluster of configurations to which the stochastic dynamics is confined (pure state). Just below ε_d there are still many configurations at all overlaps and the entropy is positive. Further lowering the energy, the value of the local minimum of the entropy decreases, eventually becoming zero at some energy ε_*. For $\varepsilon_0 < \varepsilon_*$, the overlap-resolved entropy becomes negative, indicating that there is an interval of values of the overlap for which there is typically no configuration of energy ε_0, separating a correlated, high-overlap cluster of configuration from low-overlap bulk. This is the clustering transition discussed by Baldwin *et al.* [41], where it forms the basis of their analysis of the ergodicity of the quantum dynamics, see the discussion in Section 4.6.

The annealed calculation provides an upper bound for the exact value of the entropy. In particular when it is negative for some value of q_0, the exact value is negative too. Therefore the annealed estimate $T^* = -1/2\varepsilon_*$ given in [41] is a lower bound for the actual clustering transition temperature. The examples in Fig. 3.1 show that around the minimum there is indeed a significant difference $s_{\mathrm{RS}} < s_{\mathrm{ann}}$, therefore $T^*_{\mathrm{ann}} < T^*_{\mathrm{RS}}$. The replica symmetric ansatz provides a stricter lower bound on the exact clustering temperature, which in turn must be lower than T_d (the clusters must form before they separate). It is interesting to consider the large-p scaling of the transition temperatures. It is known that the dynamical temperature scales as [84]

$$T_d \approx \sqrt{\frac{p}{4 \log p}} \,. \tag{3.61}$$

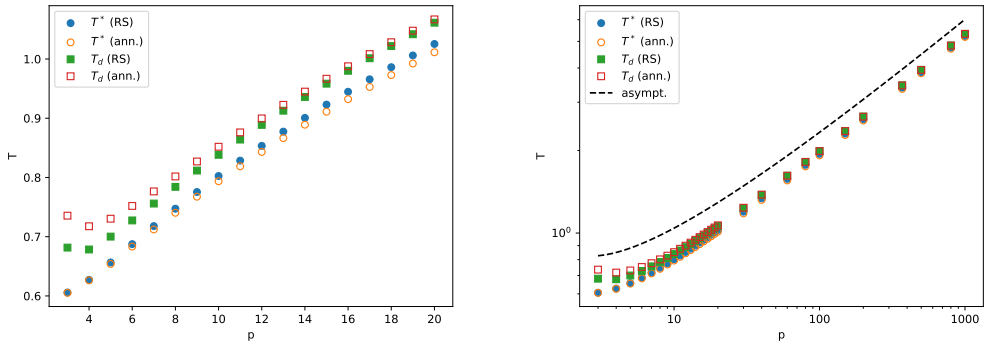

Figure 3.3: Quenched (RS) and annealed estimates for the dynamical and clustering transition temperatures as functions of p (linear and log scales). The dashed line is the asymptotic large-p scaling (3.61).

In [41], it is argued that T^* has the same asymptotic behaviour. The calculation there is at the annealed level; however, since the RS estimate and the exact result are bounded by two quantities with the same scaling, they also scale the same way. Figure 3.3 shows the annealed and RS estimates for the clustering and dynamic transition temperatures as functions of p.

The size of the high-overlap cluster, as estimated by the replica symmetric ansatz is significantly smaller than the annealed result, consistent with the difference in q_d discussed previously. We confirm that the clusters are well separated from the bulk configurations, and become arbitrarily small as p increases.

We notice, particularly at low p and ε_0, the appearance of an additional local maximum between 0 and q_{EA}, see Figure 3.1 (upper right). This is an artefact of the replica symmetric ansatz, which we do not expect to give the exact result for intermediate values of q_0. Therefore, the RSB analysis is necessary to compute exact values of T^*.

$q^* \to 1$

At low enough energy, the $q(q_0)$ curve obtained from the RS calculation develops a maximum. Further lowering the energy, the value of this peak increases, until it approaches 1. Below this energy, there are values of q_0 for which the RS equations (3.42-3.44) have no solution. To analyse this, consider the equations for $q \to 1$, *i.e.* a $\eta \to 0$ scaling with

$$q = 1 - \eta, \quad \lambda \approx \eta^{-2}, \quad \lambda_0 \approx \eta^{-1} \ . \tag{3.62}$$

After some manipulations and asymptotic analysis of the integrals, consistence with the equations requires

$$\mathrm{e}^{-[\mathrm{erf}^{-1}(q_0)]^2} = 3\sqrt{\frac{\pi}{p}}|\varepsilon_0|(1-q_0^p) \ . \tag{3.63}$$

At high energy, (3.63) has no solution, and the RS saddle point equations give a continuous curve $q^*(q_0)$. At some energy $\varepsilon_B < \varepsilon_*$, two solutions $q_\pm$ appear, and the RS equations have a solution only on $[0, q_-]$ and $[q_+, 1]$. For $q_0 \to q_\pm$, the replicas collapse on a single configuration $q \to 1$. We have no physical interpretation of this, other than the fact that the replica symmetric ansatz is unphysical in this regime, and a RSB analysis is needed.

When solving the RS equations numerically, we normally "follow" the solution from high to low q_0, using $q(q_0 + \Delta)$ as starting point for the self-consistent solution at q_0. For $\varepsilon < \varepsilon_B$, it is not possible to do this at low overlap. A possible alternative is to use instead $q^* \approx q_0^2$. This is the scaling obtained by expanding self-consistently equations (3.42-3.44) at $q_0 \to 0$. Note however that this is only needed for energies well below the RS estimate for the clustering transition, which are outside our range of interest.

3.3.2 1RSB

To obtain a better estimate of the overlap-resolved entropy curve between the two maxima, and therefore of the clustering transition temperature T^*, we need to solve the 1RSB equations (3.55-3.59). The numerical solution of these equation is significantly more complicated and delicate than that of the RS equations. This is due to a variety of reasons:

- It is a system of six equations in six variables $(q_{1,2}, \lambda_{0,1,2}, m)$, compared to three equations in three variables (optimisation problem in six-dimensional space).
- Equations (3.56-3.59) involve *nested* Gaussian integrals: each evaluation of the Dx integrand involves two Dz integrals.
- The RS solution $q_2 = q_1 = q^*$ is always present, and we expect an additional 1RSB solution $q_2 > q_1$ for some values of q_0. We want to be able to find both, detecting the value of q_0 at which replica symmetry breaking happens.
- The 1RSB solution breaks down below the clustering transition (see discussion below).

The numerical solution was implemented in Python and SciPy [85]. At fixed ε_0, q_0,

we eliminate λ_1, λ_2 using (3.55), and solve the remaining four-variable system using SciPy's `optimize.fsolve`, a wrapper around the `hybrd` algorithm from the `MINPACK` FORTRAN library. To reconstruct the $s(q_0)$ curve at fixed ε_0, we start from a value of q_0 close to one, and "follow" the solution along q_0 in small steps δ, at each step using the solution at $q_0 + \delta$ as initial guess at q_0. If the solution at $q_0 + \delta$ is replica symmetric ($q_2 = q_1$), we add a little perturbation so that $q_2 > q_1$, to avoid being stuck in the RS solution when replica symmetry breaking happens. We found that the solution is very sensitive to the energy; therefore it is not possible to follow it along ε_0 at fixed q_0.

Some examples of the solutions found with this procedure, and the corresponding overlap-resolved entropies, are shown in Figures 3.4 and 3.5. As expected, in the dynamical glassy phase, there is replica symmetry breaking for a range of values of q_0 between the high-overlap cluster and the bulk. The RS solution is instead exact at and above q_{EA}, and for energies above ε_d there is no replica symmetry breaking. Therefore the RS results for the dynamical transition, T_d and q_{EA} are correct.

On the other hand, the entropy is changed significantly by replica symmetry breaking for $0 < q_0 < q_{EA}$. Here the RS curves are mostly flat, with a small additional local maximum. This artefact is replaced by a pronounced minimum in the 1RSB curves, showing that there are typically fewer configurations than estimated at the annealed and RS level. Since the minimum of $s(q_0)$ determines the clustering transition, this has the effect of shifting T^* to higher values. The different estimates are compared in Figure 3.6.

As ε_0 approaches ε_* from above, the maximum of $q_2(q_0)$ approaches one. The solution breaks down in an apparently similar way to what we described for the RS equations. However, in this case the fact that the breaking down coincides with the clustering transition clarifies its physical meaning. Since the typical number of configurations vanishes at q_0, the replicas within the same block all collapse to a single configuration.

From the numerical point of view, this means that it is not possible to follow the solution below the clustering transition. To compute T^*, we apply a bisection algorithm on the energy: at fixed energy ε_0, we follow the solution on a mesh from high to low q_0, until either *(i)* we find a local minimum of the entropy $s(q_0) > 0$ or *(ii)* the solution breaks down. In the first case, we conclude that $\varepsilon_0 > \varepsilon_*$, in the second that $\varepsilon_0 < \varepsilon_*$. This can be repeated until the desired precision on ε_* is achieved. Knowing that replica symmetry breaking happens below q_{EA}, we can use the RS solution there as a starting point of this procedure, for each ε_0. However, at high p the peak approaches one, and the 1RSB solution becomes hard to control numerically. For this

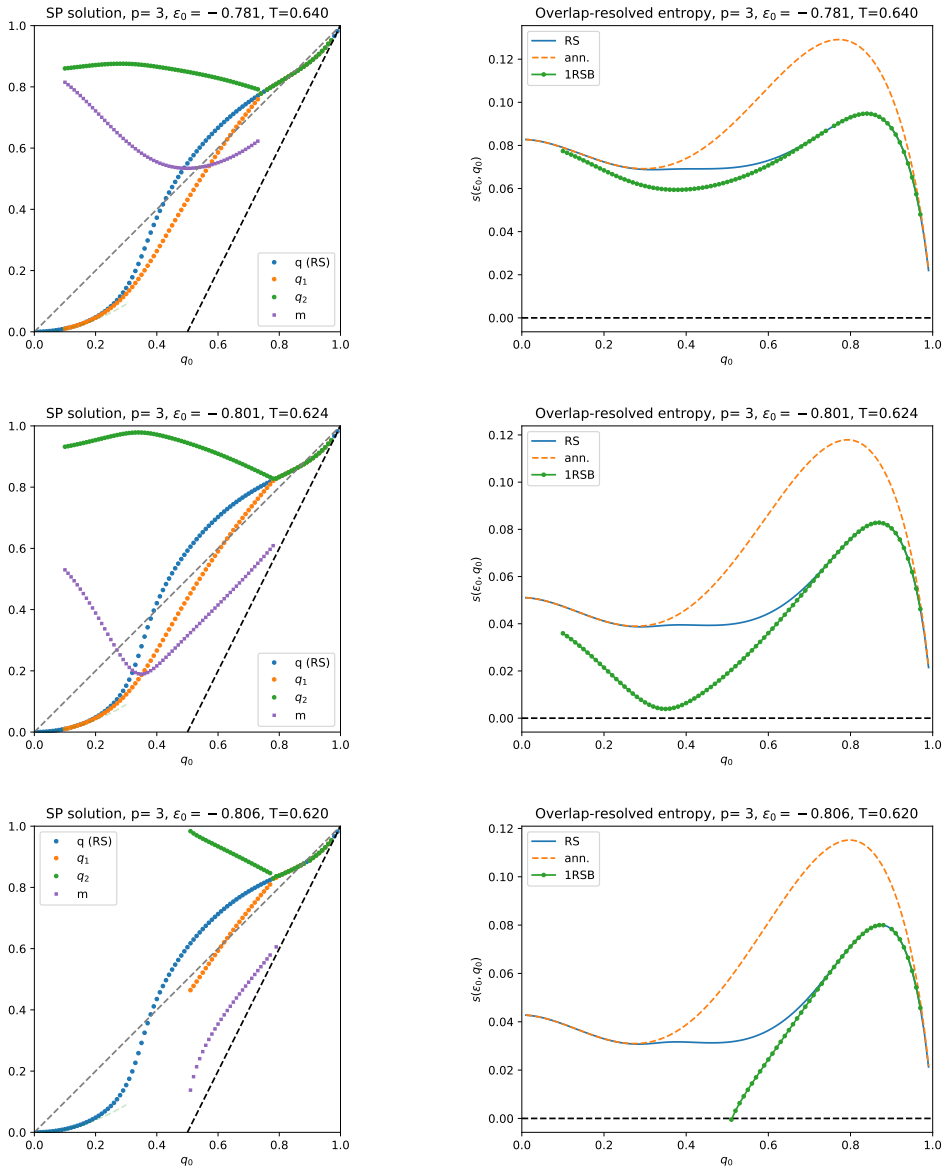

Figure 3.4: Solution of the 1RSB equations (left) and corresponding overlap-resolved entropy (right). $p = 3$, decreasing energy. On the left, the grey dashed line is the $q = q_0$ line, the black dashed line a lower bound on the q's given by the triangle inequality.

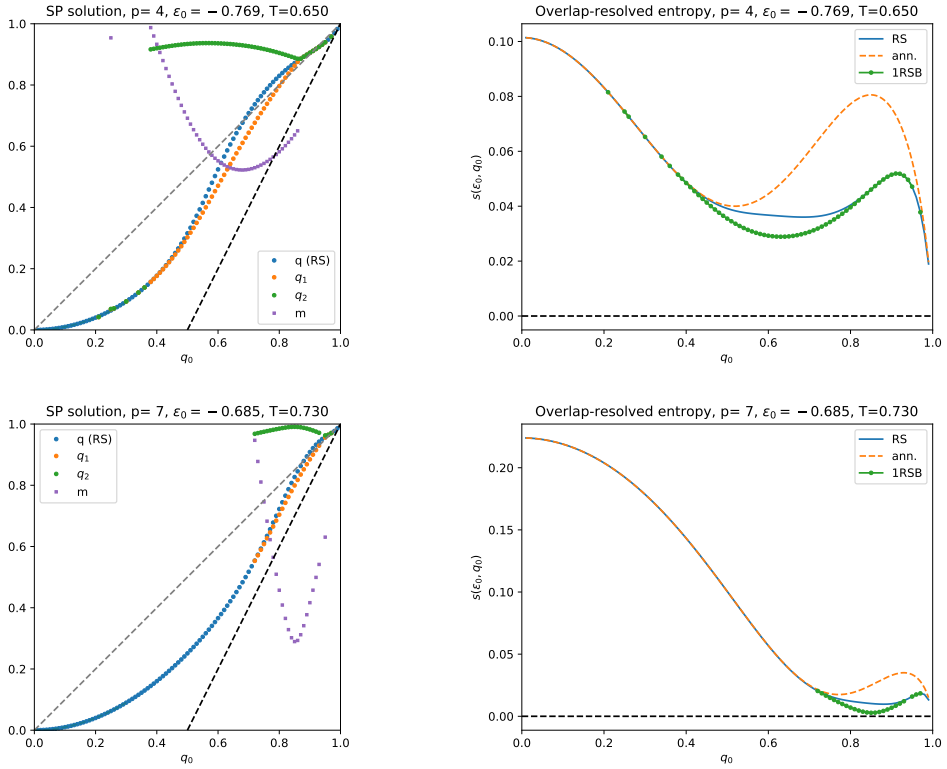

Figure 3.5: Additional examples of solutions of the 1RSB equations (left) and corresponding overlap-resolved entropy (right). On the left, the grey dashed line is the $q = q_0$ line, the black dashed line a lower bound on the q's given by the triangle inequality.

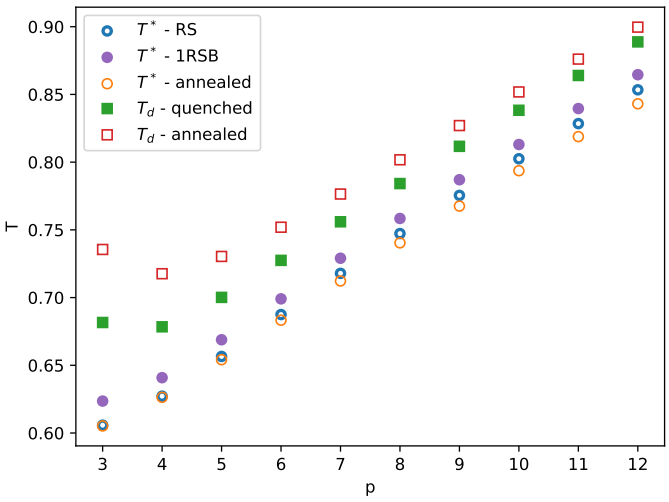

Figure 3.6: Quenched (RS, 1RSB) and annealed estimates for the dynamical and clustering transition temperatures as functions of p.

reason, we limit our analysis to $p \leq 12$, and cannot study the large-p scaling.[3] The results are shown in Figure 3.6.

Let us note finally that the annealed entropy is accurate at low enough overlap. The value of q_0 for which the annealed result is recovered is lower than at the RS level. However, we verified that for $p > 3$ and $\varepsilon_* < \varepsilon_0 < \varepsilon_d$, this value is high enough that the bulk is correctly described by the annealed calculation.

3.3.3 The Franz–Parisi potential

What we computed here is the microcanonical equivalent of the Franz–Parisi potential, a powerful tool for the analysis of spin glasses [83]. The connection between the two is the (energy-temperature) Legendre transform, in the same way that in standard statistical mechanics one goes from the (microcanonical) entropy to the (canonical) free energy. In the canonical language, the dynamical transition temperature is that below which the Franz–Parisi potential develops an additional local minimum at $q > 0$. Computing the Franz–Parisi potential from the overlap-resolved entropy would be a good consistency check; however, we expect it to be numerically unwieldy. Therefore here we only sketch the connection between the two.

[3] Recall however that T^* is bound between its annealed estimate and T_d, which determines its scaling, see Section 3.3.1 and Figure 3.3 (right).

In principle we could obtain the full potential by Legendre transform. The Franz–Parisi potential is obtained by fixing a configuration $\mathbf{s}$, computing the free energy at fixed overlap q and inverse temperature β, and then averaging over $\mathbf{s}$ drawn from the equilibrium distribution at inverse temperature β'.

$$-\beta v(\beta', \beta; q) = \left\langle \frac{1}{Z'} \sum_{\mathbf{s}} \mathrm{e}^{-\beta' H[\mathbf{s}]} \log \sum_{\boldsymbol{\sigma}} \mathrm{e}^{-\beta H[\boldsymbol{\sigma}] \delta\left(q - \frac{1}{N}\sum_i \sigma_i s_i\right)} \right\rangle \tag{3.64}$$

$$\approx \left\langle \frac{1}{Z'} \sum_{\varepsilon'} \mathrm{e}^{-\beta' \varepsilon'} \log \left(\sum_{\varepsilon} \mathrm{e}^{-\beta \varepsilon}\, \Omega(\varepsilon', \varepsilon; q) \right) \right\rangle \tag{3.65}$$

Even for $\beta = \beta'$, this involves the Legendre transform of the *two-energies* overlap-resolved microcanonical entropy. In principle this quantity can be computed with a slight modification of the derivation above. For both the RS and 1RSB calculation, it is sufficient to replace

$$\varepsilon_0^2 (1 - q_0^p)^2 \to (\varepsilon' - \varepsilon_0 q_0^p)^2 \tag{3.66}$$

in all the equations (3.41-3.42) (RS) or (3.54-3.59) (1RSB), see eq. (3.73) in the Appendix. However, in light of the difficulties described in the previous section, we expect solving the numerical solution of the equations with an extra parameter to be far from a trivial task.

3.4 Conclusion

In this chapter we presented a microcanonical analysis of the Ising p-spin model. Focussing on the overlap-resolved entropy, we refined the results of [41], giving a more precise picture of how configurations of the same energy are organised by performing a quenched computation at the replica symmetric and 1RSB levels. We confirmed the presence of a clustering transition, giving more precise estimates for the p-dependent energy at which it happens, and the size of the high-overlap cluster.

Our analysis provides a new way to determine the dynamical transition temperature for the stochastic dynamics, and the Edwards–Anderson parameter q_{EA}. We clarified the relationship between the dynamical and clustering transition and showed that, although they have the same large-p scaling, they happen at different energies/temperature and correspond to distinct phenomena.

In the $p \to \infty$ model, the REM is recovered. The cluster size shrinks to zero, and each cluster is reduced to a single configuration. This reflects the fact that energies are uncorrelated. Correspondingly, $T_d \to \infty$ and the system is dynamically frozen (glassy)

at any temperature.

In this chapter we presented a self-contained analysis of a classical model. In the context of disordered mean-field quantum systems, this is interesting because classical configurations can be taken as a basis of the Fock space, representing localised eigenstates (the vertices of the hypercube of Fig. 1.2). The motivation and relevance of this analysis for issues of quantum ergodicity are discussed in Chapter 4.

Appendix

3.A The covariance matrix

We provide some detail here of calculations involving the specific form that the covariance matrix (3.17) takes in replica calculations. Given k configurations, the covariance matrix is the p-th Hadamard (element-wise) power of the $k \times k$ matrix of overlaps Q.

When computing the entropy of states at energy density ε, the expression (3.21) involves the sum of the elements of M^{-1}. This can be computed in the following way, provided that the rows of Q have constant sum $\tilde{c}$, which is the case for Parisi ansatz matrices at any level of replica symmetry breaking. In this case, the rows of $M = Q^{\circ p}$ also have constant sum c. Then $\mathbf{e} = (1 \dots 1)$ is an eigenvector of M with eigenvalue c, and therefore of its inverse with eigenvalue $1/c$. This implies that the sum

$$\sum_{ab} (M^{-1})_{ab} = \mathbf{e}^T M^{-1} \mathbf{e} = \frac{k}{c} \ . \tag{3.67}$$

Calculations for the overlap-resolved entropy involve a slightly more complicated block form for M (with $k = n + 1$),

$$M = \left(\begin{array}{c|ccc} 1 & q_0^p & \dots & q_0^p \\ \hline q_0^p & & & \\ \vdots & & Q_n^{\circ p} & \\ q_0^p & & & \end{array} \right) \ . \tag{3.68}$$

where the $n \times 1$, $1 \times n$ blocks are constant, and Q_n is an $n \times n$ Parisi matrix. The expression and the number of parameters of $Q_n^{\circ p}$ depend on the level of replica symmetry breaking considered; however its rows have constant sum, which we denote d_n.

Note that the vectors $v_1 = (1, 0 \dots 0)$, $v_2 = (0, 1 \dots 1)/\sqrt{n}$ form an invariant subspace under M

$$\begin{aligned} M v_1 &= v_1 + \sqrt{n} q_0^p v_2 \\ M v_2 &= \sqrt{n} q_0^p v_1 + d_n v_2 \end{aligned} \tag{3.69}$$

from which we can read the elements of the reduced matrix $\tilde{M}$.

The sum of the elements of M^{-1} can be obtained again as the product $\mathbf{e}^T M^{-1}\mathbf{e}$, with $\mathbf{e} = (1 \dots 1) = v_1 + \sqrt{n}v_2$. It is then enough to invert the 2×2 matrix $\tilde{M}$.

$$\tilde{M} = \begin{pmatrix} 1 & \sqrt{n}q_0^p \\ \sqrt{n}q_0^p & d_n \end{pmatrix} \longrightarrow \tilde{M}^{-1} = \frac{1}{d_n - nq_0^{2p}} \begin{pmatrix} d_n & -\sqrt{n}q_0^p \\ -\sqrt{n}q_0^p & 1 \end{pmatrix} \tag{3.70}$$

$$\mathbf{e}^T M^{-1}\mathbf{e} = (\tilde{M}^{-1})_{11} + 2\sqrt{n}(\tilde{M}^{-1})_{12} + n(\tilde{M}^{-1})_{12} = \frac{d_n - 2nq_0^p + n}{d_n - nq_0^{2p}}. \tag{3.71}$$

The expression (3.71) can be analytically continued to real n, to take the $n \to 0$ limit needed for replica calculations,

$$\mathbf{e}^T M^{-1}\mathbf{e} = 1 + n\frac{(1 - q_0^p)^2}{d_0} + \mathcal{O}(n^2) \ . \tag{3.72}$$

Finally, to obtain the Franz–Parisi potential from the microcanonical calculations, one need the Legendre transform of the two-energy, overlap-resolved entropy. In this case M still has the form (3.68), but the quantity of interest is, with $\mathbf{w} = (\varepsilon_0, \varepsilon \dots \varepsilon)$,

$$\mathbf{w}^T M^{-1}\mathbf{w} = \frac{\varepsilon_0^2 d_n - 2nq_0^p\varepsilon_0\varepsilon + n\varepsilon^2}{d_n - nq_0^{2p}} = \varepsilon_0^2 + n\frac{(\varepsilon - \varepsilon_0 q_0^p)^2}{d_0} + \mathcal{O}(n^2) \ . \tag{3.73}$$

4 Phase diagrams of mean-field quantum spin glasses

Despite the intrinsically quantum nature of spin degrees of freedom, the theory of spin glasses has been largely developed in terms of classical models. For a long time this has provided an adequate description of materials under experimentally relevant conditions, while describing a rich phenomenology and posing formidable theoretical challenges.

Nevertheless, attempts at including quantum effects were made, and experimental progress in the early nineties made the quantum regime of spin glass materials accessible, renewing the interest in the subject [86–93]. Their equilibrium phase diagram has been investigated, leading to the generic insight that quantum fluctuations can destroy the glass phase. From the dynamical point of view, quantum effects provide an alternative way to navigate the rugged energy landscape. For this reason, quantum spin glasses have also been considered in interdisciplinary applications, such as in the search for protocols to solve satisfiability problems [94–96].

More recently, mean-field quantum spin glass models have been reconsidered in the context of MBL, with studies focussing on properties of the eigenstates and on isolated, unitary dynamics [39–43].

In this chapter we consider mean-field quantum spin glasses obtained by adding a transverse field to the p-spin model, and the quantum random energy model (QREM) emerging in the $p \to \infty$ limit. Their equilibrium phase diagram has previously been studied mostly within the static approximation, and numerical techniques based on discretisation of imaginary time. Here we derive a numerically exact, continuous-time method and apply it to the study of the high temperature phases of the p-spin model. After that, we consider the dynamical phase diagram of the QREM, and revisit the clustering picture of [41] for the p-spin model in light of the results of Chapter 3.

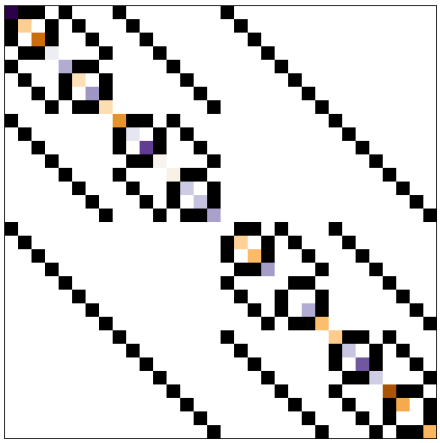

Figure 4.1: Representation of the QREM Hamiltonian as a $2^N \times 2^N$ matrix in the computational basis (N=5), showing the hierarchical structure of the couplings (black) and the random configuration energy (diagonal). The p-spin Hamiltonian has the same structure, with correlated diagonal entries.

4.1 p-spin and random energy models in a transverse field

The Hamiltonian of the quantum p-spin model in a transverse field Γ is given by

$$H = -\sum_{i_1 \dots i_p} J_{i_1 \dots i_p} \sigma^z_{i_1} \cdots \sigma^z_{i_p} - \Gamma \sum_{i=1}^{N} \sigma^x_i \ . \tag{4.1}$$

Where the σ's are Pauli matrices at each site. In the following we work mostly in the computational basis, in which states are labelled by classical configurations of spins, the eigenvalues of σ^z at each site. At $\Gamma = 0$, H is diagonal in this basis, and the model reduces to the classical one (3.1). The energies are then Gaussian random variables, the statistics of which is discussed in detail in Section 3.1.2. In the $p \to \infty$ limit the energy levels become uncorrelated, and (4.1) describes the quantum random energy model (QREM).

This provides a realisation of the mapping to the hypercube, Fig. 1.2, with classical configurations labelling the vertices, and Γ providing a hopping term between configurations differing by one spin flip. Fig. 4.1 visually represents H as a $2^N \times 2^N$ matrix in this basis, highlighting the hierarchical structure of the couplings.

In the opposite limit of $\Gamma \to \infty$, H becomes diagonal in the σ^x basis, and reduces to the Hamiltonian of N independent spins a strong magnetic field. The energy levels are labelled by the total magnetisation, $M_x\Gamma$, with $M_x = 2k - N$ for $k \in [0, N]$ and degen-

eracy $\binom{N}{k}$. This Chapter is dedicated to understanding how the system interpolates between these two limits, both from the equilibrium and dynamical perspectives.

We first focus on the equilibrium phase diagram. We review the replica method for quantum spin glasses and the static approximation, which provides the correct phase diagram for the QREM.

As in the previous chapter, we generally set $J = 1$, *i.e.* we measure temperatures, energies and Γ in units of J.

4.1.1 Replica approach

To investigate the equilibrium phase diagram for the quantum p-spin model, we compute the disorder-averaged (quenched) free energy by using the replica method, combined with the Suzuki–Trotter formalism which maps the model onto classical Ising spins [89, 91, 93, 97]. This consists essentially in representing the partition function as a path integral for the imaginary time evolution operator $\mathrm{e}^{-\beta H}$ in the following way. The imaginary time evolution is discretised as the product of M steps of size β/M, and further decomposed into contributions coming from the interaction and transverse field parts of the Hamiltonian

$$Z = \operatorname{Tr} \mathrm{e}^{-\beta H} = \lim_{M\to\infty} \operatorname{Tr} Z_M \tag{4.2}$$

$$Z_M = \left(\mathrm{e}^{\frac{\beta}{M} \sum_{(i_1 \dots i_p)} J_{i_1 \dots i_p} \sigma^z_{i_1} \dots \sigma^z_{i_p}} \, \mathrm{e}^{\frac{\beta\Gamma}{M} \sum_i \sigma^x_i} \right)^M . \tag{4.3}$$

Converting the exponential of a sum to a product of exponentials, additional terms arise due to non-commutativity of the operators, as given by the Baker–Campbell–Hausdorff formula. In the "sliced" representation, they are of order $1/M^2$ and higher. Therefore, in the limit $M \to \infty$, eq. (4.3) is an exact representation for the partition function, while at finite M it provides an approximation.

We evaluate the trace by inserting for each slice $k = 1 \dots M$ a resolution of the identity in the computational z basis.

$$\mathbb{I} = \sum_{\{\sigma_i(k)\}_i} |\{\sigma_i(k)\}\rangle \langle\{\sigma_i(k)\}| \tag{4.4}$$

The σ^z term is diagonal in this basis, while the σ^x one has matrix elements

$$\langle\sigma| \, \mathrm{e}^{\frac{\beta\Gamma}{M}\sigma^x} \, |\sigma'\rangle = \mathrm{e}^{c + B\sigma\sigma'}, \quad B = \frac{1}{2} \log \coth \frac{\beta\Gamma}{M}, \quad c = \frac{1}{2} \log \frac{\sinh(2\beta\Gamma/M)}{2} \tag{4.5}$$

This converts the replicated partition function to a sum over classical configurations of NMn spins, with three indices for sites, Trotter slices, and replicas,

$$Z_M^n = \sum_{\{\sigma_i^a(k)\}} \exp\left[\frac{\beta}{M}\sum_{k=1}^{M}\sum_{a=1}^{n}\sum_{(i_1\ldots i_p)} J_{i_1\ldots i_p}\sigma_{i_1}^a(k)\cdots\sigma_{i_p}^a(k) + \right.$$
$$\left. + B\sum_{k,a,j}\sigma_j^a(k)\sigma_j^a(k+1) + MNnc\right] \tag{4.6}$$

After some manipulations, the disorder-averaged replicated partition function takes the form

$$\overline{Z_M^n} = \sum_{\{\sigma_i^a(k)\}} \exp\left[\frac{\beta^2 J^2}{4M^2}N\sum_{(a,k;b,l)}\left(\frac{1}{N}\sum_i \sigma_i^a(k)\sigma_i^b(l)\right)^p + \right.$$
$$\left. + B\sum_{a,k,i}\sigma_i^a(k)\sigma_i^a(k+1) + MNnc\right] \tag{4.7}$$

Compared to the standard treatment of classical mean-field spin glasses, there is the additional Trotter index with an all-to-all coupling, plus a nearest neighbour coupling in the Trotter direction. The action can still be linearised by inserting the integrals (3.22), the overlaps and the corresponding Lagrange multipliers having two additional indices labelling the Trotter direction

$$Q_{kl}^{ab} = \frac{1}{N}\sum_i \sigma_i^a(k)\sigma_i^b(l), \quad \frac{\beta^2}{2M^2}\lambda_{kl}^{ab}. \tag{4.8}$$

We work at leading order in N and M. The factor in front of the Lagrange multiplier is introduced so that the λ's are of order one, and the sums converge to imaginary time integrals for $M \to \infty$. Some care must be taken with the terms involving B and c, which are singular if taken separately, but their combination gives a consistent continuous time limit, as discussed in the following. We obtain the representation

$$\overline{Z_M^n} = \int [\mathrm{d}Q_{kl}^{ab}\mathrm{d}\lambda_{kl}^{ab}]\,\mathrm{e}^{-NG[Q_{kl}^{ab},\lambda_{kl}^{ab}]} \tag{4.9}$$

$$G[Q_{kl}^{ab},\lambda_{kl}^{ab}] = \frac{\beta^2}{M^2}\sum_{(a,k;b,l)}\left[-\frac{J^2}{4}(Q_{kl}^{ab})^p + \frac{1}{2}Q_{kl}^{ab}\lambda_{kl}^{ab}\right] - \ln Z_{\mathrm{eff}} \tag{4.10}$$

$$H = \frac{\beta^2}{2M^2} \sum_{(a,k;b,l)} \lambda_{kl}^{ab} \sigma^a(k)\sigma^b(l) + B \sum_{a,k} \sigma^a(k)\sigma^a(k+1) + Mnc. \tag{4.11}$$

The problem is reduced to a single-site spin, with replica and Trotter indices, defined by the effective Hamiltonian H and the corresponding partition function $Z_{\text{eff}} = \operatorname{Tr} \mathrm{e}^H$. In the thermodynamic limit, the integrals can be evaluated with the saddle point method. The equations satisfied by the parameters at the saddle point are

$$\lambda_{kl}^{ab} = \frac{J^2}{2} p (Q_{kl}^{ab})^{p-1} \tag{4.12}$$

$$Q_{kl}^{ab} = \langle \sigma^a(k)\sigma^b(l) \rangle_H \ . \tag{4.13}$$

The latter is expressed in terms of the spin-spin correlation functions generated by H. The Q's are a dynamical (imaginary-time dependent) version of the spin glass order parameter.

4.1.2 The static approximation

Equations (4.12,4.13) have the familiar form obtained in the replica analysis of classical spin glasses, with the additional complication of the time dependence, which greatly increases the dimension of the parameter space over which we are optimizing by using the replica symmetric and RSB ansätze. The static approximation is an approach that greatly simplifies the treatment of these equations [89]. It consists in neglecting the time dependence of the Q's, assuming that the correlation functions (4.13) are constant. Even for $M \to \infty$, it is then necessary to optimise only over a few constants, rather than functions. The result of this gives a bound on the free energy, which has been used to investigate the equilibrium phase diagram, particularly in the large p limit.

The replica-symmetric static approximation ansatz is

$$\begin{aligned} Q_{kl}^{ab} &= Q, \quad \lambda_{kl}^{ab} = \lambda \quad \forall a \neq b,\ k, l \\ Q_{kl}^{aa} &= \chi, \quad \lambda_{kl}^{aa} = \nu \quad \forall k \neq l \ . \end{aligned} \tag{4.14}$$

We then have

$$G_{\text{RS}}^{(st)}(\chi, Q, \nu, \lambda) = -\frac{\beta^2 J^2}{4} n \left[\chi^p - (1-n)Q^p\right] + \frac{\beta^2}{2} n \left[\chi\nu - (1-n)Q\lambda\right] - \ln Z_H \tag{4.15}$$

where after standard manipulations

$$Z_H = \sum_{\{\sigma^a(k)\}} \mathrm{e}^{\lambda\left(\sum_{a,k}\sigma^a(k)\right)^2+(\nu-\lambda)\sigma_a(\sum_k\sigma^a(k))^2-\nu Mn} . \tag{4.16}$$

The quadratic terms can be linearised with $n+1$ Hubbard–Stratonovich transformations, similarly to the treatment of the classical calculation at the 1RSB level,

$$Z_H = \int Dz_1 \left(\int Dz_2 \sum_{\{\sigma(k)\}} \mathrm{e}^{\frac{b}{M}\sum_k\sigma(k)+B\sum_k\sigma(k)\sigma(k+1)+Mc} \right)^n \tag{4.17}$$

where $b = \beta(\sqrt{\lambda}z_1 + \sqrt{\nu-\lambda}z_2)$. The sum is the partition function of a classical Ising chain of M spins with coupling B and field b/M. It can be solved by the transfer matrix method, keeping both eigenvalues because of their scaling with M.

The RS ansatz describes paramagnetic phases, and $\lambda = Q = 0$ is indeed a solution of the saddle point equations. The remaining saddle point equations are

$$\nu = \frac{p}{2}\chi^{p-1} \qquad \chi = \int Dz_1 \left\langle\!\!\left\langle \frac{b^2}{\xi^2}\left(1+\frac{\tanh\xi}{\xi}\right)\right\rangle\!\!\right\rangle_2 \tag{4.18}$$

where $\xi = \sqrt{\gamma^2+b^2}$ and the $\langle\!\langle\cdot\rangle\!\rangle_2$ averages are taken with the measure $Dz_2\cosh\xi$.

The free energy is

$$f = \frac{1}{4T}(p-1)\chi^p - T\log\int Dz 2\cosh\left[\sqrt{\Gamma^2+p\chi^{p-1}z^2/2}/T\right] \tag{4.19}$$

In the large p limit, there are two solutions to the equations (4.18). One corresponds to $\chi = 1-\mathcal{O}(1/p^2)$, and has to leading order the same free energy as high-temperature phase of the classical REM

$$f_1 = -\frac{1}{4T} - T\log 2 + \mathcal{O}(1/p) . \tag{4.20}$$

The other solution is obtained for $\chi < 1$, $\nu \to 0$. To leading order $\chi = \tanh(\beta\Gamma)/(\beta\Gamma)$, and the free energy

$$f_2 = -\log 2\cosh\frac{\Gamma}{T} \tag{4.21}$$

is the same as that of a free spin in a field Γ. These solutions are the classical paramagnet (CPM) and quantum paramagnet (QPM).

Since the CPM solution has the same free energy as the REM, it also breaks down at $T_c = 1/(2\sqrt{\ln 2})$. At T_c, the system undergoes a transition to a spin glass phase, that

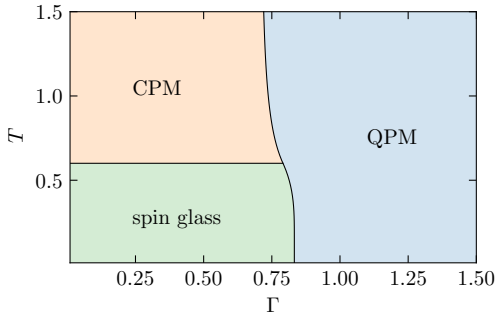

Figure 4.2: Equilibrium phase diagram of the QREM. At small but finite Γ, the free energy is the same as in the classical REM, with the glass transition at $T_c = 1/\sqrt{4 \ln 2}$. The first order transition line (4.23) separates the quantum paramagnet (QPM) from the classical paramagnet (CPM) and the glass above and below T_c respectively.

with a 1RSB static approximation ansatz [89] is found to have the same free energy as at $\Gamma = 0$,

$$f_3 = -\sqrt{\log 2} \ . \tag{4.22}$$

The QPM solution instead is physical for any temperature.

The phase diagram of the QREM is illustrated in Fig. 4.2. The QPM phase is separated by the other two by a first-order transition line $\Gamma_c(T)$, determined by $f_1 = f_2$ and $f_2 = f_3$ above and below T_c,

$$\Gamma_c(T) = \begin{cases} T \operatorname{acosh}\left(\mathrm{e}^{\sqrt{\log 2}/T}/2\right) & T < T_c \\ T \operatorname{acosh} \mathrm{e}^{1/4T^2} & T > T_c \ . \end{cases} \tag{4.23}$$

The transition persists to infinite temperature, with $\Gamma_c(\infty) = 1/\sqrt{2} > 0$. At zero temperature there is a quantum phase transition at $\Gamma_c(0) = \sqrt{\log 2}$, the point at which the ground state of the quantum paramagnet has energy density ε_c.

4.2 Beyond the static approximation

In the CPM and spin glass phases, "frozen" imaginary time order parameters are consistent with the fact that the thermodynamics is governed by the classical phases. On the QPM side, the free energy is that of a free spin, which is not consistent with the frozen dynamics. The static approximation describes the correct $p \to \infty$ limit; however, it was shown in [90] that already at the $1/p$ level the corrections

computed within the static approximation are wrong in the QPM phase. Corrections to χ and the free energy are estimated to be exponentially small in p within the static approximation, while they are $\mathcal{O}(1/p)$ when computed correctly by retaining the imaginary time dependence.

Here we go beyond the static approximation by considering a replica symmetric ansatz, while retaining the imaginary time dependence,

$$\begin{aligned} Q_{kl}^{ab} =& q_0(k,l), \quad \lambda_{kl}^{ab} = \lambda_0(k,l) \quad \forall a \neq b \\ Q_{kl}^{aa} =& \chi(k,l), \quad \lambda_{kl}^{aa} = \nu(k,l). \end{aligned} \tag{4.24}$$

The saddle point functional and the effective Hamiltonian (4.10,4.11) become

$$\begin{aligned} G_{\mathrm{RS}}[\chi,\nu,q_0,\lambda_0] = &-\frac{\beta^2 J^2}{4M^2}\left[n(n-1)\sum_{k,l} q_0(k,l)^p + n\sum_{k,l}\chi(k,l)^p\right] \\ &+ \frac{\beta^2}{2M^2}\left[n(n-1)\sum_{k,l} q_0(k,l)\lambda_0(k,l) + n\sum_{k,l}\chi(k,l)\nu(k,l)\right] - \ln Z_H \end{aligned} \tag{4.25}$$

$$\begin{aligned} H = \frac{\beta^2}{2M^2}&\left(\sum_{(a,b)}\sum_{k,l}\lambda_0(k,l)\sigma^a(k)\sigma^b(l) + \sum_a\sum_{(k,l)}\nu(k,l)\sigma^a(k)\sigma^a(l)\right) \\ &+ B\sum_{a,k}\sigma^a(k)\sigma^a(k+1) + Mnc\,. \end{aligned} \tag{4.26}$$

The Trotter direction has periodic boundary conditions and is time reversal invariant, so we can redefine the replica parameters to be function of a single variable $\tau = |k-l|$. Moreover, as argued in Ref. [87] the dominant contribution from the off-diagonal terms in replica indices comes from the zero-frequency mode, so q_0 and λ_0 are constant.

The saddle point equations are then

$$\nu(\tau) = \frac{J^2}{2} p\chi(\tau)^{p-1} \qquad \chi(\tau) = \langle\sigma^a(\tau)\sigma^a(0)\rangle_H \tag{4.27}$$

$$\lambda_0 = \frac{J^2}{2} p q_0^{p-1} \qquad q_0 = \langle\sigma^a(\tau)\sigma^b(0)\rangle_H\,. \tag{4.28}$$

The diagonal order parameter $\chi(\tau)$ describes imaginary-time dynamics within a replica, while q_0 is the spin glass order parameter, quantifying correlations between replicas.

Since the replica symmetric ansatz describes paramagnetic phases, we expect the replicas to be uncorrelated. Indeed, $q_0 = \lambda_0 = 0$ is always a solution of (4.28). With this further simplification, the effective partition function takes the form

$$Z_H = \sum_{\{\sigma^a(k)\}} \prod_a \mathrm{e}^{H_s[\boldsymbol{\sigma}^a]} = \left(\sum_{\{\sigma(k)\}} \mathrm{e}^{H_s[\boldsymbol{\sigma}]} \right)^n \equiv Z_{H_s}^n \tag{4.29}$$

$$H_s = \frac{\beta^2}{2M^2} \sum_{(k,l)} \nu(k-l)\sigma(k)\sigma(l) + B\sum_k \sigma(k)\sigma(k+1) + Mc\ . \tag{4.30}$$

Z_{H_s} is a single-spin partition function, for which we want to obtain a continuous imaginary time path integral representation.

To do so, it is convenient to represent a spin trajectory by its initial state $\sigma(0)$, the number 2ℓ of spin flips,[1] and the times $\{k_i\}_{i=1\ldots 2\ell}$ at which the flips happen. The sum in the second term of (4.30) essentially counts the number of spin flips, evaluating to $M - 4\ell$. We can now take care of the large M scaling of B and c, inserting their expressions in terms of $\beta\Gamma$,

$$\mathrm{e}^{H_s[\boldsymbol{\sigma}]} = \mathrm{e}^{\sum \nu\sigma\sigma'}\, \mathrm{e}^{B(M-4\ell)+Mc} \tag{4.31}$$

$$= \mathrm{e}^{\sum \nu\sigma\sigma'} \left(\cosh\frac{\beta\Gamma}{M}\right)^M \left(\tanh\frac{\beta\Gamma}{M}\right)^{2\ell} \xrightarrow{M\to\infty} \mathrm{e}^{\sum \nu\sigma\sigma'} \left(\frac{\beta\Gamma}{M}\right)^{2\ell}\ . \tag{4.32}$$

The sum over configurations in Z_{H_s} can be organised by summing over all the possible (ordered) values of k_i's at fixed ℓ, and then summing over ℓ,

$$Z_{H_s} = \sum_{\ell=0}^{+\infty} \sum_{k_1=1}^{M} \sum_{k_2=k_1+1}^{M} \cdots \sum_{k_{2\ell}=k_{2\ell-1}+1}^{M} \sum_{\sigma(0)=\pm 1} \left(\frac{\beta\Gamma}{M}\right)^{2\ell} \mathrm{e}^{\frac{\beta^2}{2M^2}\sum_{(k,k')} \nu(k-k') s_{\ell,\mathbf{k}}(k,k')} \tag{4.33}$$

where $s_{\ell,\mathbf{k}}(k,k')$ equals 1 if the number of spin flips (k_i's) between k and k' is even, and -1 if it is odd (see Fig. 4.3).[2]

Each term in the sum is invariant under $\sigma \to -\sigma$, therefore the sum over $\sigma(0)$ contributes an overall factor of 2. In (4.33) there is exactly a factor of β/M for each of the sums over a k_i. Therefore we can now take the continuous time $M \to \infty$, with

[1] The number of spin flips must be even due to periodicity. Pairs of spin flips correspond to "kinks" in the strongly correlated systems literature [98].

[2] This is similar to the "multi-instanton configurations" of Ref. [95].

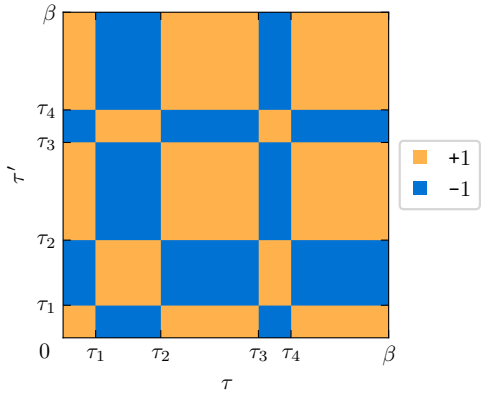

Figure 4.3: Graphical representation of $s_{\ell,\boldsymbol{\tau}}(\tau,\tau')$ for a configuration with $\ell = 2$. The value of s is $+1$ if the spin is in the same state at τ and τ' (orange), and -1 otherwise (blue).

the sums converging to integrals,

$$Z_{H_s} = 2\sum_{\ell=0}^{+\infty}\Gamma^{2\ell}\int_0^\beta \mathrm{d}\tau_1\int_{\tau_1}^\beta \mathrm{d}\tau_2\cdots\int_{\tau_{2\ell-1}}^\beta \mathrm{d}\tau_{2\ell}\exp\frac{1}{2}\int_0^\beta \mathrm{d}\tau\mathrm{d}\tau'\nu(\tau-\tau')s_{\ell,\boldsymbol{\tau}}(\tau,\tau')\ . \tag{4.34}$$

The continuous time, replica-symmetric saddle point functional is then expressed as

$$G_{\mathrm{RS}}[\chi,\nu] = \beta n\int_0^\beta \mathrm{d}\tau\left(\frac{1}{2}\chi(\tau)\nu(\tau) - \frac{J^2}{4}\chi(\tau)^p\right) - \log Z_{H_s}\ . \tag{4.35}$$

The saddle point equations have the same form (4.27), where the correlation function is intended in continuous time, computed in the effective single-spin problem described by (4.34). The construction illustrated for Z_{H_s} can be repeated to derive expressions for the correlation functions. We are interested in the two-point correlation function, which takes the form

$$\langle\sigma(s)\sigma(0)\rangle = \frac{1}{Z_{H_s}}2\sum_{\ell=0}^{+\infty}\Gamma^{2\ell}\int_0^\beta \mathrm{d}\tau_1\cdots\int_{\tau_{2\ell-1}}^\beta \mathrm{d}\tau_{2\ell}s_{\ell,\boldsymbol{\tau}}(s,0)\,\mathrm{e}^{\frac{1}{2}\int_0^\beta \mathrm{d}\tau\mathrm{d}\tau'\nu(\tau-\tau')s_{\ell,\boldsymbol{\tau}}(\tau,\tau')}\ . \tag{4.36}$$

The study of the paramagnetic phases of the quantum p-spin model is reduced to that of the imaginary time dynamics of a single-spin, similar to those emerging in the study of strongly correlated electrons within dynamical mean field theory (DMFT) [99]. Borrowing terminology from there, we refer to H_s as the *impurity* Hamiltonian. It is defined by a kernel ν, which encodes the environment of the spin, *i.e.* the effect that

the other spins of the model have on it at equilibrium. From (4.36), it is possible to extract the correlation function χ, which in turn gives back ν through the saddle point equations (4.27). In other words, the optimal values of χ and ν, describing the different equilibrium phases of the model, are the self-consistent solution of the saddle point equations. Once a solution is found, the corresponding free energy density is obtained as

$$f = \lim_{n\to 0} \frac{1}{\beta n} G_{\mathrm{RS}} = \frac{J^2}{4}(p-1)\int_0^\beta \mathrm{d}\tau \chi(\tau)^p - T \log Z_{H_s} \ . \tag{4.37}$$

4.3 Diagrammatic Monte Carlo

The equilibrium properties of the paramagnetic phases of the quantum p-spin model are encoded in the self-consistent single spin impurity problem (4.27). The computational basis path integral expression for the impurity partition function (4.34) has naturally the form of a perturbative expansion in Γ. This can be used to set up a diagrammatic Monte Carlo [98, 100] computation for imaginary time observables, in particular the correlation function, leading ultimately to a numerically exact computation of the p-spin phase diagram.

In this context a diagram is simply a spin trajectory, *i.e.* a list of imaginary times $\tau_i \subset [0, \beta]$ at which the spin flips, as described in the construction of (4.34). In terms of standard Feynman diagrams, there is only one propagator and one two-legged vertex Γ, with the constraint that the number of vertices be even due to periodicity. Due to the simplicity of the expansion compared to interacting Fermions, it is relatively easy to compute numerically the first few orders directly. The advantage of a diagMC analysis is that instead of truncating the expansion arbitrarily, the contribution of the relevant diagrams is computed according to their weights, provided that equilibrium is reached. At any order one needs to evaluate directly only the two-dimensional integral in the weight, while the 2ℓ-dimensional integrals appearing at order ℓ are computed via Monte Carlo sampling. This allows to study the system at large Γ, where terms with higher ℓ give a significant contribution.

4.3.1 Metropolis–Hastings algorithm and transition rates

Using a compact notation, in which the sum over configurations includes the sum over the number of spin flips and the time-ordered integrals over their position, the

construction of the impurity problem (4.34) can be expressed as a weighted sum

$$Z_{H_s} = \sum_{\mathcal{C}} W(\mathcal{C}) \tag{4.38}$$

and expectation values of observables are computed as the average

$$\langle O \rangle = \frac{\sum_{\mathcal{C}} O(\mathcal{C}) W(\mathcal{C})}{\sum_{\mathcal{C}} W(\mathcal{C})} = \sum_{\mathcal{C}} P(\mathcal{C}) O(\mathcal{C}) \ . \tag{4.39}$$

where the probabilities are obtained by normalising the weights, $P(\mathcal{C}) = W(\mathcal{C})/Z_{H_s}$. Diagrammatic Monte Carlo then consists in estimating observables by sampling configurations with probabilities $P(\mathcal{C})$. In the spin systems considered here, the weights are positive real numbers. Therefore the P's are a well defined probability distribution that can be sampled without worrying about the sign problems that can affect computations with Fermions [98].

The Metropolis–Hastings algorithm [98, 101] provides a way to generate samples from the distribution $P(\mathcal{C})$ by building a Markov chain for which P is the stationary state distribution. A Markov chain is a discrete-time stochastic process, completely described by the transition rates $\mathcal{S}(\mathcal{C}'|\mathcal{C})$, expressing the probability that the system is in configuration $\mathcal{C}'$ at step $n+1$ knowing that it is in $\mathcal{C}$ at step n. A sufficient condition for P to be a stationary distribution is that of detailed balance, for any two configurations $\mathcal{C}, \mathcal{C}'$

$$\mathcal{S}(\mathcal{C}'|\mathcal{C}) P(\mathcal{C}) = \mathcal{S}(\mathcal{C}|\mathcal{C}') P(\mathcal{C}') \ . \tag{4.40}$$

To guarantee that the stationary distribution is unique, it is sufficient for $\mathcal{S}$ to be ergodic, *i.e.* that any two configurations be connected in a finite number of steps with non-zero probability. It is then possible to generate configurations with distribution P by starting with any initial configuration, evolving for an appropriate equilibration time, and sampling from the resulting equilibrium distribution.

The Metropolis–Hastings algorithm provides a way to construct a class of such Markov chains by defining the transition rates in the following way. Given an initial configuration $\mathcal{C}$, the transition to configuration $\mathcal{C}'$ in the next step is proposed with probability $T(\mathcal{C}'|\mathcal{C})$. The transition is then accepted with probability $A(\mathcal{C}'|\mathcal{C})$; if it is refused, the system remains in configuration $\mathcal{C}$. The total transition rates are therefore $\mathcal{S}(\mathcal{C}'|\mathcal{C}) = T(\mathcal{C}'|\mathcal{C}) A(\mathcal{C}'|\mathcal{C})$. To ensure detailed balance, the proposal probabilities T can

be chosen arbitrarily and the acceptance ratios set to

$$A(\mathcal{C}'|\mathcal{C}) = \min\left\{1, \frac{P(\mathcal{C}')T(\mathcal{C}|\mathcal{C}')}{P(\mathcal{C})T(\mathcal{C}'|\mathcal{C})}\right\} = \min\left\{1, \frac{W(\mathcal{C}')T(\mathcal{C}|\mathcal{C}')}{W(\mathcal{C})T(\mathcal{C}'|\mathcal{C})}\right\} . \tag{4.41}$$

Note that the weights are strictly positive numbers. To ensure ergodicity, it is sufficient to ensure that the proposal probabilities connect any two configurations in a finite number of steps. Given a choice of T's, it is then possible to sample P by generating such a stochastic process, which at each step involves only computing the ratio of weights $W(\mathcal{C}')/W(\mathcal{C})$.

Here we consider the impurity problem appearing in the replica solution of the quantum p-spin model, for which the weights can be read off (4.34),

$$W(\mathcal{C}) = \Gamma^{2\ell} \exp\left[\frac{1}{2}\int_{[0,\beta]^2} \mathrm{d}\tau \mathrm{d}\tau' \nu(\tau - \tau') s_{\mathcal{C}}(\tau, \tau')\right] \tag{4.42}$$

where $s_{\mathcal{C}}$ is described in Fig. 4.3.

In our implementation of the diagMC algorithm, we consider two kind of moves: (i) adding two spin flips and (ii) removing two spin flips. Either type of move is proposed with probability $1/2$. For moves of type (i) the times at which flips are added are drawn uniformly on $[0, \beta]$. For moves of type (ii) two of the flips are chosen with equal probability and removed. The $\ell = 0$ configuration needs to be treated separately. In that case we propose a move of type (i) with probability 1.

Due to the choice of uniform distributions, the T's do not depend on the times at which flips are added or removed, but only on the order ℓ of the current configuration. Their ratios appearing in (4.41) have simple expressions in terms of ℓ and β, reported in Table 4.1. The acceptance probability at each step is then obtained by computing the ratio of weights numerically, which is the most computationally expensive part of the algorithm.

The algorithm described is based on a continuous time formulation, and configurations are stored as a list of times with essentially no discretisation. On the other hand, sampling the correlation function is necessarily done on a discrete grid of M points. When working with the self-consistency equations, the hybridisation function ν is also sampled on the same grid. Therefore we expect the cost of computing the weights to scale as $\mathcal{O}(M^2)$. Given a configuration $\mathcal{C} = \{\tau_i\}$, a sample of the correlation function at time s is plus or minus one, depending on the parity of the number of τ_i's smaller than s. This makes the cost of sampling correlation functions negligible. The overall computational cost of the algorithm scales as $\mathcal{O}(M^2)$, allowing to work with

ℓ	(i) add	(ii) remove
0	$\frac{T(\mathcal{C}_0\|\mathcal{C}_1)}{T(\mathcal{C}_1\|\mathcal{C}_0)} = \frac{\beta^2}{4}$	–
1	$\frac{T(\mathcal{C}_1\|\mathcal{C}_2)}{T(\mathcal{C}_2\|\mathcal{C}_1)} = \frac{\beta^2}{12}$	$\frac{T(\mathcal{C}_1\|\mathcal{C}_0)}{T(\mathcal{C}_0\|\mathcal{C}_1)} = \frac{4}{\beta^2}$
≥ 2	$\frac{T(\mathcal{C}_\ell\|\mathcal{C}_{\ell+1})}{T(\mathcal{C}_{\ell+1}\|\mathcal{C}_\ell)} = \frac{\beta^2}{2(\ell+1)(2\ell+1)}$	$\frac{T(\mathcal{C}_\ell\|\mathcal{C}_{\ell-1})}{T(\mathcal{C}_{\ell-1}\|\mathcal{C}_\ell)} = \frac{2\ell(2\ell-1)}{\beta^2}$

Table 4.1: Ratios of proposal probabilities for the diagMC algorithm.

large values of M.

This choice of proposals is clearly ergodic: any configuration of order ℓ is connected to the empty one by ℓ moves, therefore any two configurations of orders ℓ, ℓ' are connected by at most $\ell + \ell'$ moves. It is possible to implement additional classes of moves to improve the sampling and equilibration time of the Monte Carlo algorithm. A common choice is to add moves that connect configurations of the same order by shifting one τ_i, which might improve the sampling when adding spin flips is unlikely (low Γ). More complicated moves, involving a higher number of spin flips, are sometimes considered depending on the structure of the impurity Hilbert space [98]. In the case at hand, due to the relative simplicity of the problem, and for the ranges of parameters in which we are interested, such moves are not necessary and the algorithm can be restricted to the moves described above.

4.3.2 Non-interacting two-level system

To test the algorithm in a simplified setting, we apply it to a two level system, representing a single spin in a magnetic field and compare it with the analytical solution. Consider a single spin 1/2 with Hamiltonian

$$H = -h\sigma^z - \Gamma\sigma^x \ . \tag{4.43}$$

The magnetic field is in the xz plane and has magnitude $B = \sqrt{\Gamma^2 + h^2}$. The thermodynamics can be solved by diagonalising the 2×2 matrix. The partition function and

imaginary time spin-spin correlation function in the z direction are

$$Z = \operatorname{Tr} \mathrm{e}^{-\beta H} = 2\cosh(\beta B) \tag{4.44}$$

$$C_\beta(s) = \frac{1}{Z} \operatorname{Tr}\left(\mathrm{e}^{-(\beta-s)H}\,\sigma^z\,\mathrm{e}^{-sH}\,\sigma^z\right) = \frac{h^2}{B^2} + \frac{\Gamma^2}{B^2}\frac{\cosh[B(\beta-2s)]}{\cosh(\beta B)}\ . \tag{4.45}$$

The Suzuki–Trotter construction can be applied to this system, working in the σ^z basis, to provide an expansion in the transverse field Γ, as a sum over configurations similar to that of the impurity problem (4.34), with weights [94]

$$Z = \sum_{\mathcal{C}} W(\mathcal{C}), \qquad W(\mathcal{C}) = 2\Gamma^{2\ell}\cosh\left(h[2(\tau_1 - \tau_2 + \tau_3 \cdots - \tau_{2\ell}) + \beta]\right). \tag{4.46}$$

The diagMC algorithm with the moves described in the previous section can then be applied.

Results of the Monte Carlo sampling for $\beta = 2$, $h = 1$ and several values of Γ are shown in Figure 4.4. For each value of the parameters, a simulation was run with 10^7 steps, taking 10^6 samples of the correlation function, on a grid with $M = 50$ equally spaced points. The estimates from the Monte Carlo computation are in perfect agreement with the analytic results for the spin-spin correlation function (Fig. 4.4, left).

The diagMC algorithm in principle samples diagrams at all orders in Γ. It is interesting to check the distribution of the configurations sampled during a simulation. The resulting histograms, reported in Figure 4.4 (right), are estimators for the total weights of the order ℓ contribution, $P(\ell) = \sum_{\mathcal{C}} W(\mathcal{C})\delta(\hat{\ell}(\mathcal{C}) - \ell)/Z_{H_s}$. For all the values of the parameter considered, the histograms are peaked around an average value $\bar{\ell} \approx \Gamma$; higher orders are strongly suppressed, with no significant weight above $\approx 2\bar{\ell}$. The histograms also give a quantitative description of the accuracy of perturbation theory, confirming that the first few orders give a good approximation at low Γ, while most of the weight is at higher orders for larger Γ.

The distribution of spin flips can also be used to construct an estimator of the transverse magnetisation. It is related to the average number of spin flips through the expression

$$m = \langle \sigma^x \rangle = \frac{1}{\beta}\frac{\partial}{\partial \Gamma} \ln Z = \frac{1}{\beta}\sum_{\mathcal{C}} \frac{2\ell}{\Gamma} W(\mathcal{C}) = \frac{\langle 2\ell \rangle}{\beta\Gamma}. \tag{4.47}$$

This relation will be crucial to computing the free energy of the quantum p-spin model in the following. For the single spin system, it provides a further check of the diagMC

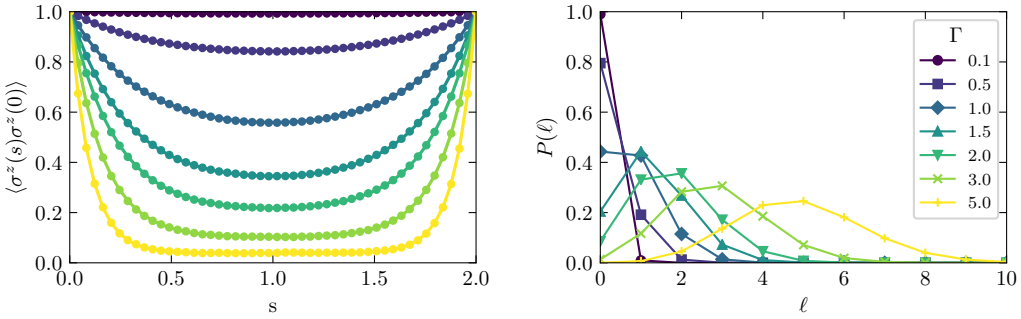

Figure 4.4: Results of diagMC for the two-level system. Left: imaginary time correlation functions, showing agreement between analytic (lines) and numeric (dots) results. Right: Distribution of the number of spin flips. For all lines, $\beta = 2$ and $h = 1$. For both panels the values of Γ follow the colour code on the right.

algorithm, by comparing the average number of flips to the analytical expression

$$\langle 2\ell \rangle = \beta \Gamma m = \frac{\beta \Gamma^2}{B^2} \tanh(\beta B) \ . \tag{4.48}$$

For the values of the parameter considered the agreement is good, with a relative error of 0.0001 or less, increasing at small Γ.

4.3.3 Iterative diagMC for the quantum p-spin model

We want to solve the self-consistent equations

$$\chi(\tau) = \langle \sigma^a(\tau)\sigma^a(0)\rangle_\nu \qquad \nu(\tau) = \frac{p}{2}\chi(\tau)^{p-1} \tag{4.49}$$

where the correlation function is defined by the ν-dependent action (4.36). To do so we perform an iterative procedure; starting with some fixed $\nu_0(\tau)$, the iteration step consists in computing χ using diagMC, and updating ν with the algebraic relation (4.49),

$$\chi_{k+1}(\tau) = \langle \sigma^a(\tau)\sigma^a(0)\rangle_{\nu_k} \qquad \nu_{k+1}(\tau) = \frac{p}{2}\chi_{k+1}(\tau)^{p-1} \tag{4.50}$$

this should be repeated until convergence within the Monte Carlo error.

For any $p > 2$, we are trying to capture the phenomenology of a first-order phase transition, as described in [93]. Therefore we expect in general two solutions, coexisting in some region of the (Γ, T) plane. At $\Gamma = 0$ (classical limit) there is one paramagnetic solution, with $\chi(\tau) = 1$. For low Γ we expect that this solution acquires corrections,

given by the expansion in Γ. At large p, the leading order corrections are $\mathcal{O}(\Gamma^2/p^2)$ and well described by the static approximation [90]. Our numerical solution provides accurate estimation of the correlation function both in this regime and at smaller p.

In the opposite limit of large Γ, the hybridisation ν becomes negligible and we expect the solution to be close to the correlation function of the free quantum paramagnet $\chi(\tau) = \cosh(\Gamma(\beta - 2\tau))/\cosh(\beta\Gamma)$. The corrections are not captured by the static approximation [90], and the full diagMC solution allows to find the exact correlation functions. We refer to the two solutions, and the corresponding equilibrium phases, as the classical paramagnet (CPM) and quantum paramagnet (QPM) respectively.

For temperatures lower than a critical value T_c, we expect to find both solution in a range of values of Γ, delimited by two spinodal curves. For each solution, the spinodal curve determines the values of Γ above (below) which it becomes unstable. In the region where both solutions are present, the one with the lowest free energy describes the equilibrium phase of the system. The condition that the two free energies be equal, $f_{\mathrm{CPM}} = f_{\mathrm{QPM}}$, defines a first order transition line, ending in the critical point at T_c. Approaching the spinodal curves, and therefore in the region close to the critical point, convergence of the iterative solution is slowed down, making the application of our method less reliable.

To track the CPM solution, we consider an interval $[\Gamma_m, \Gamma_M]$ at fixed $\beta = 1/T$, with Γ_m appropriately low, so that the we can expect the system to be in the CPM phase. We start the iteration at (β, Γ_m) with

$$\chi_0(\tau) = 1 \longrightarrow \nu_0(\tau) = \frac{p}{2} \tag{4.51}$$

and update with the rules (4.50) until convergence is determined by the method described in the following. We then repeat the iterative procedure with parameters $(\beta, \Gamma + \delta\Gamma)$ for some small step $\delta\Gamma$, using as initial condition $\nu_0 = \nu_\Gamma$ the solution obtained at (β, Γ). This is then repeated for $\Gamma + 2\delta\Gamma$ and so on, until Γ_M is reached. With this approach we can "follow" the CPM solution to higher values of Γ, minimising the risk that the iterative procedure "fall off" the CPM solution into the QPM one. It also has the advantage that at each step, the iteration starts with a correlation function close to the self-consistent solution, and is therefore expected to converge quite quickly, more so for smaller $\delta\Gamma$.

The same approach can be used to track the QPM solution, by starting with a Γ_M for which the system is in the QPM phase, and "following" the solution decreasing Γ by $\delta\Gamma$ until Γ_m is reached. For the first iteration, we use the free spin correlation

function

$$\chi_0(\tau) = \frac{\cosh[\Gamma(\beta - 2\tau)]}{\cosh(\beta\Gamma)}, \quad \nu_0(\tau) = \frac{p}{2}\chi_0(\tau)^{p-1} \ . \tag{4.52}$$

In this way, we are able to find for which values of Γ the two solutions exist, and in particular the coexistence region and spinodal curves. To monitor the solutions without looking at the full shape of χ, it is useful to consider the quantity $\Xi = \int_0^\beta \chi(\tau)^p$ and the transverse magnetisation $m = \langle\sigma^x\rangle$. Both quantities are computed from the Monte Carlo sampling, Ξ directly from the correlation function and m is related to the average order of the configurations samples as described in (4.47). In the classical limit, $\Xi \to \beta$ and $m \to 0$. At large Γ, we expect $\Xi \sim \mathcal{O}(1/\Gamma)$ and $m \to 1$. Therefore, the CPM phase is characterised by larger values of Ξ and small m, while the QPM phase by larger m and smaller Ξ. When tracking the two solutions, the spinodal lines are signalled by jumps in the values of these parameters.

Thermodynamic integration

Ultimately, we are interested in computing the free energy in each phase and find the transition line. The expression (4.37) has two contributions, the first proportional to Ξ, and the second is the impurity free energy. The latter cannot be computed directly by the Monte Carlo sampling. To overcome this, we resort to thermodynamic integration. We first need to find a quantity that can be measured in the diagMC simulations and can be written as a derivative of the free energy. With temperature and transverse field as parameters, natural choices are the energy density and magnetisation,

$$\varepsilon = \frac{1}{N}\langle H\rangle = \frac{\partial}{\partial\beta}\beta f, \qquad m = \frac{1}{N}\langle\sum_i \sigma_i^x\rangle = -\frac{\partial}{\partial\Gamma}f \ . \tag{4.53}$$

The free energy at any point in the (T, Γ) plane can be computed by integrating these quantities over the corresponding parameters. For our purposes it is more convenient to focus on the magnetisation, and integrate over Γ at fixed β,

$$f(\Gamma, \beta) = f(\Gamma_0, \beta) - \int_{\Gamma_0}^{\Gamma} m(\Gamma', \beta)\mathrm{d}\Gamma' \ . \tag{4.54}$$

This combines naturally with the procedure outlined above to track the solutions at fixed T, with $(\Gamma_m, \Gamma_M) = (\Gamma_0, \Gamma)$. For the CPM phase, we can take $\Gamma_0 = 0$, where the free energy takes the classical value (4.20), and integrate up to the desired value of Γ_M, reconstructing the free energy curve for intermediate values of Γ. Treating the QPM phase is less straightforward: the free-spin free energy (4.21) is approached

asymptotically, requiring to either start the integration from very high Γ to suppress the finite-Γ corrections, or to account for them. We overcome this by using the self-consistent approximations discussed in the following. They provide an alternative, approximate way to compute physical quantities in the impurity problem, including the free energy (see Section 4.4). The approximations provide a good description of the QPM phase far from the transition, which can be used to integrate down in Γ to below the critical line.

We note that the magnetisation in the impurity problem at the saddle point is the same as the magnetisation in the full p-spin model in the corresponding thermal state. On the other hand, the free energy (4.37) is the sum of that of the impurity, and a "bath" contribution. We stress that thermodynamic integration reconstructs the *total* free energy. The impurity problem depends on Γ both explicitly, and through the self-consistent ν. Therefore the impurity magnetisation is not the field-derivative of the impurity free energy.

Determining convergence

Using a Monte Carlo sampling for the iterative self-consistent solution, we are faced with the problem of how to determine whether the procedure has converged in presence of noise. On the one hand, the precision to which convergence is determined cannot be smaller than the Monte Carlo error. On the other hand, the fact that two consecutive iterations give compatible results does not guarantee that convergence is reached. This problem is exacerbated by the fact that convergence should in principle be checked on a large number of points, the M samples of $\chi(\tau)$, with their correlated noise. Here we devise a procedure to address this.

Instead of the full $\chi(\tau)$, we can use the scalar parameters Ξ and m to monitor convergence of the iteration. In our simulations we observed that the choice of Ξ or m does not seem to affect the results; we choose to use Ξ.

To handle the issue of noise, we adopt the following strategy. We run a minimum number r of iterations, keeping track at each step of the measured value $\hat{\Xi}_i$. After that, at the k-th iteration, we compare $\hat{\Xi}_k$ to the average and variance of the previous r values:

$$\bar{\Xi}_k = \frac{1}{r} \sum_{i=k-r}^{k-1} \hat{\Xi}_i \tag{4.55}$$

and the corresponding variance Δ_k^2. If the new value is within one standard deviation from the mean, $|\hat{\Xi}_k - \bar{\Xi}_k| < \Delta_k$, we say that the iteration has converged, otherwise

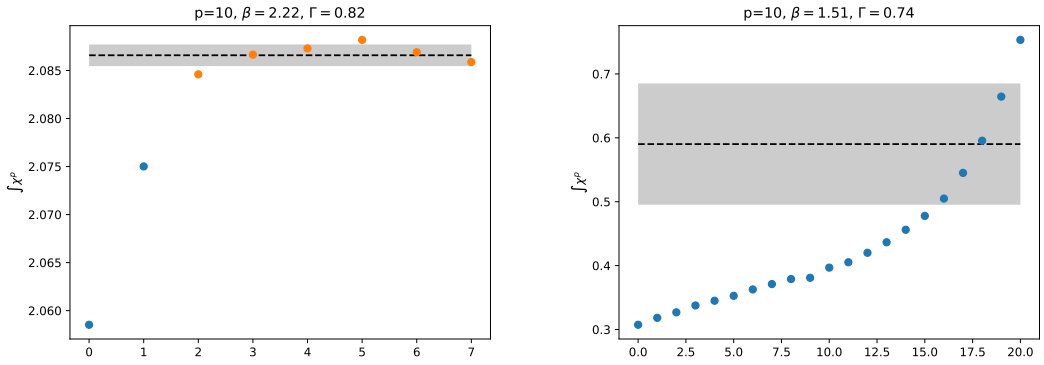

Figure 4.5: Convergence of Monte Carlo iterations. Each dot represents the quantity $\hat{\Xi}$ of one diagMC iteration, which is compared to that of the r previous steps (here $r = 5$, orange dots). The shaded area represents the window used to check for convergence. Left: example of converging iterations. Right: close to the spinodals convergence becomes slow, and the iterations are stopped after 20 steps.

one more iteration is run. This is repeated until convergence, or a maximum number of steps after which we stop the iteration, signalling the vicinity of the spinodal curve. Additionally, we impose a maximum relative error, of the order of that expected from the Monte Carlo sampling, and we include monotonicity checks on the r points.

Once convergence is reached, we use the average of the last $r+1$ iterations (including the k-th) to estimate Ξ, and the corresponding standard deviation for the error. The estimator for the magnetisation and the correlation function are constructed in the same way.

4.4 Self-consistent approximations

In this section we construct systematically a class of approximation schemes for the impurity problem based on the expansion of the two-particle irreducible (2PI) effective action in powers of the hybridisation. The approximation schemes are adapted from the analogous ones used in the DMFT analysis of strongly correlated electrons [99, 102].

4.4.1 Diagrammatic hybridisation expansion

The impurity problem for the RS replicated partition function is described by the action

$$\mathcal{S}[\boldsymbol{\sigma}] = -\frac{1}{2}\int_{[0,\beta]^2} \mathrm{d}\tau\mathrm{d}\tau' \sigma^z(\tau)\nu(\tau-\tau')\sigma^z(\tau') - \Gamma\int_0^\beta \mathrm{d}\tau\sigma^x(\tau) \tag{4.56}$$

$$Z_H = \operatorname{Tr} \mathrm{T}_\tau \, \mathrm{e}^{-\mathcal{S}[\boldsymbol{\sigma}]} \qquad \langle \mathcal{O} \rangle = \frac{1}{Z_H} \operatorname{Tr} \mathrm{T}_\tau \left(\mathrm{e}^{-S[\boldsymbol{\sigma}]} \, \mathcal{O} \right) \tag{4.57}$$

Expanding the partition function in powers of Γ at fixed ν, it is possible to recover the expression (4.34). Here we consider the opposite expansion in the hybridisation ν, around the free quantum paramagnet

$$H_0 = -\Gamma\sigma^x. \tag{4.58}$$

For later convenience, we choose to work in a basis of the impurity Hilbert space in which H_0 is diagonal. Therefore the Pauli matrices have the following representation, related to the standard one by a permutation,

$$\sigma^x = \begin{pmatrix} 1 & 0 \\ 0 & -1 \end{pmatrix} \qquad \sigma^y = \begin{pmatrix} 0 & \mathrm{i} \\ -\mathrm{i} & 0 \end{pmatrix} \qquad \sigma^z = \begin{pmatrix} 0 & 1 \\ 1 & 0 \end{pmatrix}. \tag{4.59}$$

In the free theory, imaginary-time evolution acts on operators by conjugation with the local propagator

$$R_0(\tau) = \mathrm{e}^{-\tau H_0} = \begin{pmatrix} \mathrm{e}^{\tau\Gamma} & 0 \\ 0 & \mathrm{e}^{-\tau\Gamma} \end{pmatrix} . \tag{4.60}$$

Therefore $\sigma^x(\tau) = \sigma^x$ is time-independent, and the σ^x-term in the action (4.56) is $\mathcal{S}_0 = \beta H_0$. On the other hand, $\sigma^z(\tau) = R_0(-\tau)\sigma^z R_0(\tau)$. Expanding the time-ordered exponential in powers of ν, we obtain

$$Z_H = \sum_{k=0}^\infty \int \mathrm{d}\tau_1 \mathrm{d}\tau_1' \ldots \mathrm{d}\tau_k \mathrm{d}\tau_k' \operatorname{Tr} \mathrm{T}_\tau \left[\mathrm{e}^{-\beta H_0} \prod_{i=1}^k \sigma^z(\tau_i)\sigma^z(\tau_i') \right] \operatorname{perm}_{lm} \frac{1}{2}\nu(\tau_l - \tau_m') \tag{4.61}$$

where the permanent is the sum over permutations

$$\operatorname{perm}_{lm} \nu(\tau_l - \tau_m) = \sum_{\sigma\in S_k} \prod_{i=1}^k \frac{1}{2}\nu\left(\tau_i - \tau_{\sigma(i)}'\right) . \tag{4.62}$$

Writing the time evolution explicitly, and relabelling the times to a single set $\{\tau_i\}$

with $i = 1 \dots 2k$, increasingly ordered $\tau_{j+1} > \tau_j$, the matrix structure of each term in the expansion (4.61) is given by a string

$$R_0(\beta - \tau_{2k})\sigma^z R_0(\tau_{2k} - \tau_{2k-1})\sigma^z \cdots \sigma^z R_0(\tau_1) \ . \tag{4.63}$$

Conjugation of a 2×2 matrix by σ^z amounts to swapping the diagonal elements. To make expressions more compact, we indicate this with a superscript c, *e.g.* for the free propagator $R_0^c = \sigma^z R_0 \sigma^z$.

We can then build a diagrammatic representation of the perturbative expansion, representing R_0 with a single continuous line, ν with a dashed line and σ^z as a vertex, joining two continuous and one dashed line. Note that the hybridisation is symmetric $\nu(\tau) = \nu(-\tau)$, and always enters in expressions through the combination $[\nu(\tau) + \nu(-\tau)]/2$. We can therefore consider the dashed lines to be not oriented, and assign to them the value ν without the factor $1/2$.

The diagrams contributing to Z_H at order k have the form of a single loop of $2k$ lines, corresponding to the trace of the string (4.63), with pairs of vertices connected in all the possible ways by dashed lines.

Summing all diagrams with two external R_0 legs, we obtain the dressed local propagator $R(\tau)$, in terms of which thermodynamical quantities in the full theory can be computed,

$$Z_H = \operatorname{Tr} R(\beta) \qquad \langle O \rangle = \frac{1}{Z_H} \operatorname{Tr} \left[R(\beta) O \right] \ . \tag{4.64}$$

In diagrams we represent R with a double continuous line. The vertex structure implies that all diagrams are connected and have an even number of vertices. More precisely, the diagrams contributing to R at order k have the form of a string of $2k + 1$ lines (of which two external), with $2k$ vertices connected by dashed lines. A useful way to organise the perturbative expansion is the imaginary time Dyson equation obeyed by R,

$$R(\tau) = R_0(\tau) + \int_0^\tau \mathrm{d}\tau_2 \int_0^{\tau_2} \mathrm{d}\tau_1 R(\tau - \tau_2) S(\tau_2 - \tau_1) R_0(\tau_1) \tag{4.65}$$

where the self-energy S is defined as the sum of all amputated diagrams, *i.e.* the diagrams contributing to R with the external legs removed. Eq. (4.65) is represented diagrammatically in Fig. 4.6a.

The non-crossing approximation (NCA) consists in neglecting all diagrams in which two hybridisation lines cross. The Dyson equation allows to re-sum to all orders the

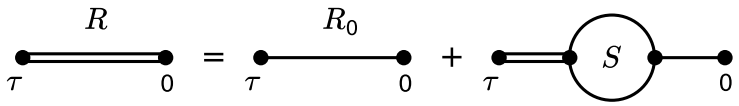

(a) Dyson equation for the local propagator $R(\tau)$, eq. (4.65).

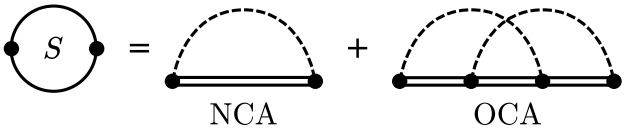

(b) Bold diagrams contributing to the self-energy S at the NCA and OCA levels, eq. (4.66,4.74).

Figure 4.6

resulting expansion for R by approximating the self-energy with

$$S_{\mathrm{NCA}}(\tau) = \sigma^z R(\tau)\sigma^z \nu(\tau) \ , \tag{4.66}$$

The diagrammatic representation (Fig. 4.6b, first diagram) shows that this self-consistently includes all diagrams without crossings. The NCA can then be implemented by solving self-consistently the system of equations (4.65,4.66), and using the resulting $R(\tau)$ to compute physical quantities.

4.4.2 The Luttinger–Ward functional

The NCA is a self-consistent conserving approximation [99], meaning that the self-energy can be obtained as the functional derivative of a functional of R, called the Luttinger–Ward functional.

The version of NCA presented here is a "first quantisation" one, in which we work directly with the impurity time evolution operator R [102]. A related, but in principle not equivalent, formulation replaces the spin with two sets of Bosonic operators (Schwinger Bosons)

$$\sigma^x = a_1^\dagger a_1 - a_2^\dagger a_2 \qquad \sigma^y = \mathrm{i}(a_1^\dagger a_2 - a_2^\dagger a_1) \qquad \sigma^z = a_1^\dagger a_2 + a_2^\dagger a_1. \tag{4.67}$$

Any thermodynamical quantity in the impurity problem can be computed as an expectation value in the Boson model, restricted to the one-particle sector. The spin evolution operator R corresponds to the Bosonic Green function, and the corresponding generating functional is constructed by including a source term J, bilinear in

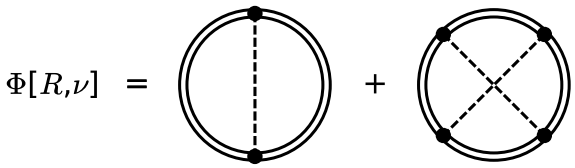

Figure 4.7: Diagrammatic expansion for the Luttinger–Ward functional. The first diagram gives the NCA, both diagrams the OCA.

$\boldsymbol{a} = (a_1, a_2)$,

$$Z[J] = \mathrm{Tr}_1\, \mathrm{T}_\tau\, \mathrm{e}^{-S[\boldsymbol{a},\boldsymbol{a}^\dagger] - \int \boldsymbol{a} J \boldsymbol{a}^\dagger} = \mathrm{e}^{-\beta F[J,\nu]} \tag{4.68}$$

$$R_{ij}(\tau_2, \tau_1) \equiv \langle \mathrm{T}_\tau \{a_i(\tau_2), a_j^\dagger(\tau_1)\}\rangle = \left.\frac{\delta \beta F[J,\nu]}{\delta J_{ij}(\tau)}\right|_{J=0} \tag{4.69}$$

The spin-spin correlation function is also naturally generated as the functional derivative of F with respect to ν. The Luttinger–Ward functional is obtained as a functional Legendre transformation, where R enters as the conjugate variable to J. In quantum field theory this is known as the two-particle irreducible (2PI) effective action [99, 103]. Diagrammatically, it is the sum of all closed diagrams constructed with bold (R) and dashed (ν) lines which are two-particle irreducible, *i.e.* in which removing two lines does make the diagram disconnected. The first two diagrams are shown in Fig. 4.7.

The Luttinger–Ward functional generates both the self-energy and the spin-spin correlation function via the functional derivatives

$$S(\tau) = \frac{\delta \Phi[R,\nu]}{\delta R(\beta - \tau)} \tag{4.70}$$

$$\chi(\tau) = \frac{2}{Z} \frac{\delta \Phi[R,\nu]}{\delta \nu(\beta - \tau)} \,. \tag{4.71}$$

Diagrammatically this corresponds to removing one bold or dashed line respectively. Truncating the expansion for Φ automatically gives an approximate form for S, which taken together with the Dyson equation (4.65) defines a self-consistent approximation scheme.

Note that removing a bold line from the first diagram in Fig. 4.7 gives the NCA contribution to the self-energy (4.66). The expansion of the Luttinger–Ward functional in the hybridisation gives a systematic way to construct self-consistent approximations, of which the first order is the NCA.

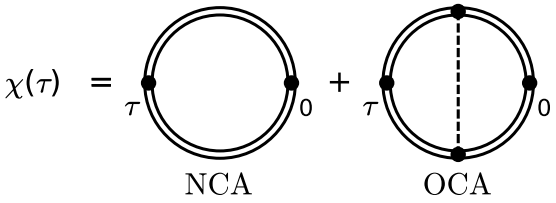

Figure 4.8: Diagrams expressing the spin-spin correlation function χ in terms of the local propagator R. Eq. (4.73,4.75).

4.4.3 Non-crossing and one-crossing approximations

We now return to the "first quantisation" picture. In this formulation, a systematic construction of the Luttinger–Ward potential as a 2PI effective action is not directly available. However, we can take the result of the construction outlined above as inspiration, and *define* an approximation scheme by constructing the Luttinger–Ward functional as the sum of bold, 2PI diagrams in the "first quantised" theory, and the self-energy as its functional derivative. We stress that while conceptually similar and represented with the same diagrams, the two formulations are in principle not equivalent.

At each order, we obtain an expression for $S(\tau)$ in terms of $R(\tau)$ and $R_0(\tau)$, which together with the Dyson equation defines a system of integral equations to be solved self-consistently for the dressed local propagator $R(\tau)$, in terms of which physical quantities are then computed. At any order in this expansion, the magnetisation is given by

$$m = \langle \sigma^x \rangle = \frac{1}{Z_H} \operatorname{Tr}\left[R(\beta)\sigma^x\right] = \frac{R_{11}(\beta) - R_{22}(\beta)}{R_{11}(\beta) + R_{22}(\beta)}, \tag{4.72}$$

while expressions for dynamical quantities, such as $\chi(\tau)$ have to be derived at each order.

As already discussed, from the first diagram in Fig. 4.7 we recover the NCA. In NCA, the σ^z correlation function is given by a single diagram, see Fig. 4.8, corresponding to the expression

$$\chi(\tau) = \frac{1}{Z} \operatorname{Tr}\left[R(\beta - \tau) R^c(\tau)\right]. \tag{4.73}$$

The second order contribution to Φ is represented by the second diagram in Fig. 4.7. The corresponding diagram for S (Fig. 4.6b) has two hybridisation lines, which cross. This leads to the one-crossing approximation (OCA), which self-consistently re-sums all diagrams of arbitrary order, in which *each hybridisation line* has at most one

crossing. The corresponding self-energy is

$$S_{\mathrm{OCA}}(\tau) = S_{\mathrm{NCA}}(\tau) + \int_0^\tau \mathrm{d}\tau_2 \int_0^{\tau_2} \mathrm{d}\tau_1 R^c(\tau-\tau_2)R(\tau_2-\tau_1)R^c(\tau_1)\nu(\tau_2)\nu(\tau-\tau_1). \quad (4.74)$$

The correlation function acquires the additional term (Fig. 4.8)

$$\begin{aligned}\chi_{\mathrm{OCA}}(\tau) &= \frac{1}{Z}\mathrm{Tr}[R^c(\beta-\tau)R(\tau)] \\ &+ \frac{1}{Z}\mathrm{Tr}\left[\int_\tau^\beta \mathrm{d}\tau_2 \int_0^\tau \mathrm{d}\tau_1 R^c(\beta-\tau_2)R(\tau_2-\tau)R^c(\tau-\tau_1)R(\tau_1)\right]\nu(\tau_2-\tau_1)\ . \quad (4.75)\end{aligned}$$

The expansion can be carried on to higher orders. However, starting from the third order, the order of the expansion for Φ does not coincides with the number of crossings in diagrams for S. The two-crossing approximation (TCA) actually includes diagrams at all orders, making it significantly more complicated than the OCA. In the context of DMFT, simplified versions of it have been developed, such as SUNCA and CTMA [99].

Here we only considered the additional contributions given by third order diagrams for Φ. The diagrams and the corresponding equations at third order are reported in Appendix 4.A. While computationally much more expensive than OCA, we found no significant improvement in the results, and therefore do not consider these additional contributions further.

4.4.4 Solution of replica equations

The self-consistent approximations derived above provide an approximate way to compute the σ^z correlation function given a fixed hybridisation ν. To apply this to the quantum p-spin we employ the same method described for the Monte Carlo: we solve iteratively the replica equations by computing the correlation function at each step, and using it to update the hybridisation (4.50). This creates a nested self-consistent procedure, in which convergence is required separately for the NCA/OCA equations at each step, and globally for the replicas equations.

4.5 Numerical results

4.5.1 diagMC

The diagMC algorithm samples configurations in continuous imaginary time. Correlation functions are stored on a grid of M points, which is also used to compute the weights. The resulting $\mathcal{O}(M^2)$ scaling of computational time allows to go to large

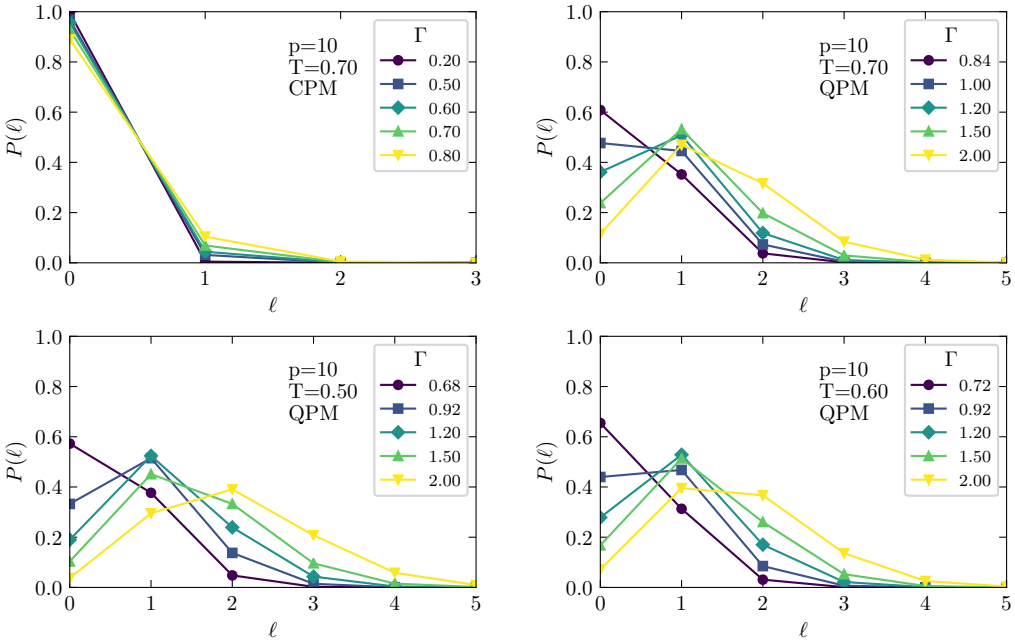

Figure 4.9: Distribution of the number of spin flips 2ℓ in the diagMC sampling.

values of M. We choose $M = 400$, which is well above the scale required for an accurate sampling of χ, $M \gg \beta\Gamma$ [93]. Each Monte Carlo run normally consists in 10^6 steps, of which 10^5 are sampled, preceded by 10^4 initialisation steps. The Monte Carlo sampling is iterated with the update rules (4.50), until convergence is detected with the procedure described in section 4.3.3, with a window r between 6 and 9.

As discussed in section 4.3.2, it is important for the diagMC sampling that there is no significant weight at arbitrarily high order in ℓ. We expect this to be the case for both the CPM and QPM solution. The former is characterised by small magnetisation; the latter is expected to approach the free quantum paramagnet, with typically fewer spin flips. Indeed, we see in Fig. 4.9 that the histograms for the distribution of spin flips are all peaked around some average value. This value increases with Γ, and provides the Monte Carlo estimate for the magnetisation (4.47).

Convergence is determined with the procedure described above, monitoring the quantity $\Xi = \int \chi(\tau)^p$. We use a window with r=6–9 and stop the iteration if it has not converged after 20 steps.

As expected, with the iterative diagMC we generally find two solutions of the replica symmetric equations, obtained by increasing Γ from small values or decreasing it from large values, corresponding to the CPM and QPM phases respectively. Fig. 4.10 shows the resulting hysteretic behaviour for Ξ and m. Some examples of the correlation

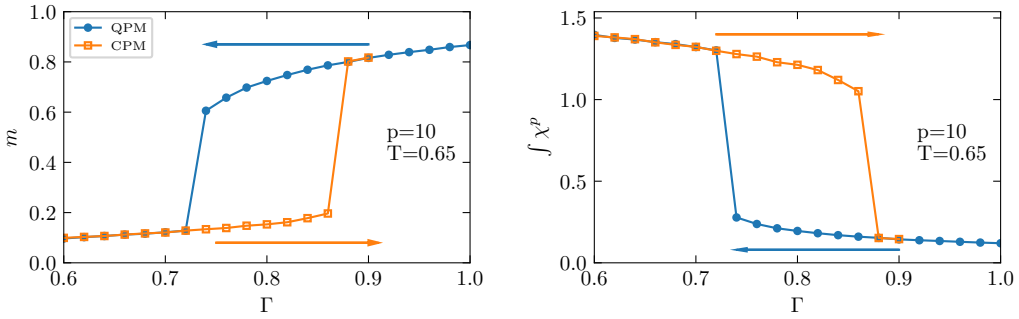

Figure 4.10: Tracking of solutions along Γ at fixed T, showing hysteresis in the coexistence region. The arrows indicate the direction along which each solution is tracked in Γ.

functions computed are reported in Fig. 4.11, comparing the two solutions for the same values of temperature and transverse field. For high enough temperature, the correlation functions computed following the small and large Γ solution are the same, and no hysteresis is present; as expected, the two solutions merge into one above the critical temperature.

Small Γ

For small values of the transverse field Γ, we expect the Monte Carlo sampling of the CPM solution to become difficult, due to the fact that the distribution of kinks is squeezed towards zero (see Fig. 4.9), implying a low probability of adding kinks in a MC step. One way around this would be to add "shift" moves, in which the number of spin flips in a trajectory is kept constant, but their times are moved.

To investigate whether this is necessary, we compare the diagMC results to perturbative $\Gamma \to 0$ analytical predictions, obtained by truncating the Γ expansion (4.34). This is different from what is done in [89, 90], in which the large p limit or the static approximation are considered; here we retain the full dependence on p.

We expand the correlation function $\chi(\tau)$ around the classical solution $\chi_0(\tau) = 1$. Only even powers of Γ contribute to the expansion (4.36). The first correction to χ is of order Γ^2 and can be time-dependent,

$$\chi(\tau) = 1 - \Gamma^2 \chi_1(\tau) + \mathcal{O}(\Gamma^4) \qquad \nu(\tau) = \frac{p}{2} - \Gamma^2 \frac{p(p-1)}{2} \chi_1(\tau) \ . \tag{4.76}$$

At each order in the expansion for Z_H, the exponential containing ν can be expanded, giving contributions to all higher order in Γ. Inserting (4.76) in (4.34)

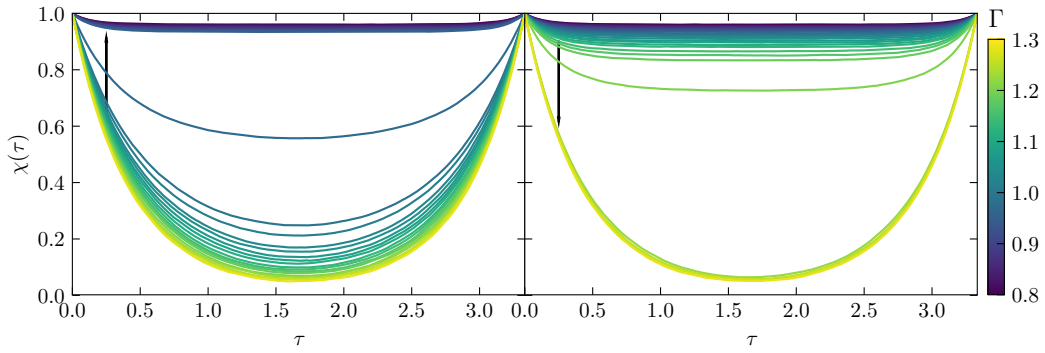

(a) $p = 3, T = 0.30$

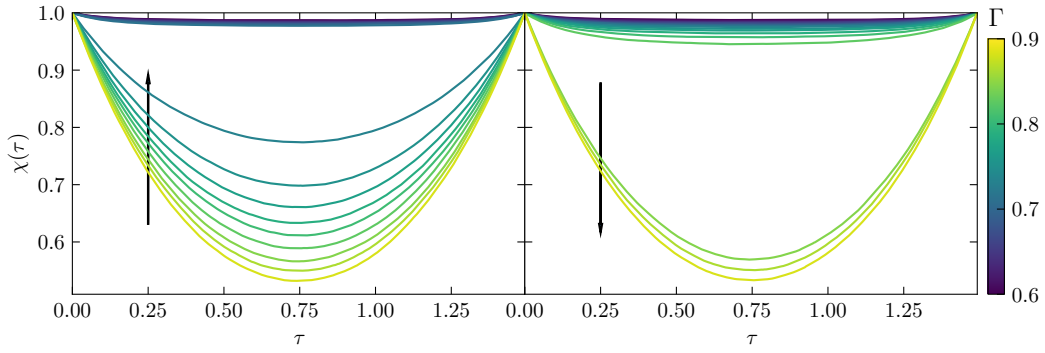

(b) $p = 10, T = 0.67$

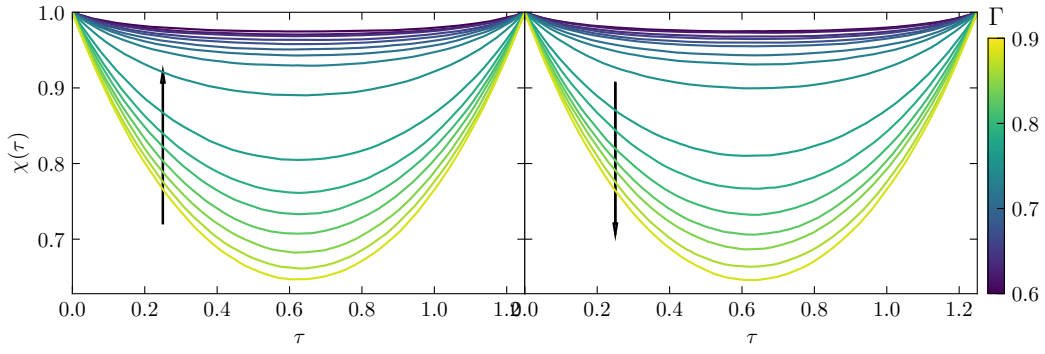

(c) $p = 10, T = 0.80$

Figure 4.11: Imaginary time correlation functions from diagMC, tracking the QPM (left) and CPM (right) solutions. The arrows indicate the direction along which the solutions are followed. For intermediate values of Γ, two different solutions are visible, except in panel (c), where $T > T_c$. Error bars are not plotted.

$$Z_H = 2\,\mathrm{e}^{\frac{1}{2}\int \nu \mathrm{d}\tau \mathrm{d}\tau'} + 2\Gamma^2 \int_0^\beta \mathrm{d}\tau_2 \int_0^{\tau_2} \mathrm{d}\tau_1\, \mathrm{e}^{\frac{1}{2}\int \nu\sigma\sigma' \mathrm{d}\tau\mathrm{d}\tau'} + \mathcal{O}(\Gamma^4) \tag{4.77}$$

$$= 2\,\mathrm{e}^{\frac{p\beta^2}{4}} + 2\Gamma^2 \int_0^\beta \mathrm{d}\tau_2 \int_0^{\tau_2} \mathrm{d}\tau_1\, \mathrm{e}^{\frac{p}{4}(\int \sigma)^2} + \mathcal{O}(\Gamma^4) \tag{4.78}$$

$$= 2\,\mathrm{e}^{\frac{p\beta^2}{4}} + \Gamma^2 \left(\sqrt{\frac{\pi}{p}}\beta \ \mathrm{erfi}\left(\frac{\sqrt{p}\beta}{2}\right) - \mathrm{e}^{\beta^2 p/4}\, \frac{\beta^2 p(p-1)}{2} \overline{\chi}_1 \right) + \mathcal{O}(\Gamma^4) \tag{4.79}$$

In the last equality we used that for a one-kink trajectory $\int \sigma(\tau) = \beta - 2\tau_2 + 2\tau_1$, and the resulting integral gives rise to $\mathrm{erfi}(z) = -\mathrm{i}\,\mathrm{erf}(\mathrm{i}z)$, while $\overline{\chi}_1$ indicates the average value in imaginary time. The same expansion for the correlation function (4.36) can be used to derive a self-consistent equation for $\overline{\chi_1}$, which can be solved numerically. However, this is not necessary to extract the first correction to the free energy and magnetisation.

In fact, we obtain the expressions for the free energy

$$f = -\frac{1}{4T} - T\ln 2 - \frac{\Gamma^2}{2}\sqrt{\frac{\pi}{p}}\,\mathrm{e}^{-\beta^2 p/4}\,\mathrm{erfi}\left(\frac{\sqrt{p}\beta}{2}\right) + \mathcal{O}(\Gamma^4) \tag{4.80}$$

and the magnetisation

$$m = -\frac{\partial f}{\partial \Gamma} = \Gamma\sqrt{\frac{\pi}{p}}\,\mathrm{e}^{-\beta^2 p/4}\,\mathrm{erfi}\left(\frac{\sqrt{p}\beta}{2}\right) + \mathcal{O}(\Gamma^3)\ . \tag{4.81}$$

Note that χ_1 does not appear in this expression. The corrections to the impurity partition function, and to the bath term in the free-energy both separately depend on $\overline{\chi_1}$. However the two contribution cancel out in the total free-energy. This is expected to hold at every order, as a consequence of the fact that the impurity and total magnetisations are the same.

At a given order in Γ, the corrections depend in a complicated way on p. At large p the result of Ref. [90] is recovered, $f = f_0 - \frac{\Gamma^2}{\beta p}$.

A comparison between diagMC data and the analytic expression (4.81) for the magnetisation is reported in Fig. 4.12 for $p = 3, 7, 10$. For all the temperatures considered, down to $T \gtrsim 0.2$ we find that the data are well described by the perturbative result to linear order for values of Γ up to at least 0.2–0.4. The values at which the cubic term becomes non-negligible depends on p and T. In particular, we extract the linear term coefficient by fitting to the data a function $\hat{m}(\Gamma) = a\Gamma + b\Gamma^3$, using least squares regression. We find that diagMC captures the correct coefficient for all the values of

the parameters considered (Fig. 4.12, right panels). The least square error increases with the temperature, due to the smaller range of Γ on which the fit is performed.

4.5.2 Self-consistent approximations

We looked for solutions of the replica symmetric equations by solving the impurity problem within the self-consistent approximations as described in section 4.4. For all the values of the parameter considered, down to $T = 0.20$, we find that only one solution is present at NCA, OCA and third order. The solution approximates the QPM one obtained with diagMC in the region in which the latter exists, with the agreement improving as Γ is increased. This is expected, as both solutions approach the free paramagnet at large Γ, with NCA and OCA accounting for some of the corrections induced by the hybridisation.

Self-consistent approximations have been used to study the Mott transition in the Hubbard model, see Ref. [104]. In that context, it was shown that the NCA only works deep in the insulating phase (corresponding to the QPM here), while OCA and third order are used to give lower bounds to the critical temperature by looking at jumps in the double occupancy (corresponding to the magnetisation). In contrast, the only sign of hysteretic behaviour we find is a slowing down of convergence near the QPM spinodal.

It is possible that hysteretic behaviour appears within OCA at lower temperature; however the temperatures we considered are already well below T_c, implying that OCA cannot capture the physics around the transition and in the coexistence region. Furthermore, we note that at the lower temperatures considered, the CPM solution is not physically relevant, and the phase diagram is described by the first-order transition between the QPM and the glass.

Fig. 4.13 shows a comparison between the magnetisations from diagMC, NCA and OCA. Hysteresis is shown by the two diagMC solutions. NCA and OCA approximate the QPM solution for large enough Γ, with OCA giving significant quantitative improvement at intermediate values of Γ. See Fig. 4.14 for a comparison at high Γ. Below the QPM spinodal, both NCA and OCA magnetisations are significantly larger than the CPM values found with diagMC.

Correlation functions are also computed within NCA and OCA. Some examples are shown in Fig. 4.15 confirming the situation described with the magnetisation. The OCA provides results practically indistinguishable from the diagMC estimate for the larger values of Γ shown.

Overall, we find that NCA and OCA fail to capture the phenomenology of the

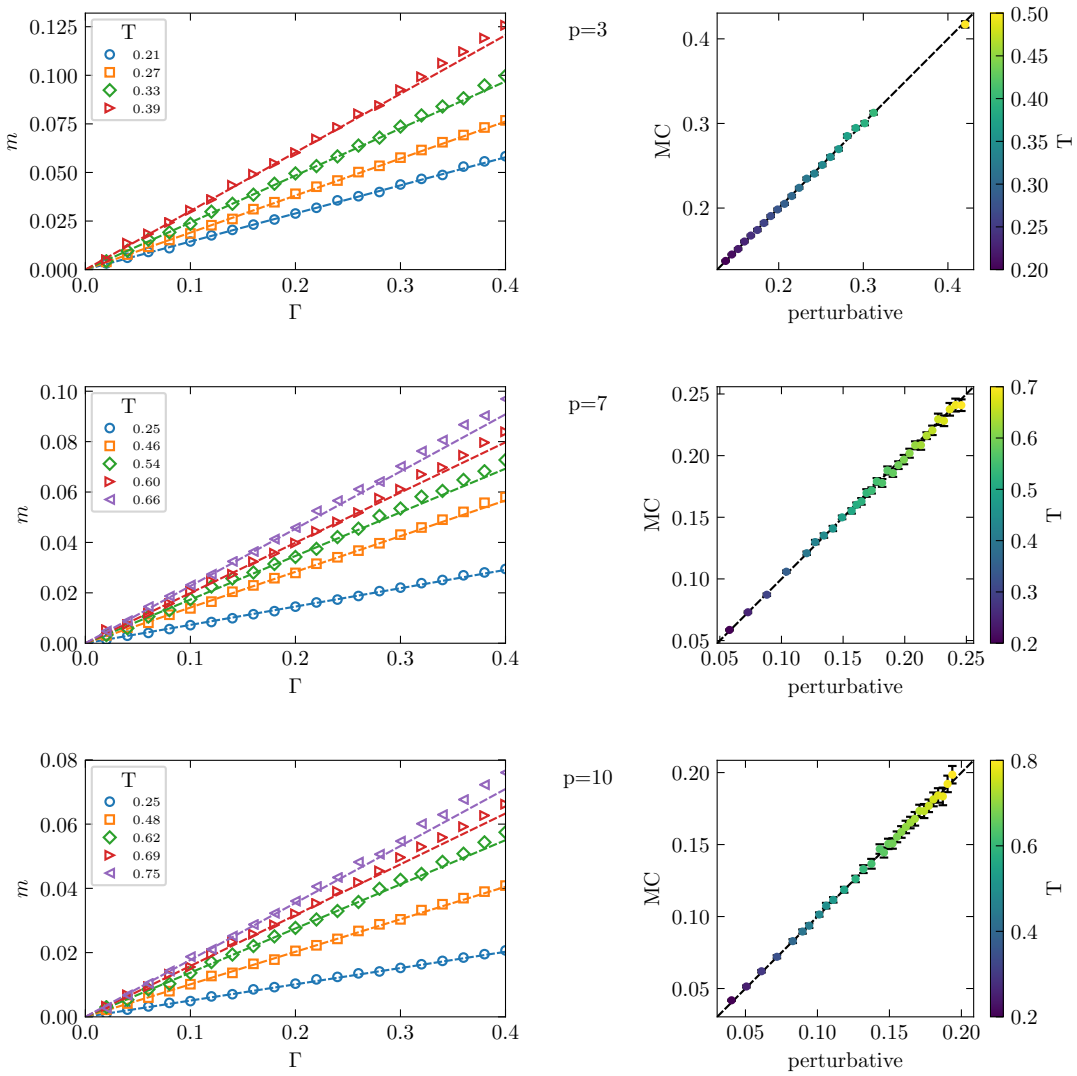

Figure 4.12: Comparison between diagMC and small Γ expansion. Left: magnetisations (4.81). Error bars (not plotted) would be the size of the markers or less. Right: the $\mathcal{O}(\Gamma)$ coefficients extracted by fitting the diagMC data correctly capture the $\Gamma \to 0$ behaviour.

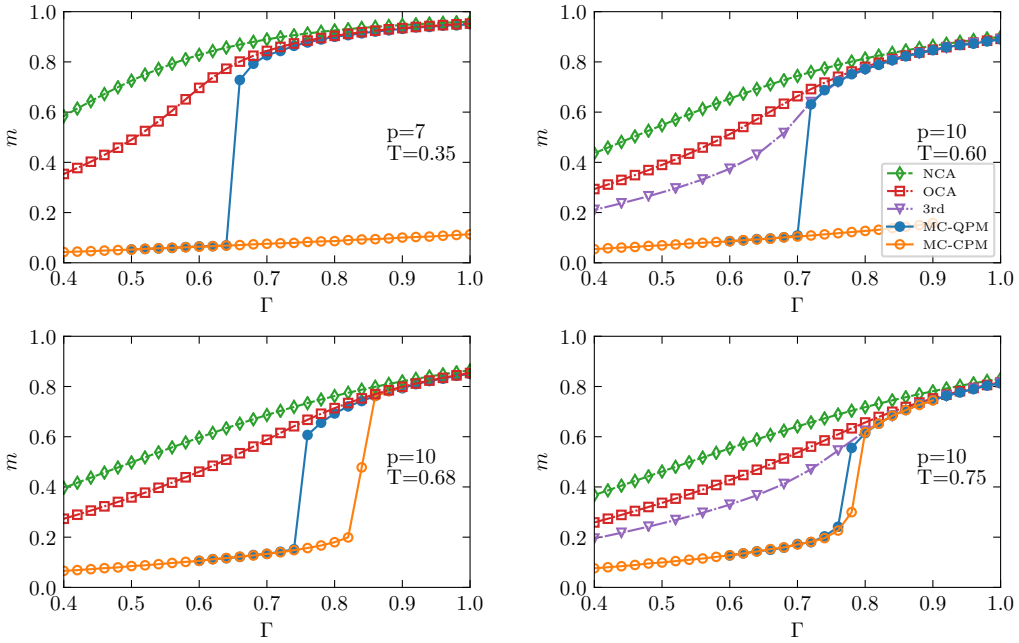

Figure 4.13: Magnetisations, comparing diagMC and self-consistent approximations. Error bars are not plotted and would be smaller than the markers (see Fig. 4.14).

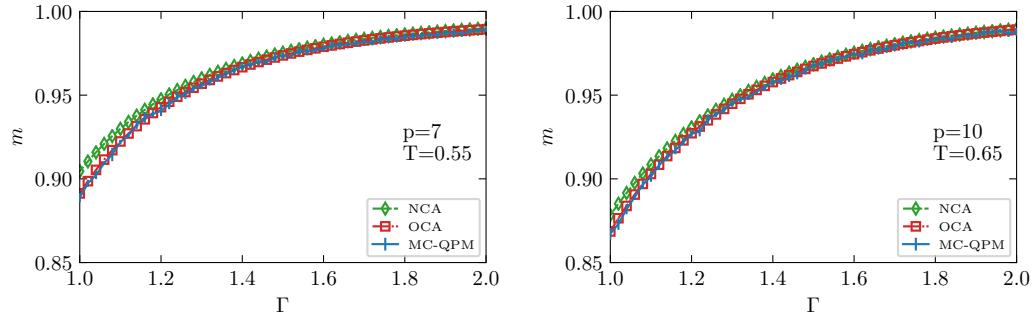

Figure 4.14: Magnetisations deep in the QPM phase. Error bars are plotted for the diagMC results, but barely visible.

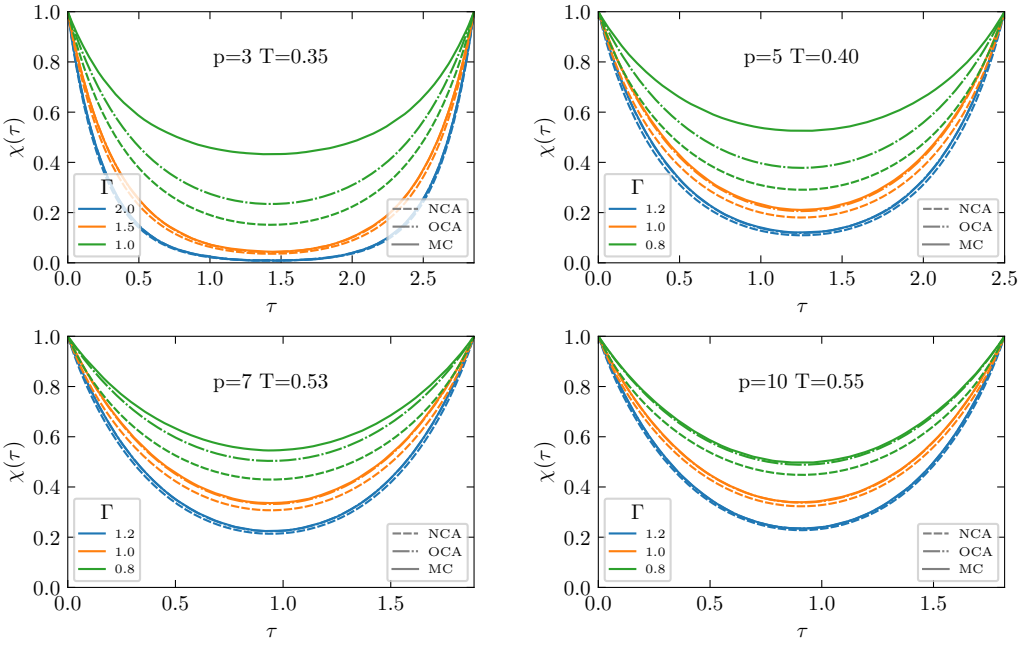

Figure 4.15: Correlation functions in the QPM phase, comparing diagMC, NCA and OCA results.

first order transition between the paramagnetic phases. The OCA provides a good approximation of the QPM phase above the coexistence region. In addition to the obvious advantage of being computationally much cheaper than Monte Carlo, the self-consistent approximations provide direct access to the impurity partition function, allowing to compute the full free energy at fixed T and Γ. Therefore, while the OCA computations cannot describe the critical line directly, they can be useful as a starting point for the diagMC thermodynamic integration.

4.5.3 Spinodals and critical line

To determine the region of existence of each of the replica symmetric solutions and compute the free energies we ran two separate set of simulations, in which the solutions are "followed" along Γ as described in section 4.3.3. We considered values $p = 3, 5, 7, 10$.

For all values, we followed the CPM solution from $\Gamma = 0$, and the QPM from $\Gamma = 2$, with steps $\delta\Gamma = 0.02$. At each step we ran the self-consistent solution algorithm first using diagMC with 10^4 steps, and then again with 10^6 steps. The first iteration has the purpose of both accelerating convergence, and reducing possible correlations

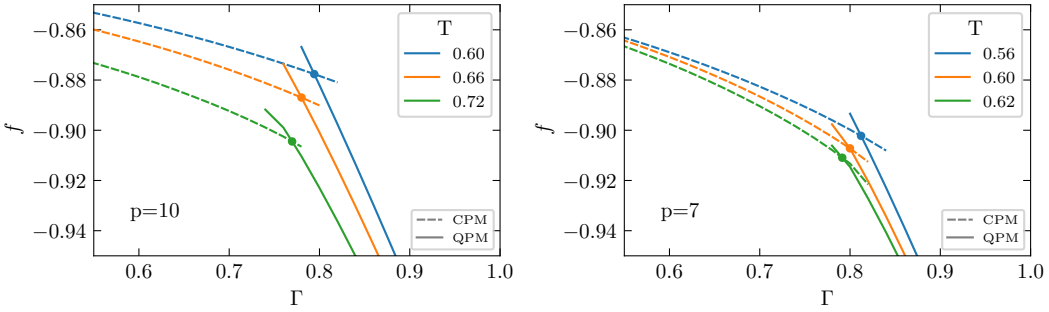

Figure 4.16: Free energies from thermodynamic integration of the diagMC magnetisations. The crossing between the CPM (dashed) and QPM (solid) curves determines the critical value of Γ separating the two phases, see Fig. 4.17.

between the simulations at different Γ. The second provides accurate estimates for the magnetisation and correlation functions.

The diagMC magnetisations are used to compute the free energy by thermodynamic integration (4.54). For the CPM we integrate from $\Gamma = 0$, using the classical free energy as initial condition. For the QPM, we use the OCA estimate at $\Gamma = 2$, which is within the regime OCA is essentially equivalent to the Monte Carlo. Integrating from lower values $\Gamma \gtrsim 1$ for $p = 10$ leads to detectable but not significant differences in the final results. The integrated free energies are obtained on a discrete grid in Γ. We use spline interpolation to obtain continuous curves, and find for each temperature the value of Γ at which they cross. Some examples are shown in Fig. 4.16.

The somewhat delicate procedure of thermodynamic integration on Monte Carlo data has the advantage that the free energies in the interesting range of intermediate values of Γ are obtained as the sum of many uncorrelated Monte Carlo quantities. In practice in our case this means that the relative error on the free energies is one order of magnitude smaller than that on the magnetisations. We find the estimates for the error on the magnetisation to be generally below 1% in the QPM phase and below 5% in the CPM phase.[3] Therefore, Monte Carlo errors do not affect significantly our analysis, and we do not discuss them further.

To detect the spinodals we ran a separate set of simulations, with $\delta\Gamma = 0.005$ and without the additional "fast" iteration between steps. At fixed temperature, we estimate the position of the spinodal as the first Γ for which the self-consistent solution is not found within 20 iterations. We then interpolate to obtain a smooth curve.

[3] Relative errors become large for $\Gamma \lesssim 0.1$, when the magnetisations are very small. However the small Γ analysis presented above implies that the estimates for the free energy are accurate, see Fig. 4.12.

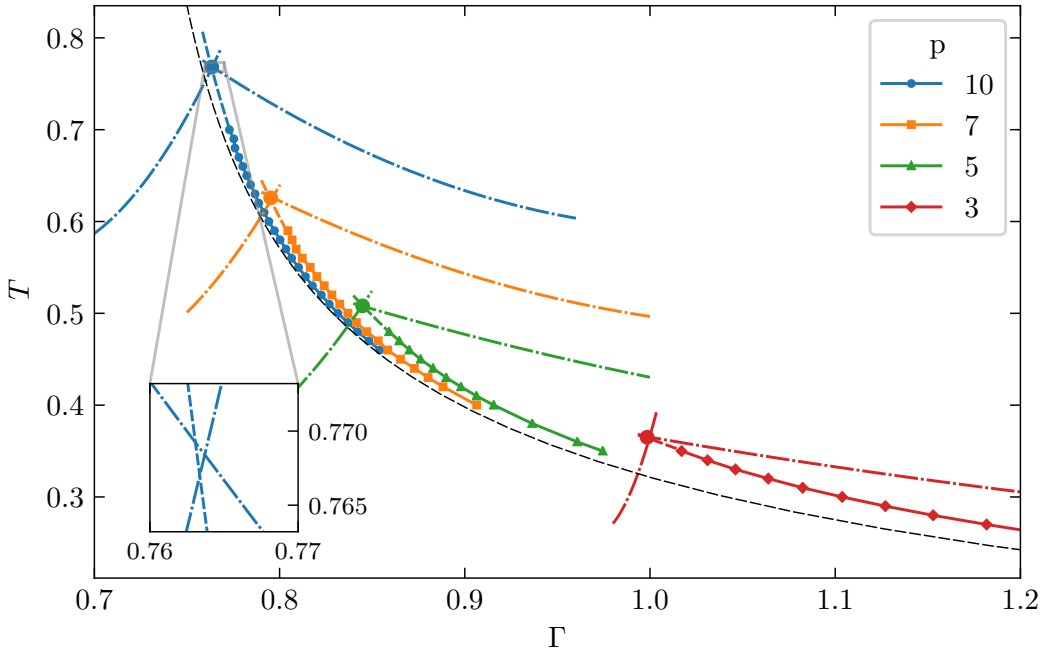

Figure 4.17: Critical lines between the CPM and QPM phases. The markers indicate the first order transition computed with diagMC and thermodynamic integration in Γ at fixed T. Close to the critical point iterative diagMC becomes unreliable and we consider a quadratic extrapolation (dashed lines). The critical points (large dots) are estimated from the crossing of the spinodals (dot-dashed) and the extrapolated critical line (see inset). For numerical values see Table 4.2. Increasing p, the critical line approaches the QREM value (4.23) (black dashed line).

In the vicinity of the critical point convergence becomes slow, making the iterative diagMC procedure impractical and unreliable. To describe the critical point and its vicinity, we take the data for the spinodals and critical line up to some $T < T_c$, and extrapolate using a quadratic curve. The result of this is presented in Fig. 4.17. For all the values of p, the three extrapolated lines cross in the same point to good accuracy (inset). Values of T_c and Γ_c to two significant figures are reported in Table 4.2. As p increases, the critical line approaches that of the QREM.

We stress that Fig. 4.17 does not characterise the full equilibrium phase diagram of the quantum p-spin model. Our analysis is limited to the replica symmetric level, capturing only the paramagnetic phases, and not the spin-glass phase that governs the low T and small Γ region. Moreover, we did not discuss the range of validity of the CPM solution. As in the classical case, we expect the solution to become unphysical

p	Γ_c	T_c
3	1.00	0.37
5	0.84	0.51
7	0.80	0.63
10	0.76	0.77

Table 4.2: Numerical estimates for the critical points, obtained as the triple crossing point of the extrapolated spinodals and critical line, see Fig. 4.17

below a curve in the (T, Γ) plane, on which its entropy vanishes. This means that the critical lines in Fig. 4.17 only describe a physical phase transition above a certain temperature, below which the transition is between the QPM and the glass.

4.6 Clustering and localisation transitions

4.6.1 QREM

As discussed in section 1.3 (see in particular Fig. 1.2), the quantum random energy model can be mapped to the Anderson tight binding model on an N-dimensional hypercube, in which the 2^N vertices represent the σ^z configurations, and the hopping rate is given by the field Γ. At $\Gamma \to 0$, the eigenstates coincide with the classical configurations, and the system is completely localised. At sufficiently large Γ the eigenstates are close to the σ^x basis, and are delocalised on the hypercube.

To discuss ergodicity and localisation, we briefly recall how the two transitions in the Rosenzweig–Porter model discussed in Chapter 2 can be identified by simple arguments. In the localised phase ($\gamma > 2$), eigenstates can be obtained by perturbation theory around completely localised vectors. Delocalisation happens when such perturbations become large, *i.e.* when

$$\mathcal{N}_\lambda \mathcal{M} \approx N^{1-\gamma/2} \gtrsim 1, \tag{4.82}$$

where $\mathcal{N}_\lambda = N\rho(\lambda)$ is the number of states at energy λ, which is of order N, and $\mathcal{M}$ is the matrix element between two sites. The localisation transition is indeed at $\gamma = 2$.

We apply the same argument to the localised phase of the QREM, noting that the matrix element between two configurations depends on their overlap q, and therefore we need to resolve the number of resonances $\mathcal{N}_E(q)$. The condition for delocalisation becomes

$$\max_q \left[\mathcal{N}_E(q)\mathcal{M}(q)\right] \gtrsim 1. \tag{4.83}$$

For clarity in the following we use the Hamming distance xN instead of the overlap $q = 1 - 2x$. Since the energy levels are independent,

$$\mathcal{N}_E(q) = \binom{N}{Nx} \frac{\mathrm{e}^{-E^2/N}}{\sqrt{\pi N}}. \tag{4.84}$$

Following [39], we estimate the matrix element by perturbation theory in the forward-scattering approximation (FSA) [19]. This consists in assuming that the matrix element between two configurations at distance x is given by the product of the xN spin flips, ignoring "loopy" contributions in which spins are flipped twice, that contribute at higher order in perturbation theory. There are $(nX)!$ such contributions. Almost all states have energy $\mathcal{O}(\sqrt{N})$, while $E \approx \mathcal{O}(N)$, therefore we take the energy differences appearing in the denominators to be E. The matrix element is

$$\mathcal{M} = \left(\frac{\Gamma}{E}\right)^{xN} (Nx)!, \tag{4.85}$$

resulting in

$$\mathcal{N}_E(q)\mathcal{M}(q) \approx \mathrm{e}^{Nf(x,\varepsilon,\Gamma)} \tag{4.86}$$

$$f(x, \varepsilon, \Gamma) = x \log\left(\frac{\Gamma}{e\varepsilon}\right) - (1-x)\log(1-x) - \varepsilon^2 \tag{4.87}$$

where $\varepsilon = |E|/N$. Spectral properties are symmetric and the results apply equally to positive and negative energies. However the physically relevant states, corresponding to positive temperature, have negative energy density.

The condition (4.83) becomes $\max_x f = 0$. If $\Gamma < \varepsilon$, f is always negative. Otherwise, the maximum of f is at $x_1 = 1 - \varepsilon/\Gamma$, leading to the implicit equation for the mobility edge

$$f(x_1, \varepsilon, \Gamma) = \frac{\varepsilon}{\Gamma} - \varepsilon^2 + \log\frac{\Gamma}{\mathrm{e}\,\varepsilon} \stackrel{!}{=} 0. \tag{4.88}$$

This can be solved numerically to determine $\Gamma_M(\varepsilon)$. We note that although it leads to the same calculations, our argument is different from that of [39], the common central point being the use of the FSA. Expanding (4.88) at small ε, we obtain

$$\Gamma_M(\varepsilon) = \varepsilon + \sqrt{2}\varepsilon^2 + \mathcal{O}(\varepsilon^3)\ . \tag{4.89}$$

In [39, 40] it is claimed that the first order, which in the context of this argument is a lower bound on Γ_M, gives the exact result for the mobility edge.

In the Rosenzweig–Porter model, a related but different condition determines the

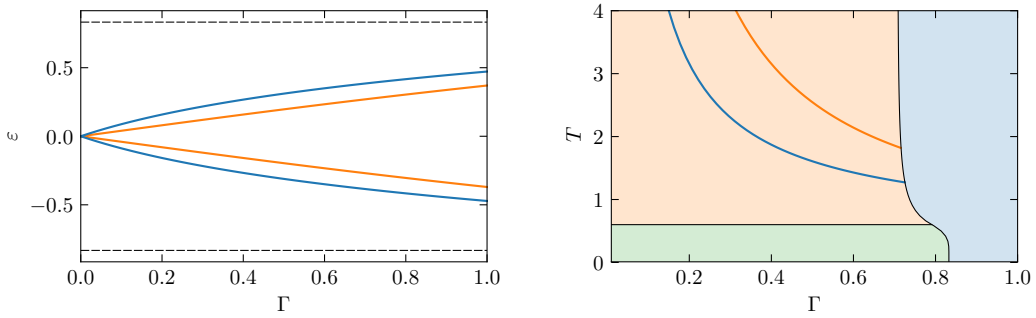

Figure 4.18: Localisation (blue) and ergodic (orange) transition lines in the QREM. Left: microcanonical phase diagram. Black dashed lines are the edges of the spectrum. Right: the corresponding lines in the canonical phase diagram, within the CPM phase.

ergodic transition, see the discussion around (2.29). The condition involves the square of the matrix elements. Within the same approximations as above,

$$\mathcal{N}_E(q)|\mathcal{M}(q)|^2 \approx \mathrm{e}^{N f_2(x,\varepsilon,\Gamma)} \tag{4.90}$$

$$f_2(x,\varepsilon,\Gamma) = x\log x - (1-x)\log(1-x) - \varepsilon^2 + 2x\log\left(\frac{\Gamma}{e\varepsilon}\right) . \tag{4.91}$$

The condition for the ergodic transition is $\max_x f_2 = 0$. If $\Gamma < 2\varepsilon$, f_2 is always negative; otherwise, the maximum is at $x_2 = (1-q)/2$, $q = -\sqrt{1-(2\varepsilon/\Gamma)^2}$. The condition

$$f_2(x_2,\varepsilon,\Gamma) \stackrel{!}{=} 0 \tag{4.92}$$

gives an implicit equation that can be solved numerically for the ergodic transition line $\Gamma_E(\varepsilon)$.

The argument presented here suggests that the QREM undergoes two separate localisation and ergodicity transitions. For a given energy density ε, the eigenstates become delocalised when the field is increased above a critical value $\Gamma_M(\varepsilon)$ determined by (4.88), while ergodicity is recovered only above $\Gamma_E > \Gamma_M$, determined by (4.92). The curves obtained are reported in Fig. 4.18. The right panel reports the curves on the equilibrium phase diagram obtained from the static approximation. The lines divide the CPM phase into three regions: a localised one for $T < \Gamma_M$, an ergodic one for $T > \Gamma_E$, and an intermediate extended, non-ergodic region similar to the one described in the Rosenzweig–Porter model. We truncate the curves where they intersect the first-order transition line between CPM and QPM, where we expect the forward-scattering approximation not to be valid. The QPM phase is therefore ergodic.

4.6.2 p-spin: counting resonances

The localisation properties of the quantum p-spin model can be analysed along the lines of the argument described above for the QREM. In Chapter 3 we describe how the classical states of the p-spin are organised, by computing the typical number of states with the same energy and a given overlap with a fixed configuration, the quenched overlap-resolved entropy $s(\varepsilon_0, q_0)$. We showed that below some temperature T^* there is a small cluster of states with high overlap, separated by the bulk of the states by a gap of overlaps at which there are no configurations.

This structure was described in [41]. The annealed calculation presented there captures the general phenomenology of this clustering transition and gives a good description of the bulk, but overestimates the size of the clusters and underestimates T^*. On the other hand, the matrix element between two configurations is computed at the quenched level, leading to a replica-symmetric forward-scattering approximation. The authors also argue that there is no replica symmetry breaking. The resulting typical amplitude has the form $\mathrm{e}^{Nk(q)}$,

$$k(q) = -\frac{1}{2}\int_q^1 \mathrm{d}q' \ln(1-q'^p) + \frac{1}{2}(1-q)\ln\left(\frac{\Gamma(1-q)}{2e|\varepsilon_0|}\right) . \tag{4.93}$$

The typical entropy of resonances is then given by $f_p(q) = k(q) + s(\varepsilon_0, q)$. When using this to determine the delocalisation transition, the structure of the clusters needs to be taken into account. Expanding around $q = 1 - \eta$,

$$k(1-\eta) = -\frac{\eta}{2}\ln(p\eta) + \mathcal{O}(\varepsilon) \tag{4.94}$$

showing that for high enough overlap, $k > 0$. This implies that there are always resonances at high overlap. This is expected since contrary to the REM, the energy of configurations with high overlap are strongly correlated.

For energies corresponding to $T > T^*$, there are no clusters and the FSA result breaks down for arbitrary small Γ. The state considered hybridises with other configurations at high overlap, which in turn hybridise with other configurations and so on. Therefore there is no localised phase above the clustering transition.

On the other hand, if $T < T^*$, the fact that f is positive at high overlap only implies that the states hybridises with other configurations within the cluster. In principle, one should then diagonalise the Hamiltonian within a cluster, and then repeat the FSA argument with the states obtained. As claimed in [41], this does not significantly affect the analysis, due to the clusters being small, particularly at high p. The 1RSB

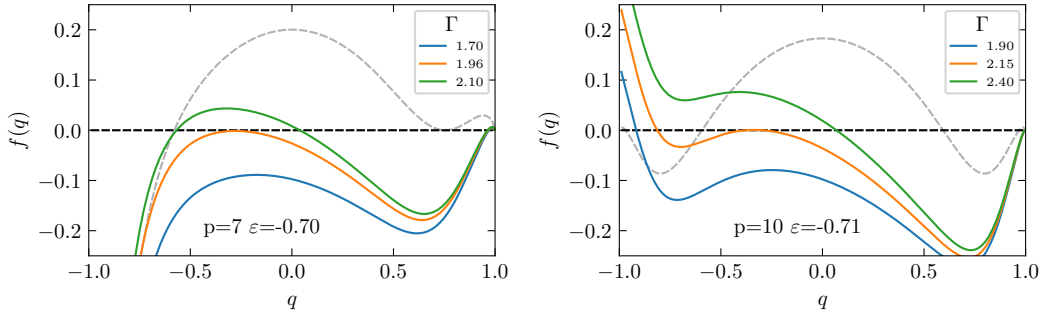

Figure 4.19: Entropy of resonances in the quantum p-spin model. Curves obtained from the annealed overlap-resolved energy, and the RS-FSA amplitude. Below the clustering transition, the states are delocalised if f becomes positive within the bulk. The annealed entropy (dashed line) accurately describes the bulk.

analysis in Section 3.3.2 shows that the clusters are significantly smaller, making the premise to the argument stronger.

One then needs to analyse whether there are resonances within the bulk of states at low overlap. This is illustrated in Fig. 4.19. For small Γ, there are resonances only within the cluster (blue lines). The states are delocalised over an extensive number of configuration, which is a small but finite fraction of the total. Increasing Γ, f becomes positive for some values of q deep in the bulk (green lines). The states then hybridise with configurations in the bulk, and the FSA breaks down, implying delocalisation. The transition is given by the value Γ_* for which the maximum of f within the bulk is zero (orange lines).

Since the energies of configurations at low overlap are weakly correlated, the entropy in the bulk is well described by the annealed calculation (see Chapter 3). The quenched calculation provides a more accurate estimate of T_*, but does not change significantly the results for Γ_*.

The localisation transition lines obtained in this way are shown in Fig. 4.20. There is a central band $|\varepsilon| < |\varepsilon|_*$ in which all states are delocalised. Outside of it, the curve $\Gamma_*(\varepsilon)$ separates a delocalised phase from one in which eigenstates are only delocalised within each cluster. This is not a MBL phase, but a factorisation of the Hilbert space, reminiscent of symmetry sectors in random matrix theory [105]. For example, GOE level spacing is observed within the clusters, which is blurred into Poisson if the uncorrelated states from different clusters are considered [41].

The right panel of Fig. 4.20 shows the transposition of the curves to the $T-\Gamma$ plane. For reference, the area of the plot is coloured according to the QREM phase diagram.

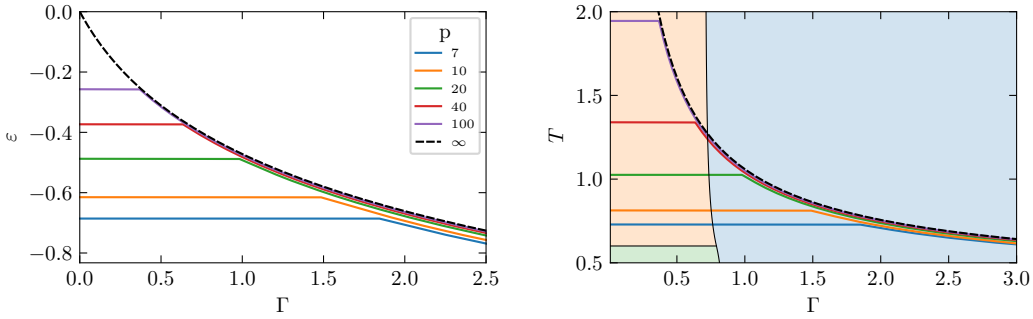

Figure 4.20: Delocalisation transition lines in the quantum p-spin model from RS-FSA. The curves start horizontal at ε_* (microcanonical - left) or T_* (canonical - right) until a critical value Γ_*, after which the lines describe curves that at large p approach the QREM mobility edge (black dashed line). For small p, (T_*, Γ_*) lies deep in the QPM phase or above the critical point.

As p is increased, the Γ_* curve approaches that of the QREM, and T_* diverges, so that the QREM result is indeed recovered.

Most results in [41] are derived at large p, but it is also claimed that the qualitative picture applies to all p. Our analysis essentially confirms the description at large p, and provides a more accurate calculation of T_*. However, we note that at small p (at least up to 20), the value of Γ_* is very high. In particular, it lies deep within the QPM phase, in which the FSA is expected to break down. Moreover, the FSA argument suggest that there is a delocalisation line within the CPM phase, that ends at the critical line. By comparing the result for T_* from Chapter 3, with the critical temperatures from diagMC (Table 4.2), we note that at least up to $p \lesssim 10$, $T_* > T_c$, leaving the domain of applicability of the FSA to small p unclear. On the other hand, the asymptotic scalings ensure that $T_* \ll T_c$ at large p.

4.7 Discussion and conclusion

In this chapter we presented an analysis of some equilibrium and non-equilibrium phase transitions in the quantum p-spin model. The equilibrium phase diagram is analysed with the replica method; the solution of the replica equations differs from the classical case by the necessity to compute the imaginary-time correlation function. This was previously done within the static approximation, and discrete-time numerical techniques.

We developed a numerically exact method for the computation of the imaginary-time correlation function based on diagrammatic Monte Carlo in continuous time, and

applied it to the replica symmetric equations. The method effectively samples classical spin trajectories and is not affected by the sign problem, and simulations can be run on desktop computers or small clusters.

At the RS level the system has two phases, a classical paramagnet at low transverse field and a quantum paramagnet at high field. The two are separated by a first-order transition line, which ends at a finite-T critical point. The iterative diagMC method allows to accurately compute the correlation function in a wide range of parameters, and to determine when the two phases are stable (*i.e.* the spinodal lines). The expected hysteretic behaviour with the transverse field is found in the correlation function and magnetisation. Monte Carlo sampling does not give direct access to the free energy, which we computed for each phase by thermodynamic integration. We accurately determined the first-order transition line and its critical endpoint for several values of p.

Increasing p, the transition line approaches the one found in the static approximation, and the critical temperature diverges. This confirms that the static approximation correctly estimates the free energy of the QREM. Looking at the diagMC results, it is clear that a flat correlation function is a reasonable approximation in the CPM phase, but is far from correct in the QPM phase.

We derived and implemented a class of approximation schemes, the non-crossing approximation and its second and third order generalisations, which are used in the dynamical mean field theory of strongly correlated electrons. By thorough comparison with the diagMC results, we verified that these approximations are very accurate in the QPM phase, but they fail to capture the CPM phase and the transition. Increasing the order enlarges the range of Γ in which the approximation is good, but only above the transition. Overall the self-consistent approximations give a computationally inexpensive good description of the QPM phase, with direct access to the free energy.

We focused on the RS region of the phase diagram, which contains the values of temperature relevant for ergodicity and localisation transitions (for example, the dynamical and clustering transitions discussed in Chapter 3). The model undergoes replica symmetry breaking to a spin-glass phase . The diagMC method can be extended to solve the 1RSB equations, the diagonal part of which is again the DMFT-like imaginary-time correlation function. The self-consistent approximations can also be extended to the 1RSB equations; however, the fact that they fail to capture the low-Γ RS phase suggests that this is not a promising direction.

After the accurate description of the equilibrium phases, we concentrated on local-

isation and ergodicity transitions. We presented an argument, based on the forward-scattering approximation and informed by the generalised Rosenzweig–Porter random matrix model (GRP, see Chapter 2), for the two transition lines in the QREM. The argument for the MBL transition is similar but distinct from that of [39], and it leads to the same estimate. Our argument indicates that, in analogy to GRP, increasing Γ the model undergoes two separate transitions: first the eigenstates delocalise, then ergodicity is restored at higher field. The equilibrium CPM phase includes an extended, non-ergodic region, as well as localised and ergodic ones.

For the p-spin model, we revisited the RS-FSA argument of [41] in light of the improved calculation of the overlap-resolved entropy (Chapter 3). For $\Gamma = 0$, the system undergoes a clustering transition at a temperature T_* that is computed correctly with the quenched calculation. The mechanism for de-clustering via hybridisation with the bulk is essentially unaffected by the improved calculation, and we confirm that at large p it indicates a transition line within the CPM phase, which converges to the MBL line of the QREM for $p \to \infty$. However, for $p \lesssim 20$–40, the estimated de-clustering point lies deep within the QPM phase, or above the critical point, casting doubts on the applicability of the clustering picture at not-too-large p and finite Γ. On the other hand the dynamical transition can be characterised at finite Γ by studying the equilibrium replica equations at the 1RSB level [93]. The 1RSB equations can still be treated as an impurity problem with an additional longitudinal field, which could be solved with an iterative diagMC method, extending the one we proposed. The self-consistent approximations on the other hand do not seem to work in this region of the phase diagram.

In any case it is worth stressing that the clustered phase differs significantly from both MBL and NEE phases. For arbitrarily small Γ, the eigenstates are delocalised over the whole cluster, the size of which is determined by T and p. Within the cluster, the dynamics is expected to be ergodic, and in [41] it is suggested that the level spacing statistics is globally Poissonian, but Wigner–Dyson within a cluster. All of this indicates the Hilbert space breaking into sectors corresponding to each cluster rather than disorder-induced localisation transitions. This is similar to the factorisation due to symmetry, well known since the early days of random matrix theory [105], with the notable feature that the number of sectors is exponentially large, and further breaking of replica symmetry is expected to induce an even richer structure. It would be interesting to study this in more detail and compare it with random matrix models with hierarchical structure, see *e.g.* [106].

Finally we note that while the work presented here focussed mostly on the equilib-

rium phase diagram, it leads naturally to a new way to study the dynamical evolution of the model. The formalism for the imaginary-time correlation function can be extended to the Keldysh contour [103, 107], and diagMC then provides a numerically exact method to study the real-time dynamics. The formalism was recently established in [108], focussing on the spherical p-spin model. As discussed there, the solution of the equilibrium equation is needed as input for the solution of real-time evolution. This provides a promising way to study the dynamical nature of the CPM phase directly, overcoming the limitations of exact diagonalisation.

Appendix

4.A Third-order self-consistent approximation

The third order contributions to the Luttinger–Ward functional are given by the two diagrams in Fig. 4.21a. Contrary to OCA and NCA, the second diagram gives rise to multiple diagrams for S and χ, depending on which lines are removed.

The resulting four diagrams in Fig. 4.21b contribute to the self-energy, leading to

$$S_3(\tau) = S_{\mathrm{OCA}}(\tau) + \int \mathrm{d}\tau_1 \dots \mathrm{d}\tau_4 T(\tau, \tau_1, \tau_2, \tau_3, \tau_4) h(\tau, \tau_1, \tau_2, \tau_3, \tau_4) \tag{4.95}$$

where T collects the contribution from the local propagators, which is the same for all diagrams

$$T(\tau, \tau_1, \tau_2, \tau_3, \tau_4) = R^c(\tau - \tau_4) R(\tau_4 - \tau_3) R^c(\tau_3 - \tau_2) R(\tau_2 - \tau_1) R^c(\tau_1) \tag{4.96}$$

and the scalar function h the four different contributions from hybridisation lines

$$\begin{aligned} h(\tau, \tau_1, \tau_2, \tau_3, \tau_4) = {} & \nu(\tau_2)\nu(\tau_4 - \tau_1)\nu(\tau - \tau_3) + \nu(\tau_4)\nu(\tau_3 - \tau_1)\nu(\tau - \tau_2) \\ & + \nu(\tau_3)\nu(\tau_4 - \tau_1)\nu(\tau - \tau_2) + \nu(\tau_3)\nu(\tau - \tau_1)\nu(\tau_4 - \tau_2) \ . \end{aligned} \tag{4.97}$$

Finally, the correlation function has contributions from the four diagrams in Fig. 4.21c,

$$\begin{aligned} \chi_3(\tau) = \chi_{\mathrm{OCA}}(\tau) & + \frac{1}{Z} \int_{\tau_1 < \tau_2 < \tau < \tau_3 < \tau_4} \mathrm{d}\tau_1 \dots \mathrm{d}\tau_4 \, \mathrm{Tr}\, U(\tau_1, \tau_2, \tau, \tau_3, \tau_4) g(\tau_1, \tau_2, \tau_3, \tau_4) \\ & + \frac{1}{Z} \int_{\tau_1 < \tau_2 < \tau_3 < \tau < \tau_4} \mathrm{d}\tau_1 \dots \mathrm{d}\tau_4 \, \mathrm{Tr}\, U(\tau_1, \tau_2, \tau_3, \tau, \tau_4) \nu(\tau_4 - \tau_2)\nu(\tau_3 - \tau_1) \\ & + \frac{1}{Z} \int_{\tau_1 < \tau < \tau_2 < \tau_3 < \tau_4} \mathrm{d}\tau_1 \dots \mathrm{d}\tau_4 \, \mathrm{Tr}\, U(\tau_1, \tau, \tau_2, \tau_3, \tau_4) \nu(\tau_4 - \tau_2)\nu(\tau_3 - \tau_1) \end{aligned} \tag{4.98}$$

$$U(\tau_1, \tau_2, \tau_3, \tau_4, \tau_5) = R(\beta - \tau_5) R^c(\tau_5 - \tau_4) R(\tau_4 - \tau_3) R^c(\tau_3 - \tau_2) R(\tau_2 - \tau_1) R^c(\tau_1) \tag{4.99}$$

$$g(\tau_1, \tau_2, \tau_3, \tau_4) = \nu(\tau_4 - \tau_2)\nu(\tau_3 - \tau_1) + \nu(\tau_4 - \tau_1)\nu(\tau_3 - \tau_2) \ . \tag{4.100}$$

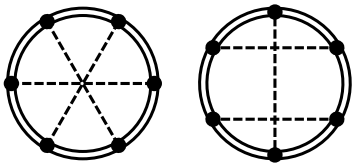

(a) Third order diagrams for the Luttinger-Ward potential $\Phi[R, \nu]$.

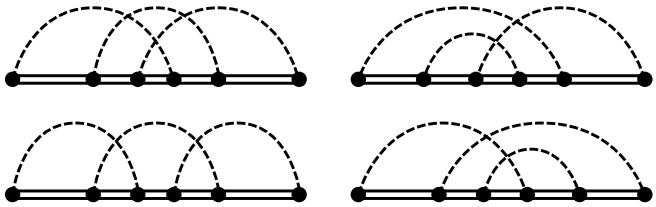

(b) Third order diagrams for the self-energy $S(\tau)$.

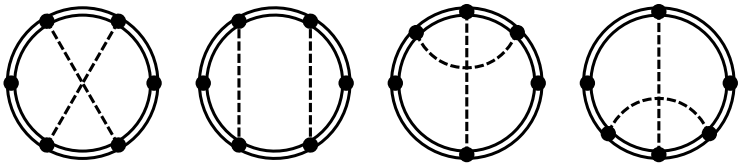

(c) Third order diagrams for the correlation function $\chi(\tau)$.

Figure 4.21: Self-consistent approximation: third order diagrams.

5 A bridge between models of glasses and of black holes

The Sachdev–Ye–Kitaev (SYK) is a model of disordered Fermions, that has recently attracted much interest in the string theory community. It originates from the model introduced by Sachdev and Ye [109] as a mean-field model of a random quantum magnet, which was later studied at the interface of quantum spin glasses and non-Fermi-liquid metals [110–112].

Kitaev introduced the variant of this model now called SYK in a series of talks [113] (the main ideas and results are detailed in [114]) in which some peculiar properties of the model, and of its low-temperature physics in particular, are highlighted. Despite the ground state being non-degenerate, SYK has finite zero-temperature entropy, and specific heat scaling linearly with the temperature.

Furthermore, in the low-temperature limit the model develops an approximate time-reparametrisation invariance, similar to a (broken) conformal symmetry. The reparametrisation invariance allows for an exact solution of the model by computing the invariant correlation functions. The construction of an effective theory for the soft modes leads to an action based on the Schwarzian derivative. The same Schwarzian action appears in two-dimensional gravity, providing a realisation of the holographic principle related to the AdS/CFT correspondence. Finally, it was shown that the SYK model is *maximally chaotic*, meaning that its Lyapunov exponent saturates a quantum bound, see [115, 116]. Taken together, these properties have led to a great interest in SYK as a simple, solvable model of holographic black holes, which was lacking since the proposal of the AdS/CFT correspondence [114, 117].

It is interesting to note that in the original formulation of Sachdev and Ye, representative of the "glassy" point of view, it is a mean-field model representing the infinite-dimensional limit of a lattice of $N \gg 1$ sites. From the field theoretical/"stringy" point of view, it is a 0+1-dimensional theory, representing a new class of large-N theories in the same spirit of vector $O(N)$ models, and the simplest example of a holographic correspondence between one and two-dimensional spacetimes. These two points of

view are not in contradiction, but rather offer complementary perspectives.

An emergent time-reparametrisation is present in a similar way in the dynamics of models of glasses at long time. This has been known since early works on spin glass dynamics, and was a key feature in the analytic treatment of mean-field models leading to the Cugliandolo–Kurchan equations [118], in which a family of solutions of the asymptotic (low frequency) equations is found. To find the exact solution, one then needs to select the time parametrisation by matching the high and low frequency regimes, a hard task in practice. It was later realised that the reparametrisation has a physical meaning in terms of dynamical fluctuations in the ageing of glassy materials, and it was proposed by Chamon, Cugliandolo and collaborators as the basis for a universal description of glassy dynamics, see [119] and references therein. In a series of paper, they constructed a theoretical framework based on time-reparametrisation invariance as a symmetry, and tested its predictions in a variety of models, including finite dimensional and kinetically constrained models. This is a promising path towards a unified theory of glassy dynamics, the main difficulty being the construction of the action for the reparametrisation soft mode (*i.e.* the analogue of the Schwarzian action in SYK).

Given the formal analogies, it is interesting to investigate to what extent the peculiar properties of SYK-like models and those of glasses are manifestations of the same underlying structures, and to build a connection between them. In this chapter we present the first steps in this direction, with the goal of facilitating the interchange of ideas between theories of glasses and of black holes.

In Section 5.1 we give a brief overview of the SYK model, and show that there is no glass transition at any $T > 0$. In Section 5.2 we introduce a quantum model constructed from the Fokker-Planck operator of a classical mean-field glass model. The quantum model inherits the reparametrisation invariance from the classical glassy dynamics. We show that it has finite entropy at zero temperature, corresponding to the exponential number of metastable states of the glass, and we compute the scaling of the specific heat and some features of the correlation functions within a harmonic approximation.

5.1 The Sachdev–Ye–Kitaev model

5.1.1 Annealed free energy

The Sachdev-Ye-Kitaev model [114] is a model of N Majorana Fermions in 0+1 dimensions with a random q-body interaction

$$H_{\mathrm{SYK}} = (\mathrm{i})^{\frac{q}{2}} \sum_{i_1<\cdots<i_q}^{N} J_{i_1\ldots i_q}\psi_{i_1}\cdots\psi_{i_q} \ . \tag{5.1}$$

$$\{\psi_i,\psi_j\} = 2\delta_{ij}, \qquad \psi_i^\dagger = \psi_i \tag{5.2}$$

Both N and q are even integers. The coupling $\mathbf{J}$ is a totally antisymmetric random tensor, its independent components i.i.d. normally distributed with zero mean and variance $\frac{J^2(q-1)!}{N^{q-1}}$. The Hamiltonian is similar to that of the p-spin model discussed in the previous chapters, with the difference that the Hilbert space has dimension $2^{N/2}$ instead of 2^N. This is due to the Majorana nature of the degrees of freedom, and has relevant consequences, as discussed in the next section.

Here we sketch the derivation of the annealed free energy of the SYK model, obtaining the equations for the imaginary-time propagator and self-energy. In the next section we show that the annealed result is correct at any temperature, *i.e.* the SYK model does not have a glassy phase. The annealed free energy is obtained by taking the average of the imaginary-time path integral

$$\begin{aligned}\bar{Z} &= \int \mathcal{D}\boldsymbol{\psi}\, \mathrm{e}^{-S_0} \prod_{i_1<\cdots<i_q} \overline{\mathrm{e}^{-(\mathrm{i})^{\frac{q}{2}} J_{i_1\ldots i_q}\int_0^\beta \psi_{i_1}\cdots\psi_{i_q}(\tau)}} \\ &= \int \mathcal{D}\boldsymbol{\psi}\, \mathrm{e}^{-S_0 + \frac{NJ^2}{2q}\int_0^\beta \mathrm{d}\tau_1 \int_0^\beta \mathrm{d}\tau_2 \left(\frac{1}{N}\sum_i \psi_i(\tau_1)\psi_i(\tau_2)\right)^q + \mathcal{O}(N^0)} \ ,\end{aligned} \tag{5.3}$$

where $S_0 = \int \psi\partial_\tau\psi$ is the free Fermion action. Introducing the constraint $\hat{G}(\tau_1,\tau_2) = \frac{1}{N}\sum_i \psi_i(\tau_1)\psi_i(\tau_2)$, we can rewrite the averaged partition function as a path integral in $\hat{G}$ and the corresponding Lagrange multiplier Σ, the Fermions can be integrated out

$$\bar{Z} = \int \mathcal{D}\hat{G}\mathcal{D}\Sigma\, \mathrm{e}^{-\frac{N}{2}\operatorname{Tr}\Sigma\hat{G} + \frac{NJ^2}{2q}\operatorname{Tr}\hat{G}^q} \left(\int \mathcal{D}\psi\, \mathrm{e}^{-\frac{1}{2}\int\int \psi(\partial_t - \Sigma)\psi}\right)^N = \int \mathcal{D}\hat{G}\mathcal{D}\Sigma\, \mathrm{e}^{-NS[\hat{G},\Sigma]} \ . \tag{5.4}$$

$$S[\hat{G},\Sigma] = \frac{1}{2}\int_0^\beta \mathrm{d}\tau_1\mathrm{d}\tau_2 \left[\Sigma(\tau_1,\tau_2)\hat{G}(\tau_1,\tau_2) - \frac{J^2}{q}\hat{G}(\tau_1,\tau_2)^q\right] - \frac{1}{2}\ln\det\left(\partial_t - \Sigma\right) \ . \tag{5.5}$$

The saddle point of S is dominated by the imaginary time propagator

$$G(\tau) = \frac{1}{N}\sum_i \langle \mathrm{T}_\tau\, \psi_i(\tau)\psi_i(0)\rangle\,. \tag{5.6}$$

It is the solution of the time-translation invariant equations of motion

$$\tilde{G}(\omega) = \left[-\mathrm{i}\omega - \tilde{\Sigma}(\omega)\right]^{-1}, \qquad \Sigma(\tau) = J^2 G(\tau)^{q-1}\,. \tag{5.7}$$

on the interval $[0,\beta]$ with anti-periodic boundary conditions. For clarity the first equation is expressed in frequency space. Equivalently, the saddle-point condition can be expressed a single integro-differential equation

$$\frac{\partial}{\partial\tau_1}G(\tau_1,\tau_2) - J^2\int \mathrm{d}\tau' G(\tau_1,\tau')G(\tau',\tau_2)^{q-1} = \delta(\tau_1-\tau_2)\,. \tag{5.8}$$

In the $\beta\to\infty$ limit, the equation can be approximated by neglecting the derivative term (equivalently, the ω term in Eq. 5.7). This leads to the emerging reparametrisation invariance for $\tau\to h(\tau)$

$$G(\tau_1,\tau_2) \to |\dot{h}(\tau_1)\dot{h}(\tau_2)|^{\frac{1}{q}} G(h(\tau_1),h(\tau_2)). \tag{5.9}$$

In the same limit, (5.8) is solved by

$$G(\tau) = \frac{b}{|\tau|^{\frac{2}{q}}}\,\mathrm{sign}(\tau)\,, \tag{5.10}$$

where b is a q-dependent positive constant [114]. The derivative term explicitly breaks the invariance, and the power law is cut off at $t\approx\beta$. The breaking of the symmetry is measured by the "cost" of the reparametrisation h, which leads to the Schwarzian action and the peculiar properties described in the previous section.

5.1.2 TAP approach

The Thouless–Anderson–Palmer (TAP) equations [120] provide an approach to study the glass transition, and more generally complex free-energy landscapes, based on expressing the free energy as a function of the set of order parameters that fully characterises the phases of the system. Here we briefly summarise the idea of the TAP approach. For a pedagogical introduction and further discussion see *e.g.* [34, 35, 121].

The basic idea of this approach is to generalise the construction of the mean-field the-

ory of the ferromagnetic transition. In the Curie–Weiss model, the Legendre transform of the free energy with respect to the magnetic field is a function of the magnetisation $f(m)$, whose minima represent the phases of the system: at high temperature there is a single minimum $m = 0$ (paramagnetic phase); the ferromagnetic transition is characterised by $f(m)$ developing two minima $m = \pm m^*$ (ferromagnetic phases).

TAP generalised this approach to the Sherrington–Kirkpatrick model by identifying the set of the order parameters to fix as *all* the local magnetisations $m_i = \langle s_i \rangle$. The TAP equations are obtained as the extremisation conditions on the TAP free energy. A solution is a set $\{m_i\}$ characterising a thermodynamic state of the system. At high temperature, only the paramagnetic solution $m_i = 0$ is present. Lowering the temperature, the appearance of $\mathcal{O}(e^N)$ solutions signals the dynamical transition T_d. While the resulting free energy is the same as that obtained by continuing the paramagnetic solution, the dynamics remains stuck in one of exponentially many minima of the free energy landscape [118]. At the static transition $T_s < T_d$ the number of solutions becomes sub-exponential, and the few solutions left represent the "ideal" glassy phase.

A different derivation of the TAP equations is given by the Plefka expansion [122]. This allows to compute the TAP free energy as a perturbative expansion in the interaction strength, which is exact at second order for mean-field models. The Plefka expansion was used to extend the TAP approach to quantum spin glasses by Biroli and Cugliandolo [121]. Here we apply the same method to derive the TAP free energy for the SYK model. We note that this approach is closely related to that of the self-consistent approximations derived in Section 4.4, which are also based on the potential obtained as a Legendre transformation of the free energy.

The Plefka expansion has been extended to the dynamic generating functional for classical stochastic dynamics [123, 124], where it was shown that the order parameters to constrain are the time-dependent single-site magnetisation, as well as the correlation functions. Similarly, quantum thermodynamics involves the study of imaginary-time dependent (Matsubara) quantities. Due to the Majorana nature of the SYK model, we constrain the following moments

$$m_i(\tau) = \mathrm{i}\,\langle \psi_{2i-1}(\tau)\psi_{2i}(\tau)\rangle\,, \qquad G(\tau_1,\tau_2) = \frac{1}{N}\sum_i \langle \psi_i(\tau_1)\psi_i(\tau_2)\rangle \ . \tag{5.11}$$

Note that there are only $N/2$ moments m_i, reflecting the dimension of the Hilbert space. The N Majorana Fermions in SYK can be mapped to $N/2$ Dirac Fermions, of which the m_i's are the occupation numbers.

We consider the free energy at fixed G and m_i's,

$$A[\beta, \mathbf{m}, G, \alpha] = -\beta F = \log \int \mathcal{D}\boldsymbol{\psi}\mathcal{D}\Sigma\mathcal{D}\mathbf{h} \exp \left[-S_0[\boldsymbol{\psi}] - \alpha \int_0^\beta \mathrm{d}\tau H_{\mathrm{SYK}}[\boldsymbol{\psi}] \right.$$
$$+ \frac{N}{2} \int_0^\beta \mathrm{d}\tau \mathrm{d}\tau' \Sigma(\tau, \tau') \left(G(\tau, \tau') - \frac{1}{N} \sum_i \psi_i(\tau)\psi_i(\tau') \right)$$
$$\left. + \int_0^\beta \mathrm{d}\tau \sum_{i=1}^{N/2} h_i(\tau) \left(m_i(\tau) - \mathrm{i}\psi_{2i-1}(\tau)\psi_{2i}(\tau) \right) \right] . \quad (5.12)$$

We introduced the parameter α, scaling the interaction strength, as a bookkeeping device for the Plefka expansion around the free theory $\alpha = 0$. The quantum TAP free energy corresponds to (5.12) at $\alpha = 1$. The expansion is

$$A[\beta, \mathbf{m}, G, \alpha] = \sum_{k=0}^{\infty} \frac{\alpha^k}{k!} \frac{\partial^k}{\partial \alpha^k} A[\beta, \mathbf{m}, G, \alpha]\big|_{\alpha=0} \quad (5.13)$$

The first term is the free theory, in which the Fermions can be integrated out,

$$A[\beta, \mathbf{m}, G, 0] = \log \int \mathcal{D}\Sigma\mathcal{D}\mathbf{h}\, \mathrm{e}^{\frac{N}{2}\mathrm{Tr}(\Sigma \cdot G) + \mathbf{h}\cdot\mathbf{m}} \exp \left[\frac{1}{2} \sum_{i=1}^{N/2} \ln \det \begin{pmatrix} \partial_\tau - \Sigma & -\frac{\mathrm{i}}{2} h_i(\tau) \\ \frac{\mathrm{i}}{2} h_i(\tau) & \partial_\tau - \Sigma \end{pmatrix} \right] . \quad (5.14)$$

We use a compact notation in which the τ, τ' dependence is treated as matrix indices. The determinant is both over this functional structure, and the 2x2 structure corresponding to the odd-even fermions that enter in the definition of the moments. Note that ∂_τ and the h_i's are diagonal in the time variables, while Σ is not.

The first order term is obtained with one insertion of the Hamiltonian

$$\partial_\alpha A[\beta, \mathbf{m}, G, 0] = -(\mathrm{i})^{\frac{q}{2}} \int_0^\beta \mathrm{d}\tau \sum_{i_1 < \cdots < i_q} J_{i_1 \ldots i_q} \langle \psi_{i_1} \ldots \psi_{i_q} \rangle_{\alpha=0}$$
$$= - \sum_{k_1 < \cdots < k_p}^{\frac{N}{2}} J_{2k_1-1, 2k_1 \ldots 2k_p-1, 2k_p} m_{k_1} \cdots m_{k_p} \approx \mathcal{O}(N^{1-q/2}) \quad (5.15)$$

where $p = q/2$. Only $\binom{N/2}{q/2} \propto N^{q/2}$ terms contribute to the sum, making this term vanish in the thermodynamic limit.

The second order term is

$$\frac{1}{2}\partial_\alpha^2 A[\beta,\mathbf{m},G,0] = \\ = \mathrm{i}^q \int_0^\beta \mathrm{d}\tau_1 \int_0^\beta \mathrm{d}\tau_2 \sum_{i_1<\cdots<i_q} \sum_{j_1<\cdots<j_q} J_{i_1\ldots i_q} J_{j_1\ldots j_q} \left\langle \psi_{i_1}\ldots\psi_{i_q}(\tau_1)\psi_{j_1}\ldots\psi_{j_q}(\tau_2)\right\rangle_{\alpha=0} \\ = N\frac{J^2}{q}\int_0^\beta \mathrm{d}\tau_1\mathrm{d}\tau_2 G(\tau_1,\tau_2)^q + \mathcal{O}(N^0)\ . \quad (5.16)$$

It is self-averaging with respect to the disorder. All contributions involving the moments m_i are subleading in N, for the same reason that makes the first order term (5.15) vanish in the thermodynamic limit. All higher orders in the expansion also vanish in the thermodynamic limit, as is the case for classical [122] and quantum [121] fully-connected models.

Summarising, we showed that the TAP free energy for the SYK model is that of the free Majorana Fermion theory (5.14), plus the simple correction (5.16). Its dependence on the moments m_i is trivial; in fact, the extremum condition for A with respect to m_i leads to $h_i(\tau)\equiv 0$. We can therefore neglect the dependence on the m_i's, obtaining

$$A[\beta,G,1] = \log\int \mathcal{D}\Sigma\, \mathrm{e}^{NS[G,\Sigma]} \quad (5.17)$$

where we recovered $S[G,\Sigma]$ from the annealed calculation (5.5). The Legendre relation for Σ and the extremum condition on A with respect to G give the equations (5.7,5.8). This shows that there is no glass transition at any temperature $T>0$, and the annealed calculation is correct.

5.2 From a classical spin glass to a quantum model

We start from a spherical p-spin model [125, 126] in which the degrees of freedom are N "soft spins" (real coordinates), with p-spin interactions and a soft spherical constraint imposed by a function $h(x)$ with a steep minimum at $x=1$,

$$V(q) = -\sum_{i_1<\cdots<i_p} J_{i_1\cdots i_p} q_{i1}\ldots q_{i_p} + Nh\left(\frac{1}{N}\sum_i q_i^2\right)\ , \quad (5.18)$$

where $J_{i_1\ldots i_p}$ are i.i.d. random variables drawn from a Gaussian distribution with zero mean and variance $\frac{J^2 p!}{2N^{p-1}}$.

We consider stochastic Langevin dynamics,

$$\dot{q}_i(t) = -\frac{\partial V}{\partial q_i} + \eta_i(t) \tag{5.19}$$

at temperature T_s, $\langle \eta_i(t)\eta_i(t')\rangle = 2T_s\delta(t-t')$. The evolution of the probability density is generated by the Fokker-Planck operator $H_{\rm FP}$,

$$\partial_t P_t(\mathbf{q}) = \sum_i \frac{\partial}{\partial q_i}\left[T_s\frac{\partial}{\partial q_i} + \frac{\partial V}{\partial q_i}\right] P_t(\mathbf{q}) \equiv -H_{\rm FP}P_t(\mathbf{q}). \tag{5.20}$$

The Fokker-Planck operator is not Hermitian, but detailed balance is satisfied with the Gibbs distribution. Taking its Hermitian form [67, 127, 128] and rescaling time, we define the operator

$$H = \frac{T_s}{2}\,\mathrm{e}^{V/2T_s}\,H_{\rm FP}\,\mathrm{e}^{-V/2T_s} = \sum_i\left[-\frac{T_s^2}{2}\frac{\partial^2}{\partial q_i^2} + \frac{1}{8}\left(\frac{\partial V}{\partial q_i}\right)^2 - \frac{T_s}{4}\frac{\partial^2 V}{\partial q_i^2}\right]. \tag{5.21}$$

H has the form of a Schrödinger operator with T_s playing the role of $\hbar$, and potential

$$V_{\rm eff} = \frac{1}{8}\sum_i\left[\sum_{i_2<\cdots<i_p} J_{i\,i_2\ldots i_p}q_{i_2}\cdots q_{i_p} - 2q_i h'(x)\right]^2 - \frac{T_s}{2}Nh'(x) - T_s x h''(x) \tag{5.22}$$

We neglect the last term which is subleading for large N. We take H as the Hamiltonian of a quantum system with N degrees of freedom and the spherical constraint $\sum_i \langle q_i^2\rangle = N$, which we enforce through the Lagrange multiplier $\lambda = 2h'$.

The spectrum of $H_{\rm FP}$ and that of H are the same, up to the rescaling in (5.21). From the theory of stochastic processes, we know that it is non-negative. Zero is an eigenvalue. Its right eigenvector is the equilibrium state of $H_{\rm FP}$. Correspondingly, the ground state of H has zero energy. At small T_s, stationary points of the original potential correspond to small values of the effective potential, with a correction proportional to T_s, which is negative for minima and positive for maxima.

The correspondence between the Fokker–Planck operator and a quantum Hamiltonian has been exploited in condensed matter physics (Rokhsar–Kivelson points [129]), stochastic quantisation and statistical physics [128, 130], and more specifically in the context of glassy physics [131–133].

We define our quantum mechanical model of interest by taking H as its Hamiltonian, with $\hbar = T_s$, and we study its equilibrium properties at temperature T_q. The partition

function is

$$Z(\beta_q) = \operatorname{Tr} \mathrm{e}^{-\beta_q H} = \operatorname{Tr} \mathrm{e}^{-\frac{1}{2}\beta_q T_s H_{\mathrm{FP}}} \ . \tag{5.23}$$

It can be represented as a Matsubara imaginary-time path integral. From the classical stochastic process perspective, the analogous construction is that of a Martin–Siggia–Rose–Janssen–De Dominicis (MSRJD) path integral [134–137], restricted to trajectories that return to the initial point after a time $t^* = \beta_q T_s/2$. Indeed such a construction was presented by Biroli and Kurchan [138], who showed that the resulting object $\mathcal{N}(t^*) = \operatorname{Tr} \mathrm{e}^{-t^* H_{\mathrm{FP}}} = Z(\beta_q)$ counts the number of states of the system that are stable up to a time t^* or longer.[1]

This establishes a correspondence between dynamical properties of the stochastic dynamics, and equilibrium properties of the quantum model. In the following we exploit this to study the low-temperature properties of the quantum model, for the simple case of $p = 2$, and within a harmonic approximation for $T_s \to 0$, $p > 2$. These represent the first steps toward investigating SYK-like physics from the perspective of classical glasses.

5.3 Linear dynamics ($p = 2$)

For $p = 2$, both the original (classical) and the modified (quantum) potentials are quadratic forms in the coordinates. The classical system undergoes linear stochastic dynamics, and there is no glassy phase. The corresponding quantum model is a set of harmonic oscillators, independent except for the spherical constraint. However the physics of the $p = 2$ model is not trivial, and it is worth investigating as both a solvable example of the classical-quantum mapping, and a starting point for the study of more complex models. Indeed, the $p = 2$ model has been thoroughly investigated over the years both at the classical and quantum levels [88, 140–142]. We stress that the quantum model considered here is not the same as that obtained by a conventional quantisation procedure.

5.3.1 Spherical constraint

For $p = 2$ (linear dynamics) the effective potential is expressed as the quadratic form

$$V_{\mathrm{eff}} = \frac{1}{2}(\mathbf{q}, A\mathbf{q}) - \frac{1}{4} N T_s \lambda, \qquad A = \frac{1}{4}(\mathbf{J} - \lambda \mathbb{I})^2 \ . \tag{5.24}$$

[1] Intuitively, the eigenstates of H_{FP} have a lifetime given by the inverse of the eigenvalue λ_i. The corresponding contribution $\mathrm{e}^{-t^* \lambda_i}$ is of order one for $t^* \lesssim 1/\lambda_i$, and exponentially small after that. A more precise description is given by the Gaveau–Schulman construction [138, 139].

The system is a collection of harmonic oscillators, corresponding to the eigenvectors of A, independent except for the spherical constraint $\sum_i \langle q_i^2 \rangle = N$, which fixes the Lagrange multiplier λ.

The oscillators have frequencies $\omega_\mu = |\mu - \lambda|/2$, where μ are the eigenvalues of $\mathbf{J}$. Up to subleading corrections, $\mathbf{J}$ is a GOE random matrix, so in the thermodynamic limit its spectral density is given by a Wigner semicircle of radius $R = J$

$$\rho(\mu) = \frac{2}{\pi R^2}\sqrt{R^2 - \mu^2}\,\theta(R - |\mu|)\ . \tag{5.25}$$

The partition function at temperature $T_q = \beta_q^{-1}$ is

$$Z = \prod_\mu \left(\frac{\mathrm{e}^{-\beta_q T_s \omega_\mu/2}}{1 - \mathrm{e}^{-\beta_q T_s \omega_\mu}}\right) \mathrm{e}^{N\beta_q T_s \lambda/4}\,. \tag{5.26}$$

Using $\langle q_\mu \rangle^2 = -\frac{1}{\beta_q \omega_\mu}\frac{\partial}{\partial \omega_\mu}\ln Z$, the spherical constraint reads

$$\sum_\mu \langle q_\mu^2 \rangle = \sum_\mu \frac{T_s}{2\omega_\mu} + \sum_\mu \frac{T_s}{\omega_\mu}\frac{\mathrm{e}^{-\beta_q T_s \omega_\mu}}{1 - \mathrm{e}^{-\beta_q T_s \omega_\mu}} \stackrel{!}{=} N\ . \tag{5.27}$$

We assume that no oscillator is macroscopically occupied, *i.e.* that the $\langle q_\mu^2 \rangle$'s do not diverge with N. Then in the thermodynamic limit the constraint can be expressed in terms of the integral

$$\frac{1}{T_s} = \int \mathrm{d}\mu \frac{\rho(\mu)}{|\lambda - \mu|} \coth\left(\beta_q T_s \frac{|\lambda - \mu|}{4}\right) \equiv F(\lambda) \tag{5.28}$$

Bose-Einstein condensation at $T_q = 0$

For $T_q = 0$ and $\lambda > R$, the integrand in (5.28) converges uniformly to that of the resolvent of the semicircle distribution,

$$F(\lambda) = G(\lambda) = \frac{2}{R^2}\left(\lambda - \sqrt{\lambda^2 - R^2}\right). \tag{5.29}$$

$G(\lambda)$ is a continuous function on $(R, +\infty)$, monotonically decreasing from $G(R) = 2/R$ to zero. Therefore for $T_s > T_c = R/2$, eq. (5.28) has a unique solution

$$\lambda_0 = \frac{R^2 + 4T_s^2}{4T_s} = \frac{T_c^2 + T_s^2}{T_s} > R. \tag{5.30}$$

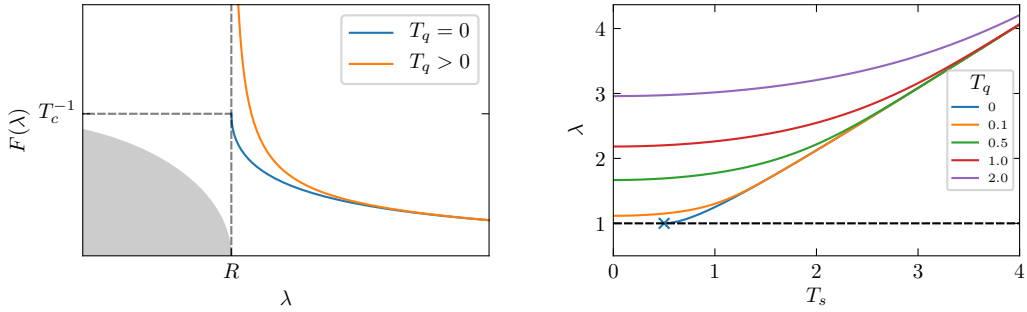

Figure 5.1: Fixing the Lagrange multiplier λ to satisfy the spherical constraint, graphical solution of (5.28). Left: if $T_q > 0$, there is a unique solution $\lambda > R$ for any T_s. At $T_q = 0$, a solution is found only for $T_s > T_c$, signalling Bose-Einstein condensation. Right: example of numerical solutions (R=1).

The spectrum of A is positive, with a gap $\lambda_0 - R$. Decreasing T_s, λ_0 approaches the edge of the semicircle at T_c, and (5.28) has no solution (see Fig. 5.1). The spherical constraint cannot be satisfied. This is due to the appearance of a zero mode in A, which is macroscopically occupied. This is the same mechanism that leads to Bose-Einstein condensation, although the constraint is different. To treat this, we account for a $\mathcal{O}(N)$ amplitude

$$\langle q_0^2 \rangle = \frac{T_s}{\lambda - R} \equiv Nq \tag{5.31}$$

and re-write the spherical constraint as

$$N \stackrel{!}{=} Nq + \sum_{\mu \neq 0} \frac{T_s}{2\omega_\mu} \xrightarrow{N\to\infty} N[q + T_s G(\lambda)]. \tag{5.32}$$

For $T_s > T_c$, $q = 0$ (back to previous case). For $T_s < T_c$, λ is "stuck" to R and there is a non-trivial solution

$$q = 1 - \frac{T_s}{T_c} \ . \tag{5.33}$$

Note that with the usual conventions $T_c = R/2 = J/2$, so this condensation is a quantum phase transition that takes place at strong coupling, $J > 2T_s$.

Finite T_q

With the zero-temperature picture in mind, we look at the spherical constraint for $T_q > 0$. The integrand in (5.28) is continuous with continuous derivatives, so F is differentiable on (R, ∞). Note that $F'(\lambda) < 0$, and F diverges at the edge of the semicircle. Therefore F is a bijection between (R, ∞) and $(0, \infty)$, and there is a

unique solution $\lambda > R$ for any T_s, see Fig. 5.1 (left). This shows that for arbitrary small $T_q > 0$, the spectrum is gapped, and condensation is destroyed. In the following we are interested in the behaviour of the gap $z = \lambda - R$ for $T_q \to 0$. If $T_s > T_c$, the limit is finite and given by $\lambda_0 - R$ (5.30). If $T_s \leq T_c$, $z \to 0$.

To analyse the scaling of z approaching the condensate phase, it is useful to rewrite the integral in (5.28) as

$$F(\lambda) = \int \mathrm{d}\mu \frac{\rho(\mu)}{|\lambda - \mu|} + \int \mathrm{d}\mu \frac{2\rho(\mu)}{|\lambda - \mu|} \frac{\mathrm{e}^{-\beta_q T_s |\lambda - \mu|/2}}{1 - \mathrm{e}^{-\beta_q T_s |\lambda - \mu|/2}} \tag{5.34}$$

If $T_s < T_c$, the first integral in (5.34) gives a finite contribution T_c^{-1}, with corrections of order $\sqrt{z}$. The scaling of z is obtained by requiring the integral in

$$2 \int_0^{2R} \mathrm{d}x \frac{\rho(R - x)}{z + x} \frac{1}{\mathrm{e}^{\beta_q T_s (z+x)/2} - 1} = T_s^{-1} - T_c^{-1} \tag{5.35}$$

to be of order one. In particular we need to handle the behaviour at $x \approx 0$. With a change of variables $x' = x/z$, ignoring constant factors and with $c = \beta_q z T_s/2$, the integral becomes

$$\begin{aligned} &\frac{2}{\pi} \sqrt{2z} R^{-\frac{3}{2}} \int_0^{+\infty} \mathrm{d}x \frac{\sqrt{x}}{(1+x)\left[\mathrm{e}^{c(1+x)} - 1\right]} \\ &\qquad \approx \frac{2\sqrt{2}}{\pi R^{\frac{3}{2}}} \frac{2T_q}{T_s \sqrt{z}} \int_0^{+\infty} \mathrm{d}x \frac{\sqrt{x}}{(1+x)^2} = \frac{2\sqrt{2}}{R^{\frac{3}{2}}} \frac{T_q}{T_s} z^{-\frac{1}{2}} \,. \end{aligned} \tag{5.36}$$

Since $T_q / z^{1/2}$ must be of order one, we find the scaling $z \propto T_q^2$. In the first passage we assumed that $c \to 0$, *i.e.* that z vanishes faster than T_q. If this were not the case, the expression would be at most of order $T_q^{1/2}$.

At the transition $T_s = T_c$, the finite contribution from the first integral satisfies the constraint. The scaling is determined by

$$\int_0^{2R} \mathrm{d}x \frac{\rho(R - x)}{z + x} \frac{1}{\mathrm{e}^{\beta_q T_s (z+x)/2} - 1} = T_c^{-1} - G(R + z) = \left(\frac{2}{R}\right)^{\frac{3}{2}} \sqrt{z} + \mathcal{O}(z) \tag{5.37}$$

so the integral must give a contribution of order $\sqrt{z}$. From (5.36), we see that this is indeed the case if c has a finite value in the $T_q \to 0$ limit. This implies that $z \propto T_q$.

Solving the constraint equation (5.28) numerically confirms the scaling both below and at the transition, see Fig. 5.2 (left).

5.3.2 Energy and specific heat

Having determined the scaling of the Lagrange multiplier, we can compute low-temperature properties of the model by summing over the harmonic oscillator results. The energy density is given by

$$\varepsilon = \frac{E}{N} = -\frac{1}{N}\frac{\partial}{\partial \beta_q} \log Z = \frac{T_s}{N} \sum_\mu \left[\frac{\omega_\mu}{2} + \frac{\omega_\mu e^{-\beta_q T_s \omega_\mu}}{1 - e^{-\beta_q T_s \omega_\mu}} \right] - \frac{T_s \lambda}{4} \tag{5.38}$$

In the thermodynamic limit we obtain

$$\varepsilon = \frac{T_s}{2} \int \mathrm{d}\rho(\mu) \frac{\lambda - \mu}{\mathrm{e}^{\beta_q T_s (\lambda - \mu)/2} - 1} = \frac{T_s}{\pi R^2} z^{\frac{5}{2}} \int_0^{2R/z} \mathrm{d}x \sqrt{x(2R - zx)} \frac{1 + x}{\mathrm{e}^{c(1+x)} - 1} \ . \tag{5.39}$$

- Below the transition $T_s < T_c$, with the change of variable $y = c(1 + x)$ the integral becomes

$$c^{-\frac{5}{2}} \int_c^{c(1+R/z)} \mathrm{d}y y^{\frac{3}{2}} \frac{\sqrt{2R - \frac{z}{c} y}}{\mathrm{e}^y - 1} \propto c^{-\frac{5}{2}} \int_0^\infty \mathrm{d}y \frac{y^{3/2}}{\mathrm{e}^y - 1} = c^{-\frac{5}{2}} \frac{3}{4} \sqrt{\pi} \zeta\left(\frac{5}{2}\right) \tag{5.40}$$

  Therefore the energy scales as $(z/c)^{\frac{5}{2}} = T_q^{\frac{5}{2}}$. The specific heath scales as $T_q^{\frac{3}{2}}$.

- At the transition $T_s = T_c$, c is finite and the integral in (5.39) is of order one. The prefactor is $\propto z^{\frac{5}{2}}$ and z is linear in T_q, so $\varepsilon \sim T_q^{\frac{5}{2}}$ and the specific heath scales as $T_q^{\frac{3}{2}}$. The scaling is the same below and at the transition, and is confirmed numerically (Fig. 5.2, right).

- Above the transition $z \to z_0 > 0$, and the integrand in (5.39) is bounded uniformly by the exponentially large denominator. The specific heat vanishes exponentially $\propto \mathrm{e}^{-c}$.

5.3.3 Dynamics

We study the real-time dynamics of the model at equilibrium at temperature T_q. The main quantities of interest are two-time correlation functions. We focus on the correlator

$$C(t) = \frac{1}{2N} \sum_i \langle \{q_i(t), q_i\} \rangle = \frac{1}{N} \sum_\mu \langle q_\mu^2 \rangle \cos(\omega_\mu t) \tag{5.41}$$

where the expectation values are computed in the thermal state of the harmonic oscillators and $\{,\}$ is the anticommutator.

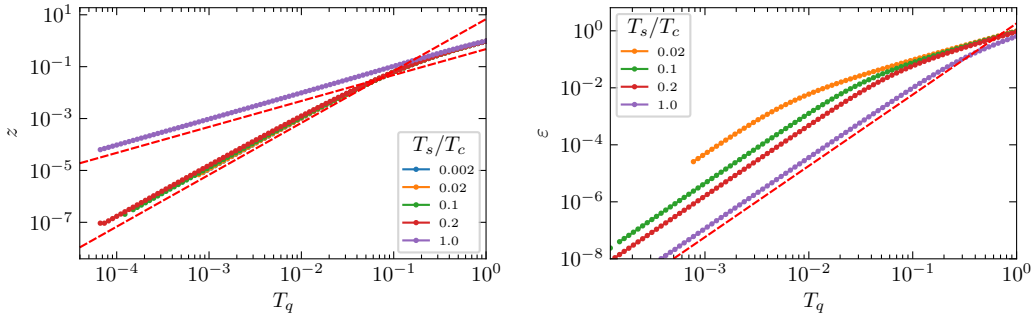

Figure 5.2: Numerical check of the low-temperature scaling for the gap z (left) and the energy density ε (right). The slopes of the dashed lines are the predictions for the $T_q \to 0$ scaling exponent.

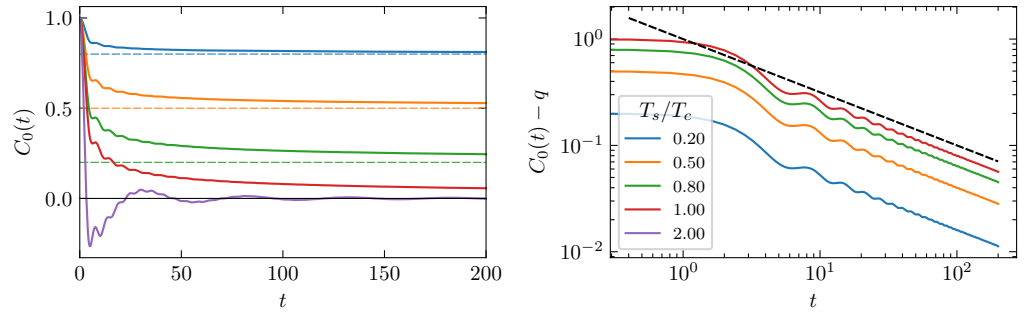

Figure 5.3: Correlation functions at $T_q = 0$ in the $p = 2$ model (5.45), for some values of T_s (legend on the right). Left: the correlation functions approach the plateau (dashed lines) for $T_s < T_c$, and zero for $T_s \geq T_c$. Right: scaling above the plateau for $T_s \leq T_c$, showing the $t^{-1/2}$ power law (black dashed line).

However, the equilibrium dynamics is time-translation invariant. Therefore all two-time functions only depend on the difference between time as in (5.41), and the Lagrange multiplier is a constant, enforcing the constraint $C(0) = 1$.

$T_q = 0$

Taking into account the macroscopically occupied zero-mode, in the thermodynamic limit the correlator has the integral representation

$$C(t) = \frac{1}{N}\langle q_0^2\rangle + T_s \int \mathrm{d}\mu \rho(\mu) \langle q_\mu^2\rangle \cos(\omega_\mu t) = q + T_s \int \mathrm{d}\mu \frac{\rho(\mu)}{\lambda - \mu} \cos\left(\frac{\lambda - \mu}{2} t\right) \quad (5.42)$$

- Above the transition ($T_s > T_c$) there is no condensation, $q = 0$ and the integral is

the Fourier transform of a continuous function with compact, positive support. It is smooth, except for the square-root kink at the edge, leading to a power law with oscillations controlled by the smallest frequency

$$C(t) \approx \frac{\cos(\omega_{\min} t)}{t^{3/2}}, \quad \omega_{\min} = \frac{z}{2} = \frac{1}{2T_s}(T_s - T_c)^2 \ . \tag{5.43}$$

- Approaching the transition, $z \to 0$. The integrand in (5.42) has a $1/\sqrt{R-\mu}$ singularity at the edge of the semicircle, which gives the asymptotic behaviour

$$C(t) = q + \frac{b}{t^{\frac{1}{2}}} \ . \tag{5.44}$$

  The power law decay is the same at and below the transition $T_s \leq T_c$. See Fig. 5.3.

$T_q > 0$

At finite T_q there is no condensation, and we write

$$C(t) = C_0(t) + 2T_s \int_0^{2R} \mathrm{d}x \frac{\rho(R-x)}{z+x} \frac{\cos\left(\frac{z+x}{2}t\right)}{\mathrm{e}^{\beta_q T_s (z+x)/2} - 1} \equiv C_0(t) + C_1(t) \tag{5.45}$$

with the decaying part of the $T_q = 0$ correlator $C_0(t) = (C(t) - q)|_{T_q=0}$ from eq (5.42).

- For $T_s > T_c$, the same argument as for $T_q = 0$ applies. The asymptotic behaviour is the same.

- For $T_s < T_c$, note by comparing equations (5.35,5.45) that $C_1(0) = q$. With the change of variable $x' = x/z$, at low T_q

$$C_1(t) \approx 2T_s \frac{\sqrt{z}}{c} \int_0^{\infty} \mathrm{d}x \frac{\rho(R - zx)}{(1+x)^2} \cos\left(\frac{1+x}{2} zt\right) \ . \tag{5.46}$$

  Since $\sqrt{z} \sim c \sim T_q$, the integral is of order one. Taking the $T_q \to 0$ at fixed time $t \sim \mathcal{O}(1)$, the time dependence disappears, and $C_1(t) = C_1(0) + \mathcal{O}(T_q^2) \approx q$. The timescale at which correlations decay is determined by $zt \sim \mathcal{O}(1)$, $t \propto \beta_q^2$.

  There is an intermediate regime $1 \ll t \ll \beta_q^2$ in which the system approaches the constant value q, with a $t^{-\frac{1}{2}}$ power-law decay (given by C_0). At $t \propto \beta_q^2$ the correlator decays from the plateau to zero.

	$T_s < T_c$	$T_s = T_c$	$T_s > T_c$
q	$1 - T_s/T_c$	0	0
z	T_q^2	T_q	$(T_s - T_c)^2/T_s$
specific heat	$T_q^{3/2}$	$T_q^{3/2}$	$\mathrm{e}^{-\beta_q T_s z/2}$
dynamics	Plateau $q + \frac{b}{t^{\frac{1}{2}}}$ for $1 \ll t \ll \beta_q^2$	$\frac{b}{t^{\frac{1}{2}}}$ for $1 \ll t \ll \beta_q$	$\mathrm{e}^{-\mathrm{i}zt/2}/t^{3/2}$

Table 5.1: Summary of results for $p = 2$.

- At the transition $T_s = T_c$ the situation is similar to $T_s < T_c$, but there is no plateau ($q = 0$), and the different scaling of z implies that the timescale at which the power law is cut off is $t \propto \beta_q$.

The results derived for $p = 2$ are summarised in Table 5.1.

5.4 Glassy model ($p > 2$)

For $p > 2$ the dynamics of the spherical p-spin model is not linear, and the model is a paradigmatic example of the thermodynamic approach to glassy physics. Unsurprisingly the analysis for $p > 2$ is significantly more complicated than for $p = 2$. As a first step, here we analyse the model in the $T_s \to 0$ limit, using a harmonic approximation. Some limitations of this approach are discussed in the following sections.

5.4.1 Low-temperature limit at fixed $\beta\hbar$

We first consider the combined limit $T_s \to 0$, $T_q \to 0$ at fixed $t^* = T_s/(2T_q)$, and analyse the scaling with $t^* \to \infty$. This provides a first approximation, but is different from the $T_q \to 0$ limit at fixed T_s. From the point of view of the classical model, it allows to study the long-time zero-temperature dynamics, and was considered in [138]. In the quantum model, the meaning of this limit is less clear. In the next section we expand the result of this analysis to consider a more natural limit, see Fig. 5.5.

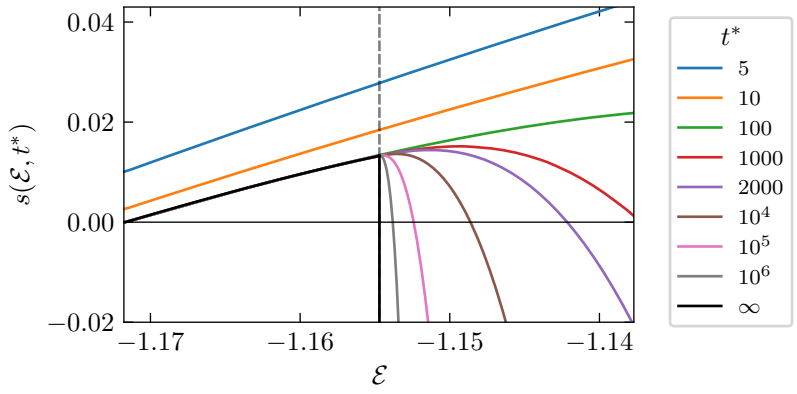

Figure 5.4: Time dependent, energy-resolved configurational entropy at $T_s \to 0$ for $p = 3$, reproducing Fig. 4 of [138].

Entropy of long-lived states at $T_s = 0$

At $T_s \to 0$ the entropy density of states of energy $\mathcal{E}$ stable up to t^* is given by [138]

$$s(\mathcal{E}, t^*) = \frac{1}{2}\left(1 + \ln\frac{p}{2}\right) - \mathcal{E}^2 + \mathrm{Re}\left[\frac{1}{2}\left(\frac{\mathcal{E} \mp \sqrt{\mathcal{E}^2 - \mathcal{E}_c^2}}{\mathcal{E}_c}\right)^2 + \log\left(-\mathcal{E} \mp \sqrt{\mathcal{E}^2 - \mathcal{E}_c^2}\right)\right] + \\ - \int \mathrm{d}\omega \rho_p(\omega + p\mathcal{E}) \ln\left[1 - \mathrm{e}^{-t^*|\omega|}\right] + t^* \int_{-\infty}^{0} \mathrm{d}\omega \rho_p(\omega + p\mathcal{E})\omega \quad (5.47)$$

The integrals involve ρ_p, the semicircle density of radius $R = \sqrt{2p(p-1)}$, centred at $-p\mathcal{E} > 0$.

The first line of (5.47) does not depend on t^* and counts the number of saddles (stationary points in the energy landscape) at energy density $\mathcal{E}$. The second line is a sum of harmonic contributions, and the density of states ρ_p coincides with the spectrum of the Hessian computed at saddles of energy density $\mathcal{E}$ [143]. It is interpreted as a harmonic expansion around the saddles.[2] As we show below, if ρ_p has positive support, the contribution from the second line is vanishingly small at large t^*; otherwise, it gives an increasingly negative contribution, a penalty for expanding around unstable saddles. The energy at which the edge of the semicircle touches zero is the threshold $\mathcal{E}_c = -\sqrt{2(p-1)/p}$. In Fig. 5.4 we show the configurational entropy (5.47) as a function of $\mathcal{E}$, for increasing values of t^*.

To recover the partition function of the quantum model, we are interested in the

[2] The expansion becomes exact at $T_s \to 0$ [128, 138]. This is the idea behind the harmonic approximation presented in the next section.

total number of metastable states at t^*, regardless of energy. In terms of entropy, this is controlled for each t^* by the maximum over $\mathcal{E}$ of (5.47).

Increasing $\mathcal{E}$ at fixed t^*, there is a competition between the two terms: the total number of saddles increases, while ρ_p shifts towards negative values, making the contribution from the integrals more negative. In the $t^* \to \infty$ limit the number of stable states is recovered (black line in Fig. 5.4), in agreement with the TAP calculation [126], and the maximum is at the threshold $\mathcal{E}_c$, with configurational entropy $s_0 = s(\mathcal{E}_c, \infty)$. For finite t^*, there is a unique maximum $\mathcal{E}_M(t^*)$, which approaches the threshold from above.

We are interested in the scaling of $\mathcal{E}_M(t^*) - \mathcal{E}_c$ and of $s_M(t^*) - s_0$ with t^*. To find it, we consider (5.47) in the double scaling limit $t^* \to \infty$, $\mathcal{E} \to \mathcal{E}_c$ with $\mathcal{E} - \mathcal{E}_c = At^{-\alpha}$ for some fixed α. We then determine the exponent α by comparing the competing contributions in (5.47). The calculation is performed in Appendix 5.A. We find the exponent $\alpha = 2/3$ independent on p, and

$$s_M(t^*) = s\left(\mathcal{E}_M(t^*), t^*\right) = s_0 + c_M t^{*-\frac{2}{3}} + \mathcal{O}\left(t^{*-\frac{4}{3}}\right) \tag{5.48}$$

with a p-dependent constant $c_M > 0$, computed in the Appendix, Eq. 5.79.

Back to the quantum model

Using the correspondence between the number of metastable states in the classical model and the partition function of the quantum model, we derive from (5.48) the free energy of the latter at $T_q \to 0$

$$-\beta_q f = \frac{1}{N} \log \mathcal{N}\left(t^* = \frac{T_s}{2T_q}\right) = s_0 + 2^{-2/3} c_M \left(\beta_q T_s\right)^{-2/3} \ . \tag{5.49}$$

This shows that the model has finite entropy s_0 at zero temperature. Like in SYK, this is not due to degeneracy (the ground state is unique for any finite N), but to the "accumulation" of an exponential number of stable states at the threshold. From (5.49) we also derive the scaling of the energy density $\propto T_q^{5/3}$ and specific heat

$$\text{specific heat} \approx \frac{10}{9} c_M \left(\frac{T_q}{2T_s}\right)^{2/3} \ . \tag{5.50}$$

We note that while these results are obtained in a peculiar limit, the fact that the zero-temperature entropy is given by the number of stable states is a direct consequence of the correspondence between the models, valid exactly at finite T_s.

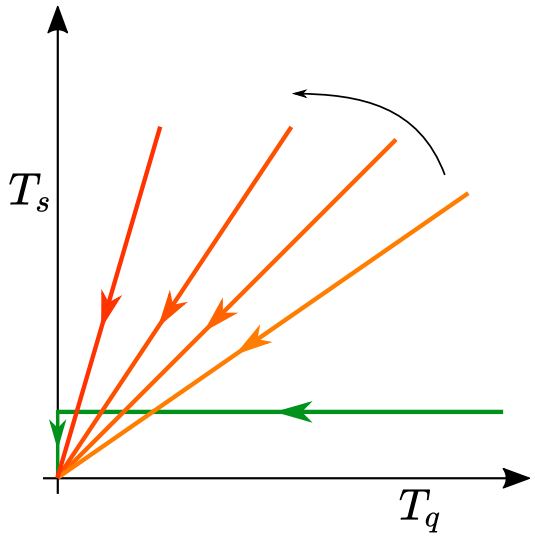

Figure 5.5: The two low-temperature limits represented in the T_q-T_s plane. The analysis of the classical model at $T_s = 0$ (section 5.4.1) corresponds to the unusual scaling represented by orange-to-red lines (fixed T_s/T_q). The harmonic approximation (section 5.4.2) analyses the $T_q \to 0$ scaling at fixed, small T_s (green line).

The analysis of states with long lifetimes in the classical model corresponds to the thermodynamical analysis of the quantum model at low-temperature. Due to the rescaling in (5.21), the quantum partition function at T_q corresponds to the trace of the stochastic evolution operator at $t^* = \beta\hbar/2$.

5.4.2 Harmonic approximation

We now consider the low-T_q scaling at fixed, small T_s, using the harmonic expansion mentioned in the previous section. This corresponds to taking the $T_s \to 0$ limit after the $T_q \to 0$ one, which is related but subtly different from the limit considered previously (see Fig. 5.5). The harmonic expansion consists in expanding the potential around each stationary point, approximating the degrees of freedom as harmonic oscillators, with frequencies given by the spectrum of the Hessian. This includes unstable directions, whose effect is taken into account in the resulting spectrum. The expansion is presented and discussed in Chapter 3 of [128]. As $T_s \to 0$, the expansion becomes exact and the result (5.47) is recovered, while for small $T_s > 0$ it gives an approximation.

To count the number of states at fixed energy density $\mathcal{E}$ in the harmonic approximation, we consider following [138] the MSRJD path integral over closed trajectories of

period t^*. The spherical and energy constraints are enforced by Lagrange multipliers $\hat{\lambda}$ and λ, and the eigenvalues μ of the Hessian are distributed according to the semicircle distribution ρ_p of radius $R = \sqrt{2p(p-1)}$ [143], as in (5.47). This results in

$$\mathcal{N}(\mathcal{E}, t^*) = \int \mathcal{D}\mathbf{q}\mathcal{D}\hat{\mathbf{q}}\, \mathrm{e}^{-\frac{\hat{\lambda}}{2}\int(\sum_\mu q_\mu^2 - 1) - \int \sum_\mu \hat{q}_\mu[\dot{q}_\mu - (\lambda-\mu)q_\mu - T_s\hat{q}_\mu]} \tag{5.51}$$

$$= \mathrm{e}^{\frac{\hat{\lambda}\beta_q T_s}{4}} \int \mathcal{D}\mathbf{q}\, \mathrm{e}^{-\frac{\hat{\lambda}}{2}\int\sum_\mu q_\mu^2 - \frac{1}{4T_s}\int\sum_\mu[\dot{q}_\mu - (\lambda-\mu)q_\mu]^2} \tag{5.52}$$

All integrals are over (imaginary) time with periodic boundary conditions. The spectrum of the Fokker-Planck operator is that of the quantum Hamiltonian of harmonic oscillators, the frequencies ω_μ of which can be read off (5.52), leading to the energies and partition function

$$E_n^{(\mu)}[\lambda, \hat{\lambda}] = \frac{T_s}{2} \underbrace{\sqrt{2\hat{\lambda}T_s + (\lambda-\mu)^2}}_{2\omega_\mu} \left(n + \frac{1}{2}\right) - \frac{T_s}{4}(\lambda - \mu) \tag{5.53}$$

$$\mathrm{e}^{-\frac{\hat{\lambda}t^*}{2}} Z^{(\mu)}[\lambda, \hat{\lambda}] = \frac{\mathrm{e}^{-\frac{\beta_q T_s}{4}[\sqrt{2\hat{\lambda}T_s + (\lambda-\mu)^2} - (\lambda-\mu)]}}{1 - \mathrm{e}^{-\frac{\beta_q T_s}{2}\sqrt{2\hat{\lambda}T_s + (\lambda-\mu)^2}}} = \frac{\mathrm{e}^{-t^*[\omega_\mu - (\lambda-\mu)/2]}}{1 - \mathrm{e}^{-2t^*\omega_\mu}} \tag{5.54}$$

The number of metastable states at fixed classical energy $\mathcal{E}$ is obtained by counting the total number of states, weighted with the above partition function integrated over all modes μ. Maximising over λ fixes $\lambda = -p\mathcal{E} + \mathcal{O}(T_s)$ [138], while $\hat{\lambda}$ enforces the spherical constraint. The full quantum partition function is obtained by maximising over the energy as well,

$$\ln Z = \max_{\mathcal{E}, \hat{\lambda}} \left\{ I_0(\mathcal{E}) - \int \mathrm{d}\rho(\mu) \left[\ln\left(1 - \mathrm{e}^{-2t^*\omega_\mu}\right) + t^* \left(\omega_\mu - \frac{\lambda - \mu}{2}\right)\right] + \frac{\hat{\lambda}t^*}{2} \right\}, \tag{5.55}$$

where $I_0(\mathcal{E})$ is the total number of saddle of energy density $\mathcal{E}$ (5.65). Setting $T_s \to 0$ at fixed t^*, we recover (5.47). The harmonic approximation becomes exact in this limit.

The extremum condition of (5.55) with respect to $\hat{\lambda}$ gives

$$\int \mathrm{d}\mu \frac{\rho(\mu)}{2\omega_\mu} \coth\left(\frac{\beta_q T_s}{2}\omega_\mu\right) = \frac{1}{T_s}\,. \tag{5.56}$$

This has the same form as (5.34), the spherical constraint for harmonic oscillators with frequencies $4\omega_\mu^2 = 2\hat{\lambda}T_s + (\lambda - \mu)^2$. The difference between the $p = 2$ and $p > 2$ cases is in the presence of $\hat{\lambda}$, which changes the density of states. For $T_q = 0$, $\hat{\lambda} \to 0$ and the discussion of Bose-Einstein condensation is essentially unchanged from the $p = 2$

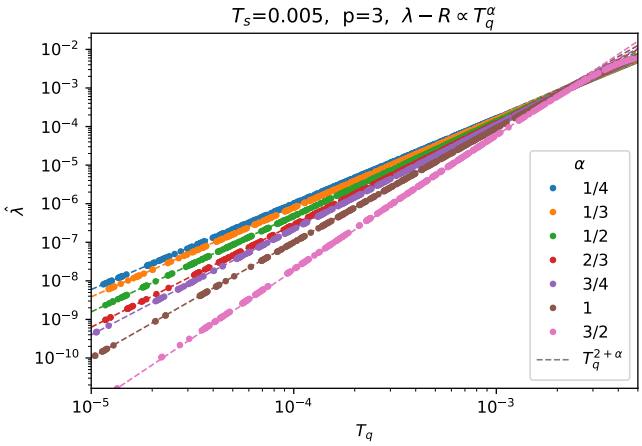

Figure 5.6: Scaling of $\hat{\lambda}$ at $T_q \to 0$, with small $T_s > 0$ (harmonic approximation). From the numerical solution of (5.56) with $\lambda - R \propto T_q^\alpha$. For each α, the dashed line shows the T_q^β, $\beta = \alpha + 2$ scaling.

case. Note that we are working at small T_s, deep in the condensed phase.

We want again to maximise (5.55), finding the scaling of the maximum above the threshold with $T_q \to 0$. We adopt the same strategy as in the previous section, considering $\mathcal{E} - \mathcal{E}_c = \bar{A} T_q^\alpha$ for some $\bar{A}$ and α to be determined, which fixes $\lambda = R - p\bar{A} T_q^\alpha$. Allowing for the additional scaling $\hat{\lambda} = \frac{\hat{\ell}}{2T_s} T_q^\beta$, we find that the spherical constraint implies $\beta = 2 + \alpha$, see Fig. 5.6.

We show in Appendix 5.A that in the scaling limit ($T_q \to 0$, $\mathcal{E} - \mathcal{E}_c = \bar{A} T_q^\alpha$, $\hat{\lambda} \propto T_q^{2+\alpha}$) the corrections in the harmonic approximation (5.55) with respect to the $T_s = 0$ result (5.47) are all subleading. Therefore, we find again $\alpha = 2/3$, and the entropy, free energy and specific heat (5.49,5.50) are unchanged.

5.4.3 Density of states and correlation function

In the MSRJD construction, the path integral is performed over two sets of fields $\mathbf{q}, \hat{\mathbf{q}}$. After averaging over the disorder, the fields can be integrated out and the action is

expressed in terms of the correlation functions

$$\begin{aligned} C(t,t') &= \frac{1}{N}\sum_i \langle q_i(t) q_i(t')\rangle\,, \\ R(t,t') &= \frac{1}{N}\sum_i \langle q_i(t) \hat{q}_i(t')\rangle\,, \\ D(t,t') &= \frac{1}{N}\sum_i \langle \hat{q}_i(t) \hat{q}_i(t')\rangle\,. \end{aligned} \tag{5.57}$$

This is the same procedure presented above for SYK, leading to (5.5). The saddle point of $S[C,R,D]$ gives a set of integro-differential equations of motion for the correlation functions [138]. In the standard construction, C is the autocorrelation function, R is a causal response function, and D vanishes due to causality. The causal structure is in general lost in the Biroli–Kurchan construction due to periodicity in time $t \in [0, t^*]$.

The saddle point equations have an emergent time reparametrisation invariance $t \to h(t)$

$$C(t,t') \to C(h(t),h(t'))\,. \tag{5.58}$$

$$R(t,t') \to \dot{h}(t') R(h(t),h(t'))\,. \tag{5.59}$$

$$D(t,t') \to \dot{h}(t)\dot{h}(t') D(h(t),h(t'))\,. \tag{5.60}$$

The first two relations are directly inherited from the study of dynamics in the ageing regime [119], while the latter is specific to the Biroli–Kurchan analysis. This will be discussed in a forthcoming publication [2]. The symmetry is explicitly broken by terms that vanish at $T_q \to 0$ (*i.e.* long times in the classical dynamics).

Although technically more involved, this is very similar to SYK both in the spirit of the derivation (5.3-5.8), and the resulting emergent symmetry (5.9). Equations (5.58-5.60) are compatible with assigning to the fields $\mathbf{q}$ and $\hat{\mathbf{q}}$ scaling dimensions 0 and 1 respectively, independently of p, to compare to the dimension $1/q$ of $\boldsymbol{\psi}$ in SYK.

The classical-quantum (MSRJD-Matsubara) correspondence is not limited to the partition function, but extends to averages of observables [138]. However in general the change of basis (5.21) is not as innocuous. Momenta in the Matsubara path integral are related to the auxiliary fields $\hat{\mathbf{q}}$, but the corresponding correlation functions acquire extra terms involving derivatives of the potential, which differ for different kind of correlation functions [127]. We also stress that (5.57) correspond to imaginary-time correlation functions, from which the real-time ones can be obtained by a careful analytic continuation [144].

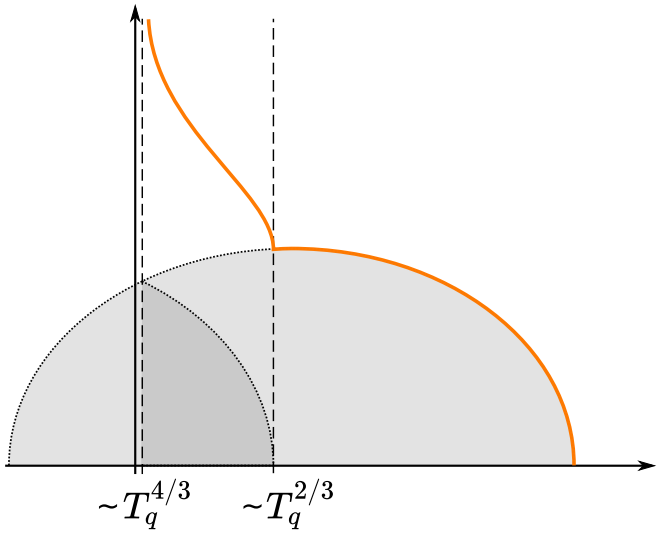

Figure 5.7: Sketch of the density of states (5.62) for $p > 2$, $T_s > 0$ within the harmonic approximation (distribution of ω, orange line) compared to the $T_s = 0$ semicircle (distribution of $(\lambda - \mu)/2$).

Within the harmonic approximation, it is simpler to work directly on the quantum side, calculating correlation functions in terms of harmonic oscillators, as for $p = 2$ (5.45). Real-time correlation functions are obtained as Fourier integrals involving the density of states, *e.g.*

$$C(t) = \frac{1}{N}\sum_i \langle\{q_i(t), q_i\}\rangle = \int \mathrm{d}\omega \frac{\rho(\omega)}{2\omega} \coth\left(\frac{\beta_q T_s}{2}\omega\right)\cos(\omega t). \tag{5.61}$$

and similar expressions hold for other Green functions. The density of states is given by

$$\rho(\omega) = \int \mathrm{d}\rho_p(\mu)\delta\left(\omega - \sqrt{\frac{1}{2}\hat{\lambda}T_s + \frac{1}{4}(\lambda-\mu)^2}\right) . \tag{5.62}$$

At $T_q = 0$, $\lambda = R$ and $\hat{\lambda} = 0$, and the discussion for $p = 2$ is essentially unchanged. The critical temperature T_c is rescaled and p-dependent; since we are working at small T_s, we are deep in the condensed phase, and $q = 1 - T_s/T_c$ is close to one.

At $T_q > 0$, given the semicircle-distributed spectrum for μ, the change of variables leads to the deformation sketched in Fig. 5.7. There are two relevant scales, both vanishing in the $T_q \to 0$ limit: $z = (R-\lambda)/2 \approx T_q^{2/3}$ and $\omega_{\min} = \sqrt{\hat{\lambda}T_s/2} \approx T_q^{4/3} \ll z$. For $\omega \geq z$, there is a one-to-one correspondence between ω and μ, and the distribution $\rho(\omega)$ is very close to the semicircle centred in λ for $\omega \geq z$. Below that, each value

of ω is obtained from two different μ's: the edge of the semicircle is "folded back" to positive values, giving a square-root kink at $\omega = z$. Finally, $\omega_{\min}$ acts as a cut-off.

Up to timescales $t \lesssim z^{-1} \approx T_q^{-2/3}$, the system does not resolve the difference between the two densities of states, and the correlation function has the same power law behaviour above the plateau. Additionally, due to the kink in ρ at $\omega = z$, there are power-law decaying oscillations $\propto \frac{1}{t^2}\cos(zt)$ around the plateau. The gap $\omega_{\min}$ sets the longest timescale, $\propto T_q^{-4/3}$, at which the correlation function decays exponentially.

5.4.4 Out-of-time-order correlators

A particular four-point correlation function, called the out-of-time-order correlator (OTOC) is commonly used to detect quantum chaos by defining quantum Lyapunov exponents [115, 116, 145]. It is defined for two observables A, B of a system in equilibrium at temperature $T = 1/\beta$ as

$$C_{AB}(t) = -\frac{1}{Z}\operatorname{Tr}\left(\mathrm{e}^{-\frac{\beta}{2}H}[A(t), B]\,\mathrm{e}^{-\frac{\beta}{2}H}[A(t), B]\right) . \tag{5.63}$$

In chaotic systems it has an exponential regime $\propto \mathrm{e}^{\lambda t}$, with a quantum Lyapunov exponent satisfying the bound

$$\lambda \leq \frac{2\pi T}{\hbar} . \tag{5.64}$$

The bound was originally proposed in the context of string theory [114], but it is a generic property of quantum mechanics and can be understood in terms of scattering of waves in the semiclassical limit [116]. The Lyapunov exponent measures the scrambling caused on the observable A by a perturbation encoded by the operator B. A priori it depends on the choice of A and B, however it is generally assumed to be a property of the model independent of the choice of observables [116].

One of the remarkable properties of the SYK model is that its Lyapunov exponent saturates the bound (5.64) at low temperature. This is a consequence of the reparametrisation invariance [114]. It is then interesting to study the quantum Lyapunov exponent in the model defined from the Fokker-Planck operator and considered here, to test the extent of its similarity with SYK. However, the harmonic approximation cannot capture the Lyapunov regime. For a collection of harmonic oscillators, four-point functions like the OTOCs are directly related to two-point functions, that cannot encode properties of chaos [145]. See Appendix 5.B for more details and explicit derivations. Therefore, we conclude that the $p = 2$ model is not chaotic, while a more refined analysis than the one presented here is required for $p > 2$.

5.5 Discussion and conclusion

In this chapter we presented the first steps towards a connection between the low-temperature physics of the SYK model, a quantum model of disordered Fermions, and the classical out-of-equilibrium dynamics of the spherical p-spin model. The former has been the focus of intense scrutiny in recent years as a solvable toy model for holographic black holes and the AdS/CFT correspondence, while the latter is a solvable prototypical example of a classical system whose long-time dynamics shows ageing, and in which ergodicity is broken due to the underlying structure of a rugged free-energy landscape.

At the heart of the connection is the correspondence between stochastic dynamics and quantum thermodynamics as imaginary time, or equivalently between Fokker-Planck and Schrödinger operators. We used it to construct a quantum model, which we propose as a Bosonic analogue of SYK, and can be studied from both the non-equilibrium stochastic dynamics and equilibrium quantum thermodynamic perspectives.

The quantum model obtained is a variation of the spherical p-spin, in which the low-temperature equilibrium physics is mapped to the long-time classical dynamics of the standard p-spin. Its zero-temperature entropy corresponds to the configurational entropy at the threshold of the classical model. For $p = 2$ we showed that it vanishes (as expected); however the physics of the model is not trivial, showing a zero-temperature transition similar to Bose-Einstein condensation at strong coupling. We computed the scaling of the specific heat and features of the correlation function, including a $|t|^{-1/2}$ power law that is cutoff at a timescale $\propto \beta_q^2$, see Table 5.1.

The study of the model for $p > 2$ is much more involved. We showed that the zero-temperature entropy is finite and we presented an analysis based on a harmonic approximation, consisting in expanding the classical potential to second order around stationary points, both stable and unstable. The low-temperature physics is determined by the classical states just above the threshold. The quantum model is then approximated as a collection of harmonic oscillators with a density of states obtained by determining the scaling above the threshold.

The harmonic approximation becomes exact in the $T_s \to 0$ limit. Within the approximation the specific heat scales as $T_q^{2/3}$, the correlation function relaxes to a plateau with a $|t|^{-1/2}$ power law, with a cutoff at a timescale $\propto \beta_q^{4/3}$. These results confirm a similarity between SYK and the model obtained from the p-spin Fokker-Planck operator, with finite entropy and critical behaviour at $T_q \to 0$, although with different

exponents. This difference is not surprising, due to the different nature of the degrees of freedom (Fermionic and Bosonic) in the two models, and different density of states, with the $|t|^{-1/2}$ power law arising from the scaling at the edge of the semicircle. However, a more complete analysis, going beyond the harmonic approximation, is necessary to fully characterise the critical behaviour in the glass-inspired model at arbitrary T_s, and especially around the dynamical transition $T_s \approx T_d$. This will be the goal of future work.

The emerging reparametrisation invariance that is behind much of the interest in SYK has long been known in the theory of glasses, particularly the p-spin model. It is not trivially inherited by the quantum model, requiring a careful analysis of the mean-field equations with periodic time, which will be presented elsewhere. We expect that a deeper understanding of this invariance, enriched by the field-theoretical perspective of SYK and related models, will allow to revisit the promising and ambitious programme for a unified theory of glasses based on it [119]. We stress again that while this work is set in the framework of glassy physics being a manifestation of a complex free energy landscape, predictions based on the time reparametrisation invariance are more general and have been verified in finite-dimensional spin glass and particle models, as well as in kinetically constrained models. A better characterisation of the theory at the mean field level will hopefully be a firmer starting point for further analysis in finite dimension.

On the other hand, the mean-field theory of glasses could give new insight into the physics of toy models of black holes. For example, questions about spectral properties can be translated to questions about the structure of the classical landscape. The main difficulty in this direction is to determine if SYK and other models can be mapped back to a classical stochastic model.

Finally, going beyond the harmonic approximation is necessary to capture chaotic behaviour. It is interesting to investigate whether the bound on chaos is saturated, a crucial property of SYK, related to the reparametrisation invariance. This will also elucidate the relation between the four-point functions used to detect quantum chaos (OTOCs) and those describing fluctuations in glasses.

Appendix

5.A Scaling above the threshold

In this appendix we analyse eq. (5.47) in the double scaling limit with $\mathcal{E} - \mathcal{E}_c = At^{*-\alpha}$ as $t^* \to +\infty$, $A, \alpha > 0$ fixed. To ease the notation, we drop the $*$ and denote the time by t. Three terms contribute to the entropy: I_0 (first row), I_1 and I_2 (first and second integral respectively).

$T_s = 0$

- The leading contribution to the first term is the total number of saddles at energy density $\mathcal{E}$,

$$I_0 = \frac{1}{2}\left(1 + \ln\frac{p}{2}\right) - \mathcal{E}_c^2 + \ln|\mathcal{E}_c| - \left(\mathcal{E}^2 - \mathcal{E}_c^2\right) + \frac{1}{2}\,\mathrm{Re}\left[\left(\frac{\mathcal{E} \mp \sqrt{\mathcal{E}^2 - \mathcal{E}_c^2}}{\mathcal{E}_c}\right)^2\right] \tag{5.65}$$

$$= s_0 - \frac{1}{2} - 2A\mathcal{E}_c t^{-\alpha} - A^2 t^{-2\alpha} + \frac{1}{2}\left[\left(1 + \frac{A}{\mathcal{E}_c} t^{-\alpha}\right)^2 - \frac{-2A\mathcal{E}_c t^{-\alpha} - A^2 t^{-2\alpha}}{\mathcal{E}_c^2}\right] \tag{5.66}$$

$$= s_0 - 2A\left(\mathcal{E}_c - \mathcal{E}_c^{-1}\right) t^{-\alpha} + \mathcal{O}(t^{-2\alpha})\ . \tag{5.67}$$

- The integrand in I_1 is exponentially small in t, but not uniformly in ω: its leading contribution comes from $|\omega| t \lesssim 1$, which is in the integration domain if the energy is above the threshold. The edge of the semicircle is at $-pAt^{-\alpha}$. If $\alpha < 1$, the contributing region is far from the edge. Up to exponentially small

corrections

$$-I_1 = \int_{-c/t}^{c/t} \mathrm{d}\omega \rho_p(\omega + p\mathcal{E}) \ln\left(1 - e^{-t|\omega|}\right) = \int_{-c}^{c} \frac{\mathrm{d}y}{t} \rho_p(p\mathcal{E} + y/t) \ln\left(1 - \mathrm{e}^{-|y|}\right) \tag{5.68}$$

$$= 2t^{-1}\rho_p(p\mathcal{E}) \int_0^c \ln\left(1 - \mathrm{e}^{-y}\right) \mathrm{d}y + \mathcal{O}(t^{-2}) \tag{5.69}$$

$$= \frac{2p}{\pi(p-1)} \sqrt{-2A\mathcal{E}_c} \left[\mathrm{Li}_2(\mathrm{e}^{-c}) - \pi^2/2\right] t^{-1-\alpha/2} + \mathcal{O}(t^{-2-\alpha/2}) \tag{5.70}$$

$$\approx -\frac{\pi^2 p}{p-1} \sqrt{-2A\mathcal{E}_c} t^{-1-\alpha/2} \ . \tag{5.71}$$

To go from the first to the third line, we used that $\rho_p(p\mathcal{E}+y/t) \approx \sqrt{At^{-\alpha} + yt^{-1}} \approx \sqrt{A}t^{-\alpha/2}$ since $\alpha < 1$. If $\alpha > 1$, the t^{-1} term dominates, and overall $I_1 \propto t^{-1-\min(1,\alpha)/2}$.

- The second integral can be performed analytically

$$I_2 = t\frac{2}{\pi p^2 \mathcal{E}_c^2} \int_{-p(\mathcal{E}+\mathcal{E}_c)}^{0} \sqrt{p^2\mathcal{E}_c^2 - (p\mathcal{E}+\omega)^2}\omega \mathrm{d}\omega \tag{5.72}$$

$$= -\frac{pt}{6\pi\mathcal{E}_c^2} \left[2(\mathcal{E}^2 + 2\mathcal{E}_c^2)\sqrt{\mathcal{E}_c^2 - \mathcal{E}^2} + 6\mathcal{E}\mathcal{E}_c^2 \left(\frac{\pi}{2} + \arctan\frac{\mathcal{E}}{\sqrt{\mathcal{E}_c^2 - \mathcal{E}^2}}\right)\right] \tag{5.73}$$

$$= -\frac{8p}{15\pi\mathcal{E}_c^2} \sqrt{-2\mathcal{E}_c} A^{-\frac{5}{2}} t^{1-\frac{5}{2}\alpha} \tag{5.74}$$

Summing the three contributions, the entropy of stable states at t, $\mathcal{E} - \mathcal{E}_c = At^{-\alpha}$ is given by

$$s - s_0 = c_0 t^{-\alpha} - c_1 t^{-1-\min(\alpha,1)/2} - c_2 t^{1-\frac{5}{2}\alpha} \tag{5.75}$$

where the c's are positive coefficients depending on A and p.

As expected from the intuition given in the main text, the first term gives a positive contribution, while the other two a negative one. The first term is larger for smaller α. The second term is subleading for $\alpha < 1$. The entropy then is maximised by the smallest α for which the negative contributions are not larger than the positive one. The leading terms in I_0, I_2 must be of the same order:

$$-\alpha \stackrel{!}{=} 1 - \frac{5}{2}\alpha \Rightarrow \alpha = \frac{2}{3}. \tag{5.76}$$

For this to be a valid solution, the overall coefficient should be positive, $\max_A(c_0 -$

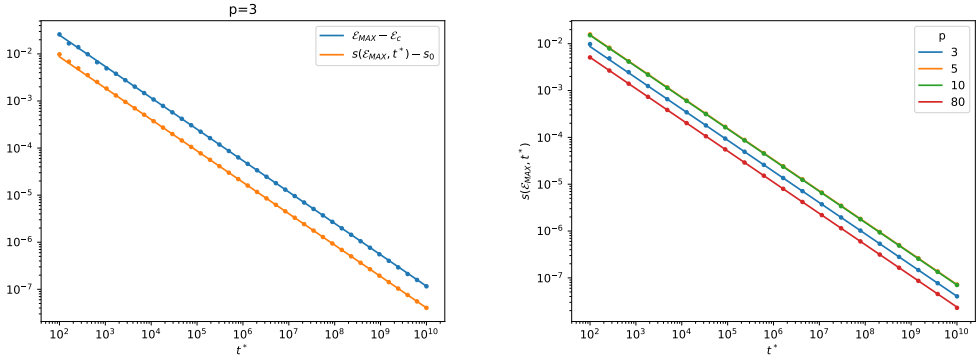

Figure 5.8: Scaling of $\mathcal{E}_M$ and s_M with t. The dots are obtained by maximising eq. (5.47) numerically. The solid lines are $\propto t^{-2/3}$ with coefficients from eq. (5.78,5.79).

$c_2 > 0$). This is indeed the case:

$$c_0 - c_2 = \sqrt{2}A\left[\frac{(p-2)}{\sqrt{p(p-1)}} - \frac{8p^{\frac{7}{4}}A^{\frac{3}{2}}}{15\pi(2(p-1))^{\frac{3}{4}}}\right] > 0 \Leftrightarrow 0 < A < \frac{[15\pi(p-2)]^{\frac{2}{3}}(p-1)^{\frac{1}{6}}}{2\sqrt{2p^3}} \tag{5.77}$$

$$A_M = \frac{[3\pi(p-2)]^{\frac{2}{3}}(p-1)^{\frac{1}{6}}}{2^{\frac{5}{6}}p^{\frac{3}{2}}} \tag{5.78}$$

Combining the above results, the leading correction to the entropy at long times is

$$s_M(t) = s_0 + c_M t^{-\frac{2}{3}} \qquad c_M = \frac{3(3\pi)^{\frac{2}{3}}(p-2)^{5/3}}{5\cdot 2^{\frac{1}{3}}(p-1)^{\frac{1}{3}}p^2}. \tag{5.79}$$

Both the exponent and the coefficients agree with the scaling obtained by maximising eq. (5.47) numerically, see Fig. 5.8.

Harmonic approximation

In the harmonic approximation, $\omega_\mu^2 = \hat{\lambda}T_s/2 + (\lambda-\mu)^2/4$, with $\lambda = -p\mathcal{E}$, $\hat{\lambda} \propto T_q^{2+\alpha}$. Here we analyse how the contributions in (5.55) differ from those of (5.47).

- The first term $I_0(\mathcal{E})$ is exactly the same, counting the number of stable states at energy $\mathcal{E}$.
- The first integral corresponds to I_1 (5.68). Here $\hat{\lambda}T_s$ acts as a cutoff, removing the divergence of the integrand. It vanishes fast enough that the integrand is

still exponentially small in T_q, but not uniformly in μ. However, it is enough to note that since $\omega > |\lambda - \mu|/2$, the $T_s > 0$ contribution is smaller than I_1, which was shown to be always subleading in the previous section.

$$\begin{aligned}\left|\int \mathrm{d}\rho(\mu) \ln\left(1 - \mathrm{e}^{-2t^*\omega_\mu}\right)\right| &= -\int \mathrm{d}\rho(\mu) \ln\left|1 - \mathrm{e}^{-2t^*\omega_\mu}\right| \\ &< -\int \mathrm{d}\rho(\mu) \ln\left|1 - \mathrm{e}^{-t^*|\lambda-\mu|}\right| = |I_1| \ .\end{aligned} \tag{5.80}$$

- For $\hat{\lambda} T_s \to 0$, the second integral reduces to I_2 (5.72). The correction can be bounded by considering separately two contributions. From $|\lambda - \mu| \lesssim T_q^{\beta/2}$, we get a contribution that can be bounded by $\approx T_q^{\beta+\alpha/2} = T_q^{2+3\alpha/2}$. Expanding the square root for $|\lambda - \mu| \gg T_q^{\beta/2}$,

$$\approx \frac{1}{T_q} \int_{|\lambda-\mu| \gg T_q^\beta} \mathrm{d}\rho(\mu) \frac{\hat{\ell} T_q^\beta}{|\lambda - \mu|} \propto T_q^{1+\frac{3}{2}\alpha} \log(T_q) \tag{5.81}$$

  we get a logarithmic correction, which is small compared to $I_2 \propto T_q^{\frac{5}{2}\alpha - 1}$.

- The additional term is $\frac{\hat{\lambda} T_s}{4 T_q} \propto T_q^{1+\alpha}$, and is always subleading.

Therefore, eq. (5.79) is correct within the harmonic approximation and $\alpha = 2/3$.

5.B Out-of-time-order correlators

For a single quantum harmonic oscillator of frequency ω, we can consider OTOCs for the position and momentum operator. They can be computed directly by using the commutation relations:

$$C_{xx}^{(\omega)}(t) = (m\omega)^{-4} C(\omega)_{pp}(t) = \left(\frac{\hbar}{m\omega}\right)^2 \sin(\omega t)^2 \tag{5.82}$$

$$C(\omega)_{xp}(t) = \hbar^2 \cos(\omega t)^2 \ . \tag{5.83}$$

They obey the relation

$$m^2 \omega^2 C(\omega)_{xx} + C(\omega)_{xp} = \hbar^2 \ . \tag{5.84}$$

Due to the linear dynamics, they are simply related to the squares of the corresponding two-point functions, and they are independent of temperature. For a system of non-interacting harmonic oscillators, the OTOCs are given by a linear superposition of

(5.82, 5.83), with some density $\rho(\omega)$ and therefore cannot have exponential growth, regardless of the shape of ρ. This is not surprising, since the system considered is integrable, however it is worth pointing out that the harmonic approximation cannot capture chaotic behaviour.

The $p = 2$, and $p > 2$, $T_s = 0$ OTOCs can be calculated exactly by integrating the single-oscillator correlators over the Wigner semicircle density ρ of radius R,

$$C_{xp}(t) = \hbar^2 \int \mathrm{d}\rho(\mu) \cos\left(\frac{\lambda - \mu}{2} t\right)^2 = \frac{\hbar^2}{2} + \frac{\hbar^2}{Rt} \cos(\lambda t) J_1(Rt) \tag{5.85}$$

$$C_{pp}(t) = \left(\frac{\hbar m}{2}\right)^2 \left[\frac{R^2 + 4\lambda^2}{8} + \frac{J_2(Rt)}{t^2} \left(3\cos(\lambda t) + 2t\lambda \sin(\lambda t)\right) + \right. \\ \left. - \frac{(R^2 + \lambda^2) J_1(Rt) \cos(t\lambda)}{Rt}\right] \tag{5.86}$$

This result is exact, and depends on the temperature through λ. They oscillate and decay to zero and to a constant respectively. Using (5.84),

$$\frac{\mathrm{d}^2}{\mathrm{d}t^2} C_{xx}(t) = \frac{4}{m^2} \left[C_{xp}(t) - \frac{\hbar^2}{2}\right] = \frac{4\hbar^2}{m^2} \frac{\cos(\lambda t) J_1(Rt)}{Rt} \,. \tag{5.87}$$

For $\lambda = R$ it can be integrated to

$$C_{xx}(t) = \left(\frac{2\hbar}{mR}\right)^2 \left[2Rt \left(J_0(Rt)\sin(Rt) - J_1(Rt)\cos(Rt)\right) + J_0(Rt)\cos(Rt) - 1\right] \tag{5.88}$$

which grows asymptotically as $\sqrt{Rt}$. For $\lambda > R$ ($p = 2$, $T_s > T_c$), the growth stops at $t \propto (\lambda - R)^{-1}$.

6 Summary and outlook

The interplay between quantum effects, disorder and interactions gives rise to many fascinating phenomena, which touch fundamental questions about our physical theories, and are also relevant for exciting technological developments such as high-temperature superconductors and quantum computers.

On the experimental side, it is now possible to create extremely clean and controlled systems, and manipulate them on the level of individual atoms. It is perhaps paradoxical that the success of the experimentalists' efforts to remove disorder has contributed to making its study more interesting, as the ability to introduce disorder in a controlled way is an invaluable tool for the understanding of its role.

On the theoretical side, the study of many-body localisation has grown from characterising conduction properties of metals [14, 18] to fundamental questions on ergodicity breaking and the applicability of statistical mechanics [6].

Despite much recent progress, understanding realistic interacting systems is still a formidable task. In this thesis we considered some mean-field models, drawn from random matrix theory and quantum spin glasses, which provide relatively tractable examples of strongly interacting, disordered systems. The goal is to investigate the phenomena in a more controlled settings, and develop tools that are hopefully more widely applicable. In particular, we focused on the issues of extended, non-ergodic phases, and the comparison between localisation and glassy physics. Here we summarise the main results obtained, highlighting some possible directions for future research.

Extended, non-ergodic phases

In Chapter 2 we considered the issue of extended, non-ergodic phases, and the difference between localisation and ergodicity transitions induced by disorder. In standard Anderson localisation the two transitions coincide: there is a localised, non-ergodic phase at strong disorder and a delocalised, ergodic phase at low disorder. Eigenstates have non-trivial (and non-universal) multifractality properties only at the critical point [17].

We studied the generalised Rosenzweig–Porter model, and confirmed the existence of the intermediate phase by clarifying in detail the structure of the eigenstates. Our results, based on a SDE construction of the model, were later proved rigorously [75]. Solving belief-propagation-like equations for the local resolvent (Green function), we found exact expressions for its statistics. Based on that we proposed a new characterisation of the extended non-ergodic phase, providing a new perspective to approach the elusive phase and contributing to the following developments [77, 78, 146–148].

The state of the art regarding the intermediate phase in hierarchical lattices was recently reviewed in [148], where it is shown to exist on infinite Cayley trees. The situation is different for random regular graphs, in which the intermediate phase is not present in the thermodynamic limit, but only as a finite size effect. The non-ergodic scaling and multifractality are observed up to a crossover size N_c, which diverges exponentially approaching the localisation transition. Therefore there is no separate ergodicity transition, but the behaviour of observables probing volumes up to (very large) N_c is well described by the intermediate phase of the Cayley tree. Such behaviour will dominate the results of simulations, and potentially of experiments which are performed with a relatively small number of cold atoms.

Given that the relation between RRG and MBL is of affinity rather than an exact mapping, questions about intermediate many-body phases are still largely open. However the results presented in [148] provide a compelling picture and a starting point for future investigations.

Quantum spin glasses

In Chapters 3 and 4 we turned our attention to mean-field quantum disordered spin models, the p-spin and random energy models, looking at both equilibrium and dynamical transitions.

At the classical level these have been thoroughly studied since the seventies, and their description in terms of replica symmetry breaking, rugged free-energy landscape and ergodicity breaking due to a proliferation of metastable states provides one of the main frameworks for the description of the physics of glasses and spin glasses [35, 118, 143]. To study the effects of quantum fluctuations within this description of glasses, quantum models, obtained by adding a transverse field, have been considered. Their solution within the static approximation lead to good generic understanding of their phase diagram, and approximate numerical techniques have been developed to provide quantitative results for specific models and describe their dissipative dynamics [87, 89, 90, 92, 93, 121]. More recently these models have been reconsidered in relation to

isolated dynamics and many-body localisation [39–41].

In Chapter 3 we presented a microcanonical calculation of the overlap-resolved entropy in the classical p-spin model using the replica method. Our results, analogous to the standard canonical analysis of the Franz–Parisi potential, provide insight on the structure of the configuration space, and a complementary picture of the dynamical transition. We computed correctly, at the 1RSB level, the energy below which the configuration space divides into high-overlap clusters, and clarified (at the classical level) the difference between clustering and dynamical glass transitions.

In Chapter 4 we developed a numerically exact method to compute the imaginary-time correlation functions of the quantum p-spin model, and used it to solve the replica symmetric equations describing the two high-temperature phases. The method, based on diagrammatic Monte Carlo, allows to accurately determine the region of existence of each phase, and the critical line separating them. We also developed a class of self-consistent approximations, which provide a very efficient way to compute physical properties of the high-field phase (QPM), but fail to describe the classical phases. To capture the spin-glass phase and the dynamical transition, the diagMC method can be extended to the 1RSB level. Computationally, we expect this to be significantly more demanding, but feasible.

Turning to the dynamical phase diagram, we presented an argument to determine ergodicity and localisation in the QREM, informed by the GRP results of Chapter 2. This indicates that there are two separate transitions. The equilibrium classical paramagnetic phase corresponds to three distinct dynamical phases: a localised one at low field, an ergodic one at high field (but before the equilibrium transition), and an intermediate phase separating the two. The structure of the eigenstates in the intermediate phase has not been investigated, and the results of Chapter 2 could provide a starting point for a detailed characterisation.

For the quantum p-spin model, we revisited the clustering picture proposed in [41], in light of the microcanonical calculation of Chapter 3 and the refined phase diagram. We found that in the large p limit, or perturbatively in Γ, the clustering picture holds, and provided an improved calculation of the clustering temperature. However at finite p the approximations used are not consistent, leaving the question of the dynamical phase diagram at finite p and Γ open.

The most promising direction to tackle this is to extend the diagMC method from imaginary-time to real-time dynamics, by formulating it on the Keldysh contour. The formalism for this was recently introduced for a related model [108], showing the importance of the equilibrium analysis to determine the initial conditions for the dynamics.

Detailed simulations based on this are within reach, and will provide a powerful tool to investigate the dynamical phase diagram.

Reparametrisation invariance

In Chapter 5 we explored a connection between the classical dynamics of mean-field spin-glass models and the SYK model. The latter is a variation of a mean-field model of a disordered magnet. Its Hamiltonian is similar to that of the p-spin model, but its degrees of freedom are Majorana Fermions. We derived the TAP equations for SYK, confirming that its TAP free energy is trivial, and the annealed calculation is correct at arbitrary temperature, a fact usually assumed in the literature.

Due to some peculiar low-temperature properties, SYK has recently attracted much interest in the string theory literature as a solvable example of the AdS/CFT correspondence, a toy model for holographic black holes [113, 114, 117]. Crucial for these properties is the approximate invariance under time reparametrisation of the equation for the Green function, which becomes exact at $T \to 0$.

A similar invariance appears in the classical dynamics of spin glasses in the long time limit. An effective theory for this soft mode has been proposed as a unified description of glassy dynamics [119], but is difficult to construct explicitly. Such a theory is known for SYK.

To build a bridge between the two, we constructed a quantum model from the Fokker-Planck operator describing the classical stochastic dynamics of the spherical p-spin model. The model can be analysed either from the quantum (Matsubara path integral) or the classical stochastic (MSRJD) perspective, creating a correspondence between quantum equilibrium properties and features of the classical free energy landscape.

We analysed the model for $p = 2$, and for $p > 2$ in the harmonic approximation. Our results show that the model shares some of the low-temperature properties of SYK, which we understand in terms of classical glassy physics. Further analysis of the model proposed here, going beyond the harmonic approximation, is an exciting direction of research.

Bibliography

[1] D. Facoetti, P. Vivo, and G. Biroli, "From non-ergodic eigenvectors to local resolvent statistics and back: a random matrix perspective", EPL (Europhysics Letters) **115**, 47003 (2016), arXiv:1607.05942 [cond-mat.dis-nn].

[2] D. Facoetti, G. Biroli, J. Kurchan, and D. R. Reichman, *Classical glasses, black holes, and strange quantum liquids*, arXiv:1906.09228 [hep-th].

[3] J. von Neumann, "Wahrscheinlichkeitstheoretischer aufbau der quantenmechanik", Göttinger Nachrichten, 245–272 (1927).

[4] J. Eisert, M. Friesdorf, and C. Gogolin, "Quantum many-body systems out of equilibrium", Nature Physics **11**, 124–130 (2015), arXiv:1408.5148 [quant-ph].

[5] I. Bloch, J. Dalibard, and W. Zwerger, "Many-body physics with ultracold gases", Rev. Mod. Phys. **80**, 885–964 (2008), arXiv:0704.3011 [cond-mat].

[6] R. Nandkishore and D. A. Huse, "Many-body localization and thermalization in quantum statistical mechanics", Annual Review of Condensed Matter Physics **6**, 15–38 (2015), arXiv:1404.0686 [cond-mat.stat-mech].

[7] M. Srednicki, "Chaos and quantum thermalization", Phys. Rev. E **50**, 888–901 (1994), arXiv:cond-mat/9403051.

[8] M. Rigol, V. Dunjko, and M. Olshanii, "Thermalization and its mechanism for generic isolated quantum systems", Nature **452**, 854–858 (2008), arXiv:0708.1324 [cond-mat.stat-mech].

[9] G. De Palma, A. Serafini, V. Giovannetti, and M. Cramer, "Necessity of eigenstate thermalization", Phys. Rev. Lett. **115**, 220401 (2015), arXiv:1506.07265 [quant-ph].

[10] S. Goldstein, J. L. Lebowitz, R. Tumulka, and N. Zanghì, "Canonical typicality", Phys. Rev. Lett. **96**, 050403 (2006), arXiv:cond-mat/0511091.

[11] T. Kinoshita, T. Wenger, and D. S. Weiss, "A quantum Newton's cradle", Nature **440**, 900–903 (2006), arXiv:cond-mat/9802263.

[12] G. Grosso and G. Parravicini, *Solid state physics* (Elsevier Science, 2000).

[13] P. W. Anderson, "Absence of diffusion in certain random lattices", Phys. Rev. **109**, 1492–1505 (1958).

[14] D. Basko, I. Aleiner, and B. Altshuler, "Metal–insulator transition in a weakly interacting many-electron system with localized single-particle states", Annals of Physics **321**, 1126 –1205 (2006), arXiv:cond-mat/0506617.

[15] A. Pal and D. A. Huse, "Many-body localization phase transition", Phys. Rev. B **82**, 174411 (2010), arXiv:1010.1992 [cond-mat.dis-nn].

[16] J. Z. Imbrie, V. Ros, and A. Scardicchio, "Local integrals of motion in many-body localized systems", Annalen der Physik **529**, 1600278 (2017), arXiv:1609.08076 [cond-mat.dis-nn].

[17] F. Evers and A. D. Mirlin, "Anderson transitions", Rev. Mod. Phys. **80**, 1355–1417 (2008), arXiv:0707.4378 [cond-mat.mes-hall].

[18] B. L. Altshuler, Y. Gefen, A. Kamenev, and L. S. Levitov, "Quasiparticle lifetime in a finite system: a nonperturbative approach", Phys. Rev. Lett. **78**, 2803–2806 (1997).

[19] F. Pietracaprina, V. Ros, and A. Scardicchio, "Forward approximation as a mean-field approximation for the Anderson and many-body localization transitions", Phys. Rev. B **93**, 054201 (2016), arXiv:1508.05097 [cond-mat.dis-nn].

[20] G. Biroli, A. C. Ribeiro-Teixeira, and M. Tarzia, "Difference between level statistics, ergodicity and localization transitions on the Bethe lattice", arXiv:1211.7334 [cond-mat.dis-nn].

[21] A. De Luca, A. Scardicchio, V. E. Kravtsov, and B. L. Altshuler, "Support set of random wave-functions on the Bethe lattice", arXiv:1401.0019 [cond-mat.stat-mech].

[22] A. De Luca, B. L. Altshuler, V. E. Kravtsov, and A. Scardicchio, "Anderson localization on the Bethe lattice: nonergodicity of extended states", Phys. Rev. Lett. **113**, 046806 (2014), arXiv:1403.7817 [cond-mat.stat-mech].

[23] M. Pino, L. B. Ioffe, and B. L. Altshuler, "Nonergodic metallic and insulating phases of Josephson junction chains", Proc. Natl. Acad. Sci. U.S.A. **113**, 536–541 (2016), arXiv:1501.03853 [cond-mat].

[24] J. Goold, C. Gogolin, S. R. Clark, J. Eisert, A. Scardicchio, and A. Silva, "Total correlations of the diagonal ensemble herald the many-body localization transition", Phys. Rev. B **92**, 180202 (2015), arXiv:1504.06872 [cond-mat].

[25] B. L. Altshuler, E. Cuevas, L. B. Ioffe, and V. E. Kravtsov, "Nonergodic phases in strongly disordered random regular graphs", Phys. Rev. Lett. **117**, 156601 (2016), arXiv:1605.02295 [cond-mat.dis-nn].

[26] K. S. Tikhonov, A. D. Mirlin, and M. A. Skvortsov, "Anderson localization and ergodicity on random regular graphs", Phys. Rev. B **94**, 220203 (2016), arXiv:1604.05353 [cond-mat.dis-nn].

[27] K. S. Tikhonov and A. D. Mirlin, "Fractality of wave functions on a Cayley tree: difference between tree and locally treelike graph without boundary", Phys. Rev. B **94**, 184203 (2016), arXiv:1608.00331 [cond-mat.dis-nn].

[28] S. F. Edwards and P. W. Anderson, "Theory of spin glasses", Journal of Physics F: Metal Physics **5**, 965–974 (1975).

[29] S. F. Edwards and P. W. Anderson, "Theory of spin glasses. II", Journal of Physics F: Metal Physics **6**, 1927–1937 (1976).

[30] D. Sherrington and S. Kirkpatrick, "Solvable model of a spin-glass", Phys. Rev. Lett. **35**, 1792–1796 (1975).

[31] G. Parisi, "Infinite number of order parameters for spin-glasses", Phys. Rev. Lett. **43**, 1754–1756 (1979).

[32] M. Mezard, G. Parisi, and M. Virasoro, *Spin glass theory and beyond*, Lecture Notes in Physics Series (World Scientific, 1987).

[33] C. De Dominicis and I. Giardina, *Random fields and spin glasses: a field theory approach* (Cambridge University Press, 2006).

[34] T. Castellani and A. Cavagna, "Spin-glass theory for pedestrians", Journal of Statistical Mechanics: Theory and Experiment **2005**, P05012 (2005), arXiv:cond-mat/0505032.

[35] F. Zamponi, *Mean field theory of spin glasses*, arXiv:1008.4844 [cond-mat.stat-mech].

[36] B. Derrida, "Random-energy model: limit of a family of disordered models", Phys. Rev. Lett. **45**, 79–82 (1980).

[37] B. Derrida, "Random-energy model: an exactly solvable model of disordered systems", Phys. Rev. B **24**, 2613–2626 (1981).

[38] D. Gross and M. Mezard, "The simplest spin glass", Nuclear Physics B **240**, 431 –452 (1984).

[39] C. R. Laumann, A. Pal, and A. Scardicchio, "Many-body mobility edge in a mean-field quantum spin glass", Phys. Rev. Lett. **113**, 200405 (2014), arXiv:1404.2276 [cond-mat.stat-mech].

[40] C. L. Baldwin, C. R. Laumann, A. Pal, and A. Scardicchio, "The many-body localized phase of the quantum random energy model", Phys. Rev. B **93**, 024202 (2016), arXiv:1509.08926 [cond-mat].

[41] C. L. Baldwin, C. R. Laumann, A. Pal, and A. Scardicchio, "Clustering of nonergodic eigenstates in quantum spin glasses", Phys. Rev. Lett. **118**, 127201 (2017), arXiv:1611.02296 [cond-mat].

[42] G. Mossi and A. Scardicchio, "Ergodic and localized regions in quantum spin glasses on the Bethe lattice", Philosophical Transactions of the Royal Society A **375** (2017) 10.1098/rsta.2016.0424, arXiv:1703.03678 [cond-mat.dis-nn].

[43] X. Chen, X. Yu, G. Y. Cho, B. K. Clark, and E. Fradkin, "Many-body localization transition in Rokhsar-Kivelson-type wave functions", Phys. Rev. B **92**, 214204 (2015), arXiv:1509.03890 [cond-mat.dis-nn].

[44] G. Biroli and J.-P. Bouchaud, "The random first-order transition theory of glasses: a critical assessment", in *Structural glasses and supercooled liquids: theory, experiment, and applications* (2012), arXiv:0912.2542 [cond-mat.dis-nn].

[45] G. Biroli and J. P. Garrahan, "Perspective: the glass transition", The Journal of Chemical Physics **138**, 12A301 (2013), arXiv:1303.3542 [cond-mat.stat-mech].

[46] J. P. Garrahan, "Aspects of non-equilibrium in classical and quantum systems", Physica A: Statistical Mechanics and its Applications **504**, 130 –154 (2018), arXiv:1709.09208 [cond-mat.stat-mech].

[47] Y. Bar Lev, G. Cohen, and D. R. Reichman, "Absence of diffusion in an interacting system of spinless fermions on a one-dimensional disordered lattice", Phys. Rev. Lett. **114**, 100601 (2015), arXiv:1407.7535 [cond-mat.dis-nn].

[48] Y. Bar Lev and D. R. Reichman, "Slow dynamics in a two-dimensional Anderson-Hubbard model", EPL **113**, 46001 (2016), arXiv:1508.05391 [cond-mat.dis-nn].

[49] R. Vosk, D. A. Huse, and E. Altman, "Theory of the many-body localization transition in one-dimensional systems", Phys. Rev. X **5**, 031032 (2015), arXiv:1412.3117 [cond-mat.dis-nn].

[50] A. C. Potter, R. Vasseur, and S. A. Parameswaran, "Universal properties of many-body delocalization transitions", Phys. Rev. X **5**, 031033 (2015), arXiv:1501.03501 [cond-mat.dis-nn].

[51] J.-Y. Choi, S. Hild, J. Zeiher, P. Schauß, A. Rubio-Abadal, T. Yefsah, V. Khemani, D. A. Huse, I. Bloch, and C. Gross, "Exploring the many-body localization transition in two dimensions", Science **352**, 1547–1552 (2016), arXiv:1604.04178 [cond-mat.quant-gas].

[52] V. E. Kravtsov, I. M. Khaymovich, E Cuevas, and M Amini, "A random matrix model with localization and ergodic transitions", New Journal of Physics **17**, 122002 (2015), arXiv:1508.01714 [cond-mat.dis-nn].

[53] I. Oren and U. Smilansky, "Trace formulas and spectral statistics for discrete Laplacians on regular graphs (II)", Journal of Physics A **43**, 225205 (2010), arXiv:1003.1445 [math-ph].

[54] M. L. Manning and A. J. Liu, "A random matrix definition of the boson peak", EPL **109**, 36002 (2015), arXiv:1307.5904 [cond-mat.soft].

[55] X. Cao, A. Rosso, J.-P. Bouchaud, and P. Le Doussal, "Genuine localization transition in a long-range hopping model", Phys. Rev. E **95**, 062118 (2017), arXiv:1607.04173 [cond-mat.stat-mech].

[56] P. Bourgade, private communication.

[57] N. Rosenzweig and C. E. Porter, "Repulsion of energy levels in complex atomic spectra", Phys. Rev. **120**, 1698–1714 (1960).

[58] E. Brézin and S. Hikami, "Correlations of nearby levels induced by a random potential", Nucl. Phys. B **479**, 697 –706 (1996).

[59] H. Kunz and B. Shapiro, "Transition from Poisson to Gaussian unitary statistics: the two-point correlation function", Phys. Rev. E **58**, 400–406 (1998), arXiv:cond-mat/9802263.

[60] A. Pandey, "Brownian-motion model of discrete spectra", Chaos, Solitons & Fractals **5**, 1275 –1285 (1995).

[61] A. Altland, M. Janssen, and B. Shapiro, "Perturbation theory for the Rosenzweig-Porter matrix model", Phys. Rev. E **56**, 1471–1475 (1997), arXiv:cond-mat/9705227.

[62] T. Guhr, "Transitions toward quantum chaos: with supersymmetry from Poisson to Gauss", Annals of Physics **250**, 145 –192 (1996), arXiv:cond-mat/9510052.

[63] P. Shukla, "Localization to ergodic transitions: is Rosenzweig–Porter ensemble the hidden skeleton?", New Journal of Physics **18**, 021004 (2016).

[64] E. Tarquini, G. Biroli, and M. Tarzia, "Level statistics and localization transitions of Lévy matrices", Phys. Rev. Lett. **116**, 010601 (2016), arXiv:1507.00296 [cond-mat.stat-mech].

[65] D. S. Bernstein, *Matrix mathematics* (Princeton University Press, 2009).

[66] M. Mézard and G. Parisi, "The Bethe lattice spin glass revisited", Eur. Phys. J. B **20**, 217–233 (2001), arXiv:cond-mat/0009418.

[67] R. G. Margiotta, R. Kühn, and P. Sollich, "Spectral properties of the trap model on sparse networks", Journal of Physics A: Mathematical and Theoretical **51**, 294001 (2018), arXiv:1802.10144 [cond-mat.dis-nn].

[68] A. D. Mirlin and Y. V. Fyodorov, "Distribution of local densities of states, order parameter function, and critical behavior near the Anderson transition", Phys. Rev. Lett. **72**, 526–529 (1994).

[69] F. J. Dyson, "A Brownian-motion model for the eigenvalues of a random matrix", Journal of Mathematical Physics **3**, 1191–1198 (1962).

[70] P. Bourgade and H.-T. Yau, "The eigenvector moment flow and local quantum unique ergodicity", Communications in Mathematical Physics **350**, 231–278 (2017), arXiv:1312.1301 [math.PR].

[71] R. Allez, J. Bun, and J.-P. Bouchaud, "The eigenvectors of Gaussian matrices with an external source", arXiv:1412.7108 [math.PR].

[72] D. S. Dean, "Langevin equation for the density of a system of interacting langevin processes", Journal of Physics A: Mathematical and General **29**, L613 (1996), arXiv:cond-mat/9611104.

[73] L. C. G. Rogers and Z. Shi, "Interacting Brownian particles and the Wigner law", Probability Theory and Related Fields **95**, 555–570 (1993).

[74] J.-P. Blaizot and M. A. Nowak, "Universal shocks in random matrix theory", Phys. Rev. E **82**, 051115 (2010), arXiv:0902.2223 [hep-th].

[75] P. von Soosten and S. Warzel, "Non-ergodic delocalization in the Rosenzweig-Porter model", Letters in Mathematical Physics (2018) 10.1007/s11005-018-1131-7, arXiv:1709.10313 [math-ph].

[76] P. von Soosten and S. Warzel, "The phase transition in the ultrametric ensemble and local stability of dyson brownian motion", Electron. J. Probab. **23**, 24 pp. (2018), arXiv:1705.00923 [math.PR].

[77] M. Amini, "Spread of wave packets in disordered hierarchical lattices", EPL (Europhysics Letters) **117**, 30003 (2017), arXiv:1703.04671 [cond-mat.dis-nn].

[78] G. De Tomasi, M. Amini, S. Bera, I. M. Khaymovich, and V. E. Kravtsov, "Survival probability in Generalized Rosenzweig-Porter random matrix ensemble", SciPost Phys. **6**, 14 (2019), arXiv:1805.06472 [cond-mat.dis-nn].

[79] J. J. Sakurai and J. Napolitano, *Modern quantum mechanics* (Addison-Wesley, 2011).

[80] G. Livan, M. Novaes, and P. Vivo, *Introduction to random matrices: theory and practice* (Springer, 2018), arXiv:1712.07903 [math-ph].

[81] P. Vivo, "Large deviations of the maximum of independent and identically distributed random variables", European Journal of Physics **36**, 055037 (2015), arXiv:1507.05442 [cond-mat.stat-mech].

[82] M. Talagrand, *Spin glasses: a challenge for mathematicians* (Springer, 2003).

[83] S. Franz and G. Parisi, "Recipes for metastable states in spin glasses", J. Phys. I France **5**, 1401 (1995), arXiv:cond-mat/9503167.

[84] U. Ferrari, L. Leuzzi, G. Parisi, and T. Rizzo, "Two-step relaxation next to dynamic arrest in mean-field glasses: spherical and ising p-spin model", Phys. Rev. B **86**, 014204 (2012), arXiv:1202.4168 [cond-mat.dis-nn].

[85] E. Jones, T. Oliphant, P. Peterson, et al., *SciPy: open source scientific tools for Python*, (2001–) http://www.scipy.org/.

[86] W. Wu, B. Ellman, T. F. Rosenbaum, G. Aeppli, and D. H. Reich, "From classical to quantum glass", Phys. Rev. Lett. **67**, 2076–2079 (1991).

[87] A. J. Bray and M. A. Moore, "Replica theory of quantum spin glasses", Journal of Physics C: Solid State Physics **13**, L655 (1980).

[88] P. Shukla and S. Singh, "Classical and quantum spherical models of spin-glasses: a complete treatment of statistics and dynamics", Phys. Rev. B **23**, 4661–4666 (1981).

[89] Y. Y. Goldschmidt, "Solvable model of the quantum spin glass in a transverse field", Phys. Rev. B **41**, 4858–4861 (1990).

[90] V. Dobrosavljević and D. Thirumalai, "1/p expansion for a p-spin interaction spin-glass model in a transverse field", Journal of Physics A: Mathematical and General **23**, L767 (1990).

[91] T. M. Nieuwenhuizen and F. Ritort, "Quantum phase transition in spin glasses with multi-spin interactions", Physica A: Statistical Mechanics and its Applications **250**, 8 –45 (1998), arXiv:cond-mat/9706244.

[92] L. F. Cugliandolo, D. R. Grempel, G. Lozano, H. Lozza, and C. A. da Silva Santos, "Dissipative effects on quantum glassy systems", Phys. Rev. B **66**, 014444 (2002).

[93] L. F. Cugliandolo, D. R. Grempel, G. Lozano, and H. Lozza, "Effects of dissipation on disordered quantum spin models", Phys. Rev. B **70**, 024422 (2004), arXiv:cond-mat/0312064.

[94] F. Krzakala, A. Rosso, G. Semerjian, and F. Zamponi, "Path-integral representation for quantum spin models: application to the quantum cavity method and Monte Carlo simulations", Phys. Rev. B **78**, 134428 (2008), arXiv:0807.2553 [cond-mat.stat-mech].

[95] T. Jörg, F. Krzakala, J. Kurchan, and A. C. Maggs, "Simple glass models and their quantum annealing", Phys. Rev. Lett. **101**, 147204 (2008), arXiv:0806.4144 [quant-ph].

[96] T. Jörg, F. Krzakala, J. Kurchan, A. C. Maggs, and J. Pujos, "Energy gaps in quantum first-order mean-field–like transitions: the problems that quantum annealing cannot solve", EPL (Europhysics Letters) **89**, 40004 (2010), arXiv:0912.4865 [quant-ph].

[97] M. Suzuki, "Generalized Trotter's formula and systematic approximants of exponential operators and inner derivations with applications to many-body problems", Communications in Mathematical Physics **51**, 183–190 (1976).

[98] M. Schiró, "Real-time dynamics in quantum impurity models with diagrammatic Monte Carlo", Phys. Rev. B **81**, 085126 (2010), arXiv:0911.0184 [cond-mat.str-el].

[99] G. Kotliar, S. Y. Savrasov, K. Haule, V. S. Oudovenko, O. Parcollet, and C. A. Marianetti, "Electronic structure calculations with dynamical mean-field theory", Rev. Mod. Phys. **78**, 865–951 (2006), arXiv:cond-mat/0511085.

[100] M. Schiró and M. Fabrizio, "Real-time diagrammatic Monte Carlo for nonequilibrium quantum transport", Phys. Rev. B **79**, 153302 (2009), arXiv:0808.0589 [cond-mat.str-el].

[101] W. K. Hastings, "Monte Carlo sampling methods using Markov chains and their applications", Biometrika **57**, 97–109 (1970).

[102] A. Rüegg, E. Gull, G. A. Fiete, and A. J. Millis, "Sum rule violation in self-consistent hybridization expansions", Phys. Rev. B **87**, 075124 (2013), arXiv:1212.2694 [cond-mat.str-el].

[103] J. Berges, "Nonequilibrium quantum fields: from cold atoms to cosmology", in *Strongly interacting quantum systems out of equilibrium, Lecture notes of the Les Houches summer school, August 2012*, Vol. 99, edited by T. Giamarchi, A. J. Millis, O. Parcollet, H. Saleur, and L. F. Cugliandolo (2016), arXiv:1503.02907 [hep-ph].

[104] M. Eckstein and P. Werner, "Nonequilibrium dynamical mean-field calculations based on the noncrossing approximation and its generalizations", Phys. Rev. B **82**, 115115 (2010), arXiv:1005.1872 [cond-mat.str-el].

[105] M. L. Mehta, *Random matrices*, 3rd edition (Academic Press, 2004).

[106] Y. V. Fyodorov, A. Ossipov, and A. Rodriguez, "The anderson localization transition and eigenfunction multifractality in an ensemble of ultrametric random matrices", Journal of Statistical Mechanics: Theory and Experiment **2009**, L12001 (2009), arXiv:0909.4704 [cond-mat.mes-hall].

[107] A. Kamenev, *Field theory of non-equilibrium systems* (Cambridge University Press, 2011).

[108] L. F. Cugliandolo, G. S. Lozano, and N. Nessi, "Role of initial conditions in the dynamics of quantum glassy systems", Journal of Statistical Mechanics: Theory and Experiment **2019**, 023301 (2019), arXiv:1811.03987 [cond-mat.dis-nn].

[109] S. Sachdev and J. Ye, "Gapless spin-fluid ground state in a random quantum Heisenberg magnet", Phys. Rev. Lett. **70**, 3339–3342 (1993), arXiv:cond-mat/9212030.

[110] O. Parcollet and A. Georges, "Non-Fermi-liquid regime of a doped Mott insulator", Phys. Rev. B **59**, 5341–5360 (1999), arXiv:cond-mat/9806119.

[111] A. Georges, O. Parcollet, and S. Sachdev, "Mean field theory of a quantum Heisenberg spin glass", Phys. Rev. Lett. **85**, 840–843 (2000), arXiv:cond-mat/9909239.

[112] A. Georges, O. Parcollet, and S. Sachdev, "Quantum fluctuations of a nearly critical Heisenberg spin glass", Phys. Rev. B **63**, 134406 (2001), arXiv:cond-mat/0009388.

[113] A. Kitaev, *A simple model of quantum holography*, http://online.kitp.ucsb.edu/online/entangled15/kitaev/, http://online.kitp.ucsb.edu/online/entangled15/kitaev2/.

[114] J. Maldacena and D. Stanford, "Remarks on the Sachdev-Ye-Kitaev model", Phys. Rev. D **94**, 106002 (2016), arXiv:1604.07818 [hep-th].

[115] J. Maldacena, S. H. Shenker, and D. Stanford, "A bound on chaos", Journal of High Energy Physics **2016**, 106 (2016), arXiv:1503.01409 [hep-th].

[116] J. Kurchan, "Quantum bound to chaos and the semiclassical limit", Journal of Statistical Physics **171**, 965–979 (2018), arXiv:1612.01278 [cond-mat.stat-mech].

[117] V. Rosenhaus, "An introduction to the SYK model", arXiv:1807.03334 [hep-th].

[118] L. F. Cugliandolo and J. Kurchan, "Analytical solution of the off-equilibrium dynamics of a long-range spin-glass model", Phys. Rev. Lett. **71**, 173–176 (1993), arXiv:cond-mat/9303036.

[119] C. Chamon and L. F. Cugliandolo, "Fluctuations in glassy systems", Journal of Statistical Mechanics: Theory and Experiment **2007**, P07022 (2007), arXiv:0704.0684 [cond-mat.dis-nn].

[120] D. J. Thouless, P. W. Anderson, and R. G. Palmer, "Solution of 'solvable model of a spin glass'", The Philosophical Magazine: A Journal of Theoretical Experimental and Applied Physics **35**, 593–601 (1977).

[121] G. Biroli and L. F. Cugliandolo, "Quantum Thouless-Anderson-Palmer equations for glassy systems", Phys. Rev. B **64**, 014206 (2001), arXiv:cond-mat/0011028.

[122] T. Plefka, "Convergence condition of the TAP equation for the infinite-ranged ising spin glass model", Journal of Physics A: Mathematical and General **15**, 1971 (1982).

[123] G. Biroli, "Dynamical TAP approach to mean field glassy systems", Journal of Physics A: Mathematical and General **32**, 8365 (1999), arXiv:cond-mat/9909415.

[124] B. Bravi, P. Sollich, and M. Opper, "Extended Plefka expansion for stochastic dynamics", Journal of Physics A: Mathematical and Theoretical **49**, 194003 (2016), arXiv:1602.06964 [cond-mat.dis-nn].

[125] A. Crisanti and H.-J. Sommers, "The spherical p-spin interaction spin glass model: the statics", Zeitschrift für Physik B Condensed Matter **87**, 341–354 (1992).

[126] A. Crisanti and H.-J. Sommers, "Thouless-Anderson-Palmer approach to the spherical p-spin spin glass model", Journal de Physique I **5**, 805–813 (1995), arXiv:cond-mat/9406051.

[127] J. Zinn-Justin, *Quantum field theory and critical phenomena*, International series of monographs on physics (Clarendon Press, 2002).

[128] J. Kurchan, "Six out of equilibrium lectures", in *Long-range interacting systems, Lecture notes of the Les Houches summer school, August 2008*, Vol. 90, edited by T. Dauxois, S. Ruffo, and L. F. Cugliandolo (2010), arXiv:0901.1271 [cond-mat.stat-mech].

[129] D. S. Rokhsar and S. A. Kivelson, "Superconductivity and the quantum hard-core dimer gas", Phys. Rev. Lett. **61**, 2376–2379 (1988).

[130] G. Parisi, *Statistical field theory*, Frontiers in Physics (Addison-Wesley, 1988).

[131] G. Biroli, C. Chamon, and F. Zamponi, "Theory of the superglass phase", Phys. Rev. B **78**, 224306 (2008), arXiv:0807.2458 [cond-mat.dis-nn].

[132] Z. Nussinov, P. Johnson, M. J. Graf, and A. V. Balatsky, "Mapping between finite temperature classical and zero temperature quantum systems: quantum critical jamming and quantum dynamical heterogeneities", Phys. Rev. B **87**, 184202 (2013), arXiv:1209.3823 [cond-mat.stat-mech].

[133] Z. Lan, M. van Horssen, S. Powell, and J. P. Garrahan, "Quantum slow relaxation and metastability due to dynamical constraints", Phys. Rev. Lett. **121**, 040603 (2018), arXiv:1706.02603 [quant-ph].

[134] P. C. Martin, E. D. Siggia, and H. A. Rose, "Statistical dynamics of classical systems", Phys. Rev. A **8**, 423–437 (1973).

[135] H.-K. Janssen, "On a Lagrangean for classical field dynamics and renormalization group calculations of dynamical critical properties", Zeitschrift für Physik B Condensed Matter **23**, 377–380 (1976).

[136] C. De Dominicis, "Techniques de renormalisation de la théorie des champs et dynamique des phénomènes critiques", Journal de Physique Colloques **37**, C1–247–C1–253 (1976).

[137] U. Täuber, *Critical dynamics: a field theory approach to equilibrium and non-equilibrium scaling behavior* (Cambridge University Press, 2014).

[138] G. Biroli and J. Kurchan, "Metastable states in glassy systems", Phys. Rev. E **64**, 016101 (2001), arXiv:cond-mat/0005499.

[139] B. Gaveau and L. S. Schulman, "Theory of nonequilibrium first-order phase transitions for stochastic dynamics", Journal of Mathematical Physics **39**, 1517–1533 (1998).

[140] J. M. Kosterlitz, D. J. Thouless, and R. C. Jones, "Spherical model of a spin-glass", Phys. Rev. Lett. **36**, 1217–1220 (1976).

[141] L. F. Cugliandolo and D. S. Dean, "Full dynamical solution for a spherical spin-glass model", J. Phys. A **28**, 4213–4234 (1995), arXiv:cond-mat/9502075.

[142] M. Rokni and P. Chandra, "Dynamical study of the disordered quantum $p = 2$ spherical model", Phys. Rev. B **69**, 094403 (2004), arXiv:cond-mat/0301166.

[143] A. Cavagna, I. Giardina, and G. Parisi, "Stationary points of the Thouless-Anderson-Palmer free energy", Phys. Rev. B **57**, 11251–11257 (1998), arXiv:cond-mat/9710272.

[144] G. D. Mahan, *Many-particle physics*, Third edition (Kluwer Academic/Plenum Publishers, 2000).

[145] L. Foini and J. Kurchan, "The eigenstate thermalization hypothesis and out of time order correlators", arXiv:1803.10658 [cond-mat.stat-mech].

[146] I. García-Mata, O. Giraud, B. Georgeot, J. Martin, R. Dubertrand, and G. Lemarié, "Scaling theory of the Anderson transition in random graphs: ergodicity and universality", Phys. Rev. Lett. **118**, 166801 (2017), arXiv:1609.05857 [cond-mat.stat-mech].

[147] V. Kravtsov, B. Altshuler, and L. Ioffe, "Non-ergodic delocalized phase in Anderson model on Bethe lattice and regular graph", Annals of Physics **389**, 148–191 (2018), arXiv:1712.00614 [cond-mat.dis-nn].

[148] G. Biroli and M. Tarzia, "Delocalization and ergodicity of the Anderson model on Bethe lattices", arXiv:1810.07545 [cond-mat.dis-nn].